



**HAL**  
open science

## Two opposite voltage-dependent currents control the unusual early development pattern of embryonic Renshaw cell electrical activity

Juliette Boeri, Claude Meunier, Hervé Le Corrond, Pascal Branchereau, Yulia Timofeeva, François-Xavier Lejeune, Christine Mouffle, Hervé Arulkandarajah, Jean Marie Mangin, Pascal Legendre, et al.

### ► To cite this version:

Juliette Boeri, Claude Meunier, Hervé Le Corrond, Pascal Branchereau, Yulia Timofeeva, et al.. Two opposite voltage-dependent currents control the unusual early development pattern of embryonic Renshaw cell electrical activity. *eLife*, 2021, 10, pp.e62639. 10.7554/eLife.62639 . hal-03323925v2

**HAL Id: hal-03323925**

**<https://hal.sorbonne-universite.fr/hal-03323925v2>**

Submitted on 30 Apr 2021 (v2), last revised 23 Aug 2021 (v3)

**HAL** is a multi-disciplinary open access archive for the deposit and dissemination of scientific research documents, whether they are published or not. The documents may come from teaching and research institutions in France or abroad, or from public or private research centers.

L'archive ouverte pluridisciplinaire **HAL**, est destinée au dépôt et à la diffusion de documents scientifiques de niveau recherche, publiés ou non, émanant des établissements d'enseignement et de recherche français ou étrangers, des laboratoires publics ou privés.

1           **Two opposite voltage-dependent currents control the**  
2           **unusual early development pattern of embryonic Renshaw**  
3           **cell electrical activity**

4  
5           Juliette Boeri<sup>1¶</sup>, Claude Meunier<sup>2 ¶</sup>, Hervé Le Corronc<sup>1,3 ¶</sup>, Pascal Branchereau<sup>4</sup>, Yulia  
6           Timofeeva<sup>5,6</sup>, François Xavier Lejeune<sup>7</sup>, Christine Mouffle<sup>1</sup>, Hervé Arulkandarajah<sup>1</sup>, Jean  
7           Marie Mangin<sup>1</sup>, Pascal Legendre<sup>1&\*</sup>, Antony Czarnecki<sup>1,4&\*</sup>

8  
9           **Affiliation**

10          <sup>1</sup> INSERM, UMR\_S 1130, CNRS, UMR 8246, Neuroscience Paris Seine, Institute of Biology  
11          Paris Seine, Sorbonne Univ, Paris, France.

12          <sup>2</sup> Centre de Neurosciences Intégratives et Cognition, CNRS UMR 8002, Institut  
13          Neurosciences et Cognition, Université de Paris, Paris, France.

14          <sup>3</sup> Univ Angers, Angers, France.

15          <sup>4</sup> Univ. Bordeaux, CNRS, EPHE, INCIA, UMR 5287 F-33000 Bordeaux, France

16          <sup>5</sup> Department of Computer Science and Centre for Complexity Science, University of  
17          Warwick, Coventry, UK.

18          <sup>6</sup> Department of Clinical and Experimental Epilepsy, UCL Queen Square Institute of  
19          Neurology, University College London, London, UK.

20          <sup>7</sup> Institut du Cerveau et de la Moelle Epinière, Centre de Recherche CHU Pitié-Salpêtrière,  
21          INSERM, U975, CNRS, UMR 7225, Sorbonne Univ, Paris, France.

22  
23          \* Corresponding authors

24          Email: [pascal.legendre@inserm.fr](mailto:pascal.legendre@inserm.fr) (PL)

25          Email: [antony.czarniecki@u-bordeaux.fr](mailto:antony.czarniecki@u-bordeaux.fr) (AC)

26  
27          ¶These authors contributed equally to this work.

28  
29          &These authors also contributed equally to this work.

30

31 **Abstract**

32 Renshaw cells ( $V1^R$ ) are excitable as soon as they reach their final location next to the  
33 spinal motoneurons and are functionally heterogeneous. Using multiple experimental  
34 approaches, in combination with biophysical modeling and dynamical systems theory, we  
35 analyzed, for the first time, the mechanisms underlying the electrophysiological properties  
36 of  $V1^R$  during early embryonic development of the mouse spinal cord locomotor networks  
37 (E11.5-E16.5). We found that these interneurons are subdivided into several functional  
38 clusters from E11.5 and then display an unexpected transitory involution process during  
39 which they lose their ability to sustain tonic firing. We demonstrated that the essential  
40 factor controlling the diversity of the discharge pattern of embryonic  $V1^R$  is the ratio of a  
41 persistent sodium conductance to a delayed rectifier potassium conductance. Taken  
42 together, our results reveal how a simple mechanism, based on the synergy of two voltage-  
43 dependent conductances that are ubiquitous in neurons, can produce functional diversity  
44 in embryonic  $V1^R$  and control their early developmental trajectory.

45

46 **Keywords:** development, spinal cord, embryo, Renshaw cell, firing pattern, functional  
47 involution, electrophysiology, biophysical modeling.

48

## 49 **Introduction**

50 The development of the central nervous system (CNS) follows complex steps, which  
51 depend on genetic and environmental factors and involve interactions between multiple  
52 elements of the neural tissue. Remarkably, emergent neurons begin to synchronize soon  
53 after the onset of synapse formation, generating long episodes of low frequency (<0.01 Hz)  
54 correlated spontaneous network activity (SNA) [1-8]. In the mouse embryonic spinal cord  
55 (SC), SNA is driven by an excitatory cholinergic-GABAergic loop between motoneurons  
56 (MNs) and interneurons (INs), GABA being depolarizing before embryonic day 16.5 (E16.5)  
57 [9]. SNA emerges around E12.5 [4, 6, 10-12], at a time when functional neuromuscular  
58 junctions are not yet established [13], and sensory and supraspinal inputs have not yet  
59 reached the spinal motor networks [14-17].

60 Several studies pointed out that SNA is an essential component in neuronal networks  
61 formation. [18-21]. In the SC, pharmacologically-induced disturbances of SNA between  
62 E12.5 and E14.5 induce defects in the formation of motor pools, in motor axon guidance to  
63 their target muscles and in the development of motor networks [4, 21-23]. During SNA  
64 episodes, long lasting giant depolarization potentials (GDPs) are evoked in the SC, mainly  
65 by the massive release of GABA onto MNs [12]. Immature Renshaw cells ( $V1^R$ ) are likely the  
66 first GABAergic partners of MNs in the mouse embryo [24, 25], and the massive release of  
67 GABA during SNA probably requires that many of them display repetitive action potential  
68 firing or plateau potential activity [25].

69 However, little is known about the firing pattern of embryonic  $V1^R$  and the maturation  
70 of their intrinsic properties. We recently found that  $V1^R$  exhibit heterogeneous excitability  
71 properties when SNA emerges in the SC [25] in contrast to adult Renshaw cells that  
72 constitute a functionally homogeneous population [26, 27]. Whether this early functional

73 diversity really reflects distinct functional classes of  $V1^R$ , how this diversity evolves during  
74 development, and what are the underlying biophysical mechanisms remain open questions.  
75 The present study addresses these issues using multiple approaches, including patch-clamp  
76 recordings, cluster analysis, biophysical modeling and dynamical systems theory. The firing  
77 patterns of  $V1^R$  and the mechanisms underlying their functional diversity are analyzed  
78 during a developmental period covering the initial phase of development of SC activity in  
79 the mouse embryo (E11.5-E14.5), when SNA is present, and during the critical period  
80 (E14.5-E16.5), when GABAergic neurotransmission gradually shifts from excitation to  
81 inhibition [28] and locomotor-like activity emerges [4, 10, 11].

82 We discover that the balance between the slowly inactivating subthreshold persistent  
83 sodium inward current ( $I_{Nap}$ ) [29] and the delayed rectifier potassium outward current  
84 ( $I_{Kdr}$ ), accounts for the heterogeneity of embryonic  $V1^R$  and the changes in firing pattern  
85 during development. The heterogeneity of  $V1^R$  at E12.5 arises from the existence of distinct  
86 functional groups. Surprisingly, and in opposition to the classically accepted development  
87 scheme [30-35], we show that the embryonic  $V1^R$  population loses its ability to support  
88 tonic firing from E13.5 to E15.5, exhibiting a transient functional involution during its  
89 development. Our experimental and theoretical results provide a global view of the  
90 developmental trajectories of embryonic  $V1^R$ . They demonstrate that a simple mechanism,  
91 based on the synergy of only two major opposing voltage-dependent currents, accounts for  
92 functional diversity in these immature neurons.

93

## 94 **Results**

95 **The delayed rectifier potassium current  $I_{Kdr}$  is a key partner of the persistent sodium**  
96 **current  $I_{Nap}$  in controlling embryonic  $V1^R$  firing patterns during development**

97 We previously highlighted that  $V1^R$  are spontaneously active at E12.5. Their response to  
98 a 2 s suprathreshold depolarizing current steps revealed four main patterns, depending of  
99 the recorded interneuron [25]: i) single spiking (SS)  $V1^R$  that fires only 1-3 APs at the onset  
100 of the depolarizing pulse, ii) repetitive spiking (RS)  $V1^R$ , iii) mixed events (ME)  $V1^R$  that  
101 shows an alternation of action potentials (APs) and plateau potentials or, iv)  $V1^R$  that  
102 displays a long-lasting sodium-dependent plateau potential (PP) (**Figure 1A1–A4**).

103 We also uncovered a relationship between  $I_{Nap}$  and the ability of embryonic  $V1^R$  to  
104 sustain repetitive firing [25]. However, the heterogeneous firing patterns of  $V1^R$  observed  
105 at E12.5 could not be fully explained by variations in  $I_{Nap}$  [25], suggesting the involvement  
106 of other voltage-gated channels in the control of the firing pattern of  $V1^R$ , in particular  
107 potassium channels, known to control firing and AP repolarization. Our voltage clamp  
108 protocol, performed in the presence of TTX (1  $\mu$ M), did not disclose any inward rectifying  
109 current (hyperpolarizing voltage steps to -100 mV from  $V_H = -20$  mV, data not shown), but  
110 revealed two voltage-dependent outward potassium currents, a delayed rectifier current  
111 ( $I_{Kdr}$ ) and a transient potassium current ( $I_A$ ) in all embryonic  $V1^R$ , whatever the firing  
112 pattern (**Figure 1B1–B4**). These currents are known to control AP duration ( $I_{Kdr}$ ) or firing  
113 rate ( $I_A$ ), respectively [36]. The activation threshold of  $I_{Kdr}$  lied between -30 mV and -20  
114 mV and the threshold of  $I_A$  between -60 mV and -50 mV, (n = 27; N = 27 embryos) (**Figure**  
115 **1C1–C4**). Removing external calcium had no effect on potassium current I/V curves (data  
116 not shown), suggesting that calcium-dependent potassium currents are not yet present at  
117 E12.5.

118 It was unlikely that the heterogeneity of  $V1^R$  firing patterns resulted from variations in  
119 the intensity of  $I_A$ . Indeed, its voltage-dependent inactivation (time constant:  $23.3 \pm 2.6$  ms,  
120 n = 8; N = 8), which occurs during the depolarizing phase of an AP, makes it ineffective to

121 control AP or plateau potential durations. This was confirmed by our theoretical analysis  
122 (see **Figure 7—figure supplement 1**). We thus focused our study on  $I_{Kdr}$ . At E12.5, PP V1<sup>R</sup>  
123 had a significantly lower  $G_{Kdr}$  ( $2.12 \pm 0.44$  nS,  $n = 6$ ;  $N = 6$ ) than SS V1<sup>R</sup> ( $5.57 \pm 0.56$  nS,  $n =$   
124  $9$ ;  $N = 9$ ) and RS V1<sup>R</sup> ( $6.39 \pm 0.83$  nS,  $n = 7$ ;  $N = 7$ ) (**Figure 1D**). However, there was no  
125 significant difference in  $G_{Kdr}$  between SS V1<sup>R</sup> and RS V1<sup>R</sup> at E12.5 (**Figure 1D**), which  
126 indicated that variations in  $G_{Kdr}$  alone could not explain all the firing patterns observed at  
127 E12.5. Similarly, there was no significant difference in  $G_{Nap}$  between RS V1<sup>R</sup> ( $0.91 \pm 0.21$ nS,  
128  $n = 8$ ;  $N = 8$ ) and PP V1<sup>R</sup> ( $1.24 \pm 0.19$  nS,  $n = 6$ ;  $N = 6$ ) at E12.5 (**Figure 1E**), indicating that  
129 variations in  $G_{Nap}$  alone could not explain all the firing patterns of V1<sup>R</sup> at E12.5 [25]. In  
130 contrast  $G_{Nap}$  measured in SS V1<sup>R</sup> at E12.5 ( $0.21 \pm 0.20$  nS,  $n = 9$ ;  $N = 9$ ) were significantly  
131 lower compared to  $G_{Nap}$  measured in RS V1<sup>R</sup> and in PP V1<sup>R</sup> at E12.5 (**Figure 1E**).

132 Mature neurons often display multiple stable firing patterns [37-39]. This usually  
133 depends on the combination of several outward and inward voltage- or calcium-dependent  
134 conductances and on their spatial localization [37-39]. In contrast, immature V1<sup>R</sup> have a  
135 limited repertoire of voltage-dependent currents ( $I_{Nat}$  and  $I_{Nap}$ ,  $I_{Kdr}$  and  $I_A$ ) at E12.5, and  
136 we did not find any evidence of voltage-dependent calcium currents at this age [25].  
137 Blocking  $I_{Nap}$  prevented plateau potential activity, PP-V1<sup>R</sup> becoming unexcitable, and  
138 turned repetitive spiking V1<sup>R</sup> into single spiking V1<sup>R</sup> [25]. Therefore, we hypothesized that  
139 the different firing patterns of V1<sup>R</sup> observed at E12.5 were related to the  $G_{Nap} / G_{Kdr}$  ratio  
140 only, with variations in the intensity of  $I_A$  being unlikely to account for the heterogeneity of  
141 firing pattern. We found that this ratio was significantly lower for SS V1<sup>R</sup> recorded at E12.5  
142 ( $G_{Nap} / G_{Kdr} = 0.043 \pm 0.015$ ,  $n = 9$ ) compared to RS V1<sup>R</sup> ( $0.154 \pm 0.022$ ,  $n = 8$ ) and PP V1<sup>R</sup>  
143 ( $0.66 \pm 0.132$ ,  $n = 6$ ) (**Figure 1F**). We also found that the  $G_{Nap} / G_{Kdr}$  ratio was significantly  
144 lower for RS V1<sup>R</sup> compared to PP V1<sup>R</sup> (**Figure 1F**).

145 Altogether, these results strongly suggest that, although the presence of  $I_{Nap}$  is  
146 required for embryonic  $V1^R$  to fire repetitively or to generate plateau potentials [25], the  
147 heterogeneity of the firing pattern observed between E12.5 is not determined by  $I_{Nap}$  *per*  
148 *se* but likely by the balance between  $I_{Nap}$  and  $I_{Kdr}$ .

149

### 150 **Manipulating the balance between $G_{Nap}$ and $G_{Kdr}$ changes embryonic $V1^R$ firing patterns**

151 We previously showed that blocking  $I_{Nap}$  with riluzole converted PP  $V1^R$  or RS  $V1^R$  into  
152 SS  $V1^R$  [25]. To confirm further that the balance between  $G_{Nap}$  and  $G_{Kdr}$  was the key factor  
153 in the heterogeneity of  $V1^R$  firing patterns, we assessed to what extent a given E12.5 SS  $V1^R$   
154 cell could change its firing pattern when  $I_{Kdr}$  was gradually blocked by 4-aminopyridine (4-  
155 AP). We found that  $I_{Kdr}$  could be blocked by micromolar concentrations of 4-AP without  
156 affecting  $I_A$  (**Figure 2—figure supplement 1**). 4-AP, applied at concentrations ranging from  
157 0.3  $\mu$ M to 300  $\mu$ M, specifically inhibited  $I_{Kdr}$  with an  $IC_{50}$  of 2.9  $\mu$ M (**Figure 2—figure**  
158 **supplement 1C1**).

159 We then determined to what extent increasing the concentration of 4-AP modified the  
160 firing pattern of  $V1^R$  at E12.5. Applying 4-AP at concentrations ranging from 3  $\mu$ M to 300  
161  $\mu$ M changed the firing pattern of SS  $V1^R$  ( $n = 10$ ;  $N = 10$ ) in a concentration-dependent  
162 manner (**Figure 2A1–A3**). In 50% of the recorded  $V1^R$ , increasing 4-AP concentrations  
163 successfully transformed SS  $V1^R$  into PP  $V1^R$  with the following sequence: SS  $\rightarrow$  RS  $\rightarrow$  ME  
164  $\rightarrow$  PP (**Figure 2A1**). In a second group of embryonic  $V1^R$  (25%), 4-AP application only  
165 evoked mixed activity, with the same sequence as aforementioned (SS  $\rightarrow$  RS  $\rightarrow$  ME) (data  
166 not shown). In the remaining SS  $V1^R$  (25%), increasing 4-AP concentration only led to  
167 sustained AP firing (**Figure 2A2**). Application of 300  $\mu$ M 4-AP on RS  $V1^R$  at E12.5 evoked  
168 mixed events or plateau potentials (**Figure 2—figure supplement 2**). Plateau potentials and

169 repetitive spiking evoked in the presence of 300  $\mu\text{M}$  4-AP were fully blocked by 0.5-1  $\mu\text{M}$   
170 TTX, indicating that they were generated by voltage-gated  $\text{Na}^+$  channels (**Figure 2B,C** and  
171 **Figure 2—figure supplement 2**). It should be noted that the application of 300  $\mu\text{M}$  of 4-AP  
172 induced a significant  $30.5 \pm 12.4$  % increase ( $P = 0.0137$ ; Wilcoxon test) of the input  
173 resistance ( $1.11 \pm 0.08$   $\text{G}\Omega$  versus  $1.41 \pm 0.12$   $\text{G}\Omega$ ;  $n = 11$ ;  $N = 11$ ).

174 These results show that, in addition to  $I_{\text{Nap}}$ ,  $I_{\text{Kdr}}$  is also a major determinant of the  
175 firing pattern of embryonic  $\text{V1}^{\text{R}}$ . The above suggests that the firing patterns depend on a  
176 synergy between  $I_{\text{Nap}}$  and  $I_{\text{Kdr}}$  and that the different patterns can be ordered along the  
177 following sequence  $\text{SS} \rightarrow \text{RS} \rightarrow \text{ME} \rightarrow \text{PP}$  when the ratio  $G_{\text{Nap}}/G_{\text{Kdr}}$  is increased.

178

### 179 **The heterogeneity of the $\text{V1}^{\text{R}}$ firing patterns decreases during embryonic development**

180 It was initially unclear whether these different firing patterns corresponded to well  
181 separated classes within the E12.5  $\text{V1}^{\text{R}}$  population or not. To address this question, we  
182 performed a hierarchical cluster analysis on 163 embryonic  $\text{V1}^{\text{R}}$ , based on three  
183 quantitative parameters describing the firing pattern elicited by the depolarizing pulse: the  
184 mean duration of evoked APs or plateau potentials measured at half-amplitude (mean  
185  $\frac{1}{2}\text{Ad}$ ), the variability of the event duration during repetitive firing (coefficient of variation of  
186  $\frac{1}{2}\text{Ad}$ : CV  $\frac{1}{2}\text{Ad}$ ) and the total duration of all events, expressed in percentage of the pulse  
187 duration (depolarizing duration ratio: ddr) (**Figure 3A inserts**). In view of the large  
188 dispersion of mean  $\frac{1}{2}\text{Ad}$  and ddr values, cluster analysis was performed using the (decimal)  
189 logarithm of these two quantities [40]. The analysis of the distribution of log mean  $\frac{1}{2}\text{Ad}$ , CV  
190  $\frac{1}{2}\text{Ad}$  and log ddr revealed multimodal histograms that could be fitted with several  
191 Gaussians (**Figure 3—figure supplement 1A1–C1**). Cluster analysis based on these three  
192 parameters showed that the most likely number of clusters was 5 (**Figure 3A,B**), as

193 determined by the silhouette width measurement (**Figure 3B**). Two clearly separated  
194 embryonic  $V1^R$  groups with  $CV \frac{1}{2}Ad = 0$  stood out, as shown in the 3D plot in **Figure 5C**. The  
195 cluster with the largest  $\frac{1}{2}Ad$  (mean  $\frac{1}{2}Ad = 833.5 \pm 89.99$  ms) and the largest  $ddr$  ( $0.441 \pm$   
196  $0.044$ ) contained all PP  $V1^R$  ( $n = 35$ ;  $N = 29$ ) (**Figure 3C-D** and **Figure 3—figure supplement**  
197 **1A2,C2**). Similarly, the cluster with the shortest  $\frac{1}{2}Ad$  ( $9.73 \pm 0.66$  ms) and the lowest  $ddr$   
198 ( $0.0051 \pm 0.0004$ ) contained all SS  $V1^R$  ( $n = 46$ ;  $N = 37$ ) (**Figure 3C-D** and **Figure 3—figure**  
199 **supplement 1A2,C2**).

200 The three other clusters corresponded to  $V1^R$  with nonzero values of  $CV \frac{1}{2}Ad$  (**Figure 3C**).  
201 A first cluster regrouping all RS  $V1^R$  ( $n = 69$ ;  $N = 61$ ) was characterized by smaller values of  
202  $\frac{1}{2}Ad$  ( $23.91 \pm 1.43$  ms),  $CV \frac{1}{2}Ad$  ( $27.36 \pm 1.64\%$ ) and  $ddr$  ( $0.11 \pm 0.01$ ) (**Figure 3C-D** and  
203 **Figure 3—figure supplement 1A2,C2**). The last two clusters corresponded to ME  $V1^R$   
204 (**Figure 3C,D**). The smaller cluster, characterized by a larger  $CV \frac{1}{2}Ad$  ( $170.9 \pm 8.9\%$ ;  $n = 4$ ;  $N =$   
205  $4$ ), displayed a mix of APs and short plateau potentials, while the second cluster, with  
206 smaller  $CV \frac{1}{2}Ad$  ( $87.61 \pm 7.37\%$ ;  $n = 9$ ;  $N = 9$ ), displayed a mix of APs and long-lasting  
207 plateau potentials (**Figure 3D** and **Figure 3—figure supplement 1B2**). Their  $\frac{1}{2}Ad$  and  $ddr$   
208 values were not significantly different (**Figure 3—figure supplement 1A2,C2**).

209 It must be noted that three embryonic  $V1^R$  (1.8%) were apparently misclassified since  
210 they were aggregated within the RS cluster although having zero  $CV \frac{1}{2}Ad$  (**Figure 3C**;  
211 **arrows**). Examination of their firing pattern revealed that this was because they generated  
212 only two APs, although their  $ddr$  (0.16 to 0.2) and  $\frac{1}{2}Ad$  values (31.6 to 40.3 ms) were well  
213 in the range corresponding of the RS cluster.

214 These different firing patterns of  $V1^R$  might reflect different states of neuronal  
215 development [31, 41-43]. Single spiking and/or plateau potentials are generally believed to  
216 be the most immature forms of firing pattern, repetitive spiking constituting the most

217 mature form [19, 44]. If it were so, the firing patterns of embryonic  $V1^R$  would evolve  
218 during embryonic development from single spiking or plateau potential to repetitive  
219 spiking, this latter firing pattern becoming the only one in neonates [26] and at early  
220 postnatal stages [27]. However, RS neurons already represent 41% of  $V1^R$  at E12.5. We  
221 therefore analyzed the development of firing patterns from E11.5, when  $V1^R$  terminate  
222 their migration and reach their final position [45], to E16.5. This developmental period  
223 covers a first phase of development (E11.5-E14.5), where lumbar spinal networks exhibit  
224 SNA, and a second phase (E14.5-E16.5), where locomotor-like activity emerges [4, 11, 46,  
225 47]. We first analyzed changes in the intrinsic properties (input capacitance  $C_{in}$ , input  
226 resistance  $R_{in} = 1/G_{in}$  and spike voltage threshold) of  $V1^R$ .  $C_{in}$  did not change significantly  
227 from E11.5 to E13.5 (**Figure 4A1**), remaining of the order of 12 pF, in agreement with our  
228 previous work [25]. However, it increased significantly at the transition between the two  
229 developmental periods (E13.5-E15.5) to reach about 23.5 pF at E15.5 (**Figure 4A1**). A  
230 similar developmental pattern was observed for  $R_{in}$ , which remained stable during the  
231 first phase from E11.5 to E14.5 ( $R_{in} \approx 1-1.2 \text{ G}\Omega$ ) but decreased significantly after E14.5 to  
232 reach about 0.7  $\text{G}\Omega$  at E15.5 (**Figure 4A2**). Spike threshold also decreased significantly  
233 between the first and the second developmental phases, dropping from about -34 mV at  
234 E12.5 to about -41 mV at E16.5 (**Figure 4A3**). Interestingly, this developmental transition  
235 around E14.5 correspond to the critical stage at which SNA gives way to a locomotor-like  
236 activity [11, 46, 47] and rhythmic activity becomes dominated by glutamate release rather  
237 than acetylcholine release [4].

238 This led us to hypothesize that this developmental transition could be also critical for  
239 the maturation of  $V1^R$  firing patterns. The distinct firing patterns observed at E12.5 were  
240 already present at E11.5 (**Figure 4B1,C**), but the percentage of RS  $V1^R$  strongly increased

241 from E11.5 to E12.5, while the percentage of ME V1<sup>R</sup> decreased significantly (**Figure 4C**).  
242 The heterogeneity of V1<sup>R</sup> firing patterns then substantially diminished. Plateau potentials  
243 were no longer observed at E13.5 (**Figure 4B2,C**), and ME V1<sup>R</sup> disappeared at E14.5 (**Figure**  
244 **4B3,C**). Interestingly, the proportion of SS V1<sup>R</sup> remained high from E13.5 to E15.5 and even  
245 slightly increased (91.23% at E14.5 and 93.33% at E15.5; **Figure 4C**). This trend was partially  
246 reversed at E16.5, as the percentage of RS V1<sup>R</sup> increased at the expense of SS V1<sup>R</sup> (67.86%  
247 SS V1<sup>R</sup> and 32.34% RS V1<sup>R</sup>; **Figure 4B5,C**). This decrease in repetitive firing capability after  
248 E13.5 was surprising in view of what is classically admitted on the developmental pattern  
249 of neuronal excitability [18, 48]. Therefore, we verified that it did not reflect the death of  
250 some V1<sup>R</sup> after E13.5. Our data did not reveal any activated caspase3 (aCaspase3) staining  
251 in V1<sup>R</sup> (FoxD3 staining) at E14.5 (n = 10 SCs; N = 10) (**Figure 5**), in agreement with previous  
252 reports showing that developmental cell death of V1<sup>R</sup> does not occur before birth [49].

253 To determine whether  $G_{Nap}$  and  $G_{Kdr}$  also controlled the firing pattern of V1<sup>R</sup> at E14.5  
254 (see **Figure 4B3,C**), we assessed the presence of  $I_{Nap}$  and  $I_{Kdr}$  in single spiking V1<sup>R</sup> at this  
255 embryonic age. Both  $I_{Nap}$  and  $I_{Kdr}$  were present in V1<sup>R</sup> at E14.5 (**Figure 6—figure**  
256 **supplement 1 and Figure 6—figure supplement 2**) whereas, as in V1<sup>R</sup> at E12.5, no calcium-  
257 dependent potassium current was detected at this developmental age (not shown). In SS  
258 V1<sup>R</sup>,  $G_{Kdr}$  was significantly higher at E14.5 ( $11.11 \pm 1.12$  nS, n = 10; N = 10) than at E12.5  
259 (**Figure 1D**). In contrast,  $G_{Nap}$  was similar at E14.5 ( $0.13 \pm 0.14$  nS, n = 10; N = 10) and E12.5  
260 (**Figure 1E**). We also found that the  $G_{Nap} / G_{Kdr}$  ratio was significantly lower for SS V1<sup>R</sup>  
261 recorded at E14.5 ( $0.012 \pm 0.004$ , n = 10) compared to RS V1<sup>R</sup> ( $0.154 \pm 0.022$ , n = 8) and PP  
262 V1<sup>R</sup> ( $0.66 \pm 0.132$ , n = 6) recorded at E12.5 (**Figure 1F**).

263 We tested the effect of 4-AP in SS V1<sup>R</sup> at E14.5. At this embryonic age, 300  $\mu$ M 4-AP  
264 inhibited only 59.2% of  $I_{Kdr}$ . Increasing 4-AP concentration to 600  $\mu$ M did not inhibit  $I_{Kdr}$

265 significantly more (60.2%) (**Figure 6—figure supplement 2**), indicating that inhibition of  
266  $I_{Kdr}$  by 4-AP reached a plateau at around 300  $\mu\text{M}$ . 600  $\mu\text{M}$  4-AP application had no  
267 significant effect on  $I_A$  (**Figure 6—figure supplement 2**). The application of the maximal  
268 concentration of 4-AP tested (600  $\mu\text{M}$ ) converted SS  $V1^R$  ( $n = 13$ ;  $N = 13$ ) to PP  $V1^R$  (23.1%;  
269 **Figure 6A1,B**), RS  $V1^R$  (38.5%; **Figure 6A2,B**) or ME  $V1^R$  (38.4%; **Figure 6B**), as was observed  
270 at E12.5, thus indicating that the firing pattern of  $V1^R$  depends on the balance between  
271  $I_{Nap}$  and  $I_{Kdr}$  also at E14.5. Plateau potential and repetitive spiking recorded in the  
272 presence of 4-AP at E14.5 were fully blocked by 0.5-1  $\mu\text{M}$  TTX indicating that they were  
273 generated by voltage-gated sodium channels (**Figure 6A1,A2**), as observed at E12.5.

274

#### 275 **Theoretical analysis: the basic model**

276 As shown in **Figure 7A** for 26 cells, in which both  $G_{Nap}$  and  $G_{Kdr}$  were measured, the  
277 three largest clusters revealed by the hierarchical clustering analysis (SS, RS and PP, which  
278 account together for the discharge of more than 95% of cells, see **Figure 5**) correspond to  
279 well defined regions of the  $G_{Nap}$ -  $G_{Kdr}$  plane. Single spiking is observed only when  $G_{Nap}$  is  
280 smaller than 0.6 nS. For larger values of  $G_{Nap}$ , repetitive spiking occurs when  $G_{Kdr}$  is larger  
281 than 3.5 nS, and  $V1^R$  display plateau potentials when  $G_{Kdr}$  is smaller than 3.5 nS. Mixed  
282 events (ME, 4.5% of the 163 cells used in the cluster analysis), where plateaus and spiking  
283 episodes alternate, are observed at the boundary of RS and PP clusters. This suggested to  
284 us that a conductance-based model incorporating only the leak current,  $I_{Nat}$ ,  $I_{Nap}$  and  $I_{Kdr}$   
285 (see Materials and Methods) could account for most experimental observations, the  
286 observed zonation being explained in terms of bifurcations between the different stable  
287 states of the model. Therefore, we first investigated a simplified version of the model  
288 without  $I_A$  and slow inactivation of  $I_{Nap}$ .

289 A one-parameter bifurcation diagram of this “basic” model is shown in **Figure 7B** for two  
290 values of  $G_{Kdr}$  (2.5 nS and 10 nS) and a constant injected current  $I = 20$  pA. In both cases,  
291 the steady-state membrane voltage (stable or unstable) and the peak and trough voltages  
292 of stable and unstable periodic solutions are shown as the function of the maximal  
293 conductance  $G_{Nap}$  of the  $I_{Nap}$  current, all other parameters being kept constant. For  $G_{Kdr}$   
294 = 10 nS, the steady-state membrane voltage progressively increases (in gray) with  $G_{Nap}$ ,  
295 but repetitive spiking (in red, see voltage trace for  $G_{Nap} = 1.5$  nS) is not achieved until  $G_{Nap}$   
296 reaches point  $SN_1$ , where a saddle node (SN) bifurcation of limit cycles occurs. This fits with  
297 the experimental data, where a minimal value of  $G_{Nap}$  is required for repetitive spiking  
298 (see also [25]), and is in agreement with the known role of  $I_{Nap}$  in promoting repetitive  
299 discharge [50, 51]. Below  $SN_1$ , the model responds to the onset of a current pulse by firing  
300 only one spike before returning to quiescence (see voltage trace for  $G_{Nap} = 0.2$  nS), or a few  
301 spikes when close to  $SN_1$  (not shown) before returning to quiescence. The quiescent state  
302 becomes unstable through a subcritical Hopf bifurcation (HB) at point  $HB_1$ , with bistability  
303 between quiescence and spiking occurring between  $SN_1$  and  $HB_1$  points. Repetitive firing  
304 persists when  $G_{Nap}$  is increased further and eventually disappears at point  $SN_2$ . The firing  
305 rate does not increase much throughout the RS range (**Figure 7—figure supplement 1C**),  
306 remaining between 20.1 Hz (at  $SN_1$ ) and 28.7 Hz (at  $SN_2$ ). A stable plateau appears at point  
307  $HB_2$  through a subcritical HB. The model is bistable between  $HB_2$  and  $SN_2$ , with plateau and  
308 large amplitude APs coexisting in this range.

309 The model behaves very differently when  $G_{Kdr}$  is reduced to 2.5 nS (gray-blue curve in  
310 **Figure 7B**). It exhibits a unique stable fixed point whatever the value of  $G_{Nap}$  is, and the  
311 transition from quiescence to plateau is gradual as  $G_{Nap}$  is increased. No repetitive spiking  
312 is ever observed. This indicates that the activity pattern is controlled not only by  $G_{Nap}$  but

313 also by  $G_{Kdr}$ . This is demonstrated further in **Figure 7C**, where  $G_{Nap}$  was fixed at 1.2 nS  
314 while  $G_{Kdr}$  was increased from 0 to 25 nS. The model exhibits a plateau potential until  
315  $G_{Kdr}$  is increased past point the subcritical HB point HB<sub>2</sub>, repetitive spiking sets in before at  
316 point SN<sub>2</sub> via a SN of limit cycles bifurcation. When  $G_{Kdr}$  is further increased, repetitive  
317 firing eventually disappears through a SN bifurcation of limit cycles at point SN<sub>1</sub>, the  
318 quiescent state becomes stable through a subcritical HB at point HB<sub>1</sub>, and bistability occurs  
319 between these two points. This behavior is in agreement with **Figure 7A**.

320 Since both conductances  $G_{Nap}$  and  $G_{Kdr}$  control the firing pattern of embryonic V1<sup>R</sup> cells,  
321 we computed a two-parameters bifurcation diagram (**Figure 7D**), where the stability  
322 regions of the different possible activity states and the transition lines between them are  
323 plotted in the  $G_{Nap} - G_{Kdr}$  plane. The black curves correspond to the bifurcations HB<sub>1</sub> and  
324 HB<sub>2</sub> and delimit a region where only repetitive firing occurs. The red curves correspond to  
325 the SN bifurcations of periodic orbits associated with the transition from quiescence to  
326 firing (SN<sub>1</sub>) and the transition from plateau to firing (SN<sub>2</sub>). They encompass a region  
327 (shaded area) where repetitive firing can be achieved but may coexist with quiescence  
328 (between the HB<sub>1</sub> and SN<sub>1</sub> lines) or plateau potential (in the narrow region between the  
329 HB<sub>2</sub> and SN<sub>2</sub> lines).

330 Some important features of the diagram must be emphasized: 1) minimal values of both  
331  $G_{Nap}$  (to ensure sufficient excitability) and  $G_{Kdr}$  (to ensure proper spike repolarization) are  
332 required for repetitive spiking, 2) quiescence and plateau can be clearly distinguished only  
333 when they are separated by a region of repetitive spiking (see also **Figure 7B** for  $G_{Kdr} = 10$   
334 nS), otherwise the transition is gradual (**Figure 7B** for  $G_{Kdr} = 2.5$  nS), 3) only oblique lines  
335 with an intermediate slope cross the bifurcation curve and enter the RS region (see, for  
336 example, the red line in **Figure 7D**). This means that repetitive spiking requires an

337 appropriate balance between  $I_{Nap}$  and  $I_{Kdr}$ . If the ratio  $G_{Nap}/G_{Kdr}$  is too large (blue line)  
338 or too small (gray line), only plateau potentials or quiescence will be observed at steady  
339 state. This is exactly what is observed in experiments, as shown by the cumulative  
340 distribution function of the ratio  $G_{Nap}/G_{Kdr}$  for the different clusters of embryonic  $V1^R$  in  
341 **Figure 7E** (same cells as in **Figure 7A**). The ratio increases according to the sequence SS →  
342 RS → ME → PP, with an overlap of the distributions for SS  $V1^R$  and RS  $V1^R$ . Note also that  
343 the ratio for ME cells (around 0.25) corresponds to the transition between repetitive  
344 spiking and plateau potentials (more on this below).

345 Embryonic  $V1^R$  cells display voltage fluctuations that may exceed 5 mV and are  
346 presumably due to channel noise. The relatively low number of sodium and potassium  
347 channels (of the order of a few thousands) led to voltage fluctuations in the stochastic  
348 version of our model comparable to those seen experimentally when the cell was  
349 quiescent (top voltage trace in **Figure 7D**) or when a voltage plateau occurred (bottom  
350 trace). Channel noise caused some jitter during repetitive spiking (middle trace), and  
351 induced clearly visible variations in the amplitude of APs. However, repetitive firing proved  
352 to be very robust and was not disrupted by voltage fluctuations. Altogether, channel noise  
353 little alters the dynamics (compare the deterministic voltage traces in **Figure 7B** and the  
354 noisy traces in **Figure 7D**). This is likely because channel noise has a broad power spectrum  
355 and displays no resonance with the deterministic solutions of the model.

356 The one-parameter bifurcation diagram of the model was not substantially modified  
357 when we took  $I_A$  into account, as shown in **Figure 6—figure supplement 1**. It just elicited a  
358 slight membrane hyperpolarization, an increase in the minimal value of  $G_{Nap}$  required for  
359 firing, and a decrease of the firing frequency. The transition from repetitive firing to  
360 plateau was not affected because  $I_A$  is then inactivated by depolarization.

361 The bifurcation diagram of **Figure 7D** accounts *qualitatively* for the physiological data on  
362  $V1^R$  at E12.5 presented in **Figure 7A**, as shown in **Figure 7F** where the conductance data of  
363 **Figure 7A** were superimposed on it. However, one must beware of making a more  
364 *quantitative* comparison because the theoretical bifurcation diagram was established for a  
365 constant injected current of 20 pA, whereas the current injected in experiments data  
366 varied from neuron to neuron and ranged from 10 to 30 pA in the sample shown in **Figure**  
367 **7A**. The position of bifurcation lines in the  $G_{Nap} - G_{Kdr}$  plane depends not only on the value  
368 of the injected current, but on the values chosen for the other parameters, which also vary  
369 from cell to cell but were kept at fixed values in the model [52]. For instance, the diagrams  
370 were computed in **Figure 7D,F** for  $G_{in} = 1$  nS and  $C_{in} = 13$  pF, the median values of the input  
371 conductance and capacitance at E12.5, taking no account of the cell-to-cell variations of  
372 these quantities. Between E12.5 and E14.5,  $C_{in}$  which provides an estimate of the cell size,  
373 increases by 38% in average, whereas  $G_{in}$  is not significantly modified (see **Figure 4**). As  
374 illustrated in **Figure 7G** the two-parameters bifurcation diagram is then shifted upward and  
375 rightward compared to **Figure 7F**, because larger conductances are required to obtain the  
376 same firing pattern. The observed regression of excitability from E12.5 to E14.5-E15.5 (see  
377 **Figure 4C**) thus comes from a decrease in  $G_{Nap}$  density (see presumable developmental  
378 trajectories indicated by arrows in **Figure 7F**) together with a shift of the RS region as cell  
379 size increases. As a result, all 10 cells shown in **Figure 7G** are deeply inside the SS region at  
380 E14.5.

381 It is less straightforward to explain on the basis of our model the experiments where 4-  
382 AP changed the firing pattern of SS  $V1^R$  (**Figure 2**). Indeed, the decrease of  $G_{Kdr}$  (**Figure 6—**  
383 **figure supplement 2**), although it may exceed 70% at the higher concentrations of 4-AP we  
384 used, is not sufficient by itself to account for the change in the firing pattern of  $V1^R$  (**Figure**

385 **6—figure supplement 2**) because data points in the SS cluster will not cross the bifurcation  
386 lines between SS and RS (SN1) and between RS and PP (SN2) when displaced downward in  
387 the  $G_{Nap}$ - $G_{Kdr}$  plane. However, 4-AP at a 300  $\mu$ M concentration also decreases  $G_{in}$  (by 23%  
388 in average and up to 50% in some neurons), the rheobase current with it, and the current  
389 that was injected in cells during experiments was reduced accordingly. When we take into  
390 account this reduction of both  $G_{in}$  and  $I$  the two parameters bifurcation diagram of the  
391 model remains qualitatively the same, but it is shifted leftward and downward in the  $G_{Nap}$ -  
392  $G_{Kdr}$  plane (**Figure 6—figure supplement 2**). As a consequence, the bifurcation lines  
393 between SS and RS and between RS and PP (SN2) are then successively crossed when  
394  $G_{Kdr}$  is reduced, in accordance with experimental results.

395

#### 396 **Theoretical analysis: slow inactivation of $I_{Nap}$ and bursting**

397 Our basic model accounts for the firing pattern of 73% of the 163 cells used in the  
398 cluster analysis. However, bursting, under the form of recurring plateaus separated by brief  
399 repolarization episodes (see a typical trace in **Figure 8A left**), was experimentally observed  
400 in half of PP V1<sup>R</sup> (24 out of 46), and plateaus intertwined with spiking episodes were  
401 recorded in the 13 cells of the ME cluster (8% of the total sample, see **Figure 8A right** for a  
402 typical example). Recurrent plateaus indicate membrane bistability and require that the  
403  $I - V$  curve be S-shaped. This occurs when  $G_{Nap}$  is large and  $G_{Kdr}$  small. (**Figure 8B1,B2**).  
404 However, our basic model lacks a mechanism for switching between quiescent state and  
405 plateau, even in this case. Channel noise might induce such transitions, but our numerical  
406 simulations showed that this is too infrequent to account for bursting (see voltage trace in  
407 **Figure 8B1** where the plateau state is maintained despite channel noise).

408 To explain recurrent plateaus during a constant current pulse, we have to incorporate in  
409 our model an additional slow dynamical process. Therefore, we took into account the slow  
410 inactivation of  $I_{Nap}$  that is observed in experiments.  $I_{Kdr}$  also inactivates slowly but over  
411 times that are much longer than the timescale of bursting, which is why we did not take its  
412 slow inactivation into account. The one-parameter bifurcation diagram of the basic model  
413 without slow inactivation of  $I_{Nap}$  is shown in **Figure 8C** for  $G_{Kdr} = 5$  nS and an injected  
414 current reduced to 10 pA (as compared to 20 pA in the previous section), so as to allow for  
415 bistability (see **Figure 8B2**). The  $G_{Nap} - V$  curve is then S-shaped, as shown in **Figure 8B1**,  
416 with a bistability region for  $G_{Nap}$  between 1.36 and 1.85 nS. This is in contrast with **Figure**  
417 **7B** where the  $G_{Nap} - V$  curve was monotonic. Adding the slow (de)inactivation of  
418  $I_{Nap}$  then causes periodic transitions between up (plateau) and down (quiescent) states, as  
419 illustrated by the top voltage trace on the right of **Figure 8C**, and the model displayed a  
420 stable limit cycle (shown in black in the bifurcation diagram on the left of **Figure 8C**). This  
421 mechanism is known as pseudo-plateau or plateau-like bursting (a.k.a. fold-subcritical HB  
422 bursting) [53]. In contrast with square wave bursting [54-57], where the up-state is a stable  
423 limit cycle arising from a supercritical Hopf bifurcation [58-60], the up-state here is a stable  
424 fixed point (which coexists with an unstable limit cycle). This is why one does not observe  
425 bursts of APs separated by quiescent periods as, for instance, observed in postnatal CA1  
426 Pyramidal cells [61] and in neurons of neonatal pre-Bötzinger Complex [62, 63], but  
427 recurrent plateaus. The duration of the plateaus and repolarization episodes depends on  
428 the values of  $G_{Nap}$  and  $G_{Kdr}$ . A voltage-independent time constant  $\tau_s = 2$  ms leads to up  
429 and down states of comparable durations (see top left voltage trace in **Figure 8C**). In  
430 agreement with the bifurcation diagram of **Figure 8C**, the persistent sodium current  
431 inactivates during plateaus (phase 1, see bottom right trace in **Figure 8C**) and de-

432 inactivates during quiescent episodes (phase 3, see bottom right trace). Transitions from  
433 the down-state to the up-state occurs when inactivation has reached its maximal value  
434 (phase 2) and transition from the up-state to the down state when it has reached its  
435 maximum (phase 4). Adding channel noise preserves bursting but introduces substantial  
436 randomness in the duration of plateaus and repolarization episodes (bottom left voltage  
437 trace in **Figure 8C**). Moreover, it substantially decreases the duration of both plateaus and  
438 quiescent episodes by making transition between the two states easier (compare the top  
439 and bottom voltage traces on the left, both computed for  $\tau_s = 2 \text{ ms}$ ).

440 Increasing  $G_{Nap}$  (or decreasing  $G_{Kdr}$ ) makes plateaus much longer than quiescent  
441 episodes (see bottom right voltage trace in **Figure 8C**). This again points out to the fact that  
442 the ratio is an important control parameter. We also noted that adding the  $I_A$  current  
443 lengthened the quiescence episodes (**Figure 6-figure supplement 1**).

444 Slow inactivation of  $I_{Nap}$  also provides an explanation for mixed patterns, where  
445 plateaus alternate with spiking episodes (**Figure 8A, right**). They take place in our model  
446 near the transition between repetitive spiking and plateau, as in experiments (see **Figure**  
447 **8A**). Slow inactivation can lead to elliptic bursting, notably when the bifurcation  $HB_2$  is  
448 subcritical [64, 65], which is the case here (**Figure 8D**). The model then displays a stable  
449 limit cycle with alternating plateaus and spiking episodes, arising from crossing the  
450 bifurcation points  $HB_2$  and  $SN_2$  back and forth (see bifurcation diagram in **Figure 8D** and  
451 top voltage trace). We note that sufficient de-inactivation of  $I_{Nap}$  for triggering a new  
452 plateau (phase 3 in the bottom trace of **Figure 8D**) may be difficult to achieve during  
453 spiking episodes, because voltage oscillates over a large range, which tends to average out  
454 the variations of the inactivation level. If de-inactivation is not sufficient, the model keeps  
455 on spiking repetitively without returning to the plateau state. This is what occurs for cells

456 well within the RS region, far away from the RS-PP transition. It also probably explains why  
457 it was difficult in many recorded cells to elicit plateaus by increasing the injected current,  
458 inactivation balancing then the increase of  $I_{Nap}$  induced by the larger current.

459 Altogether, our study shows that a model incorporating the slow inactivation of  
460  $I_{Nap}$  accounts for all the firing patterns displayed by cells from the PP and ME clusters.

461

## 462 **Discussion**

463  $V1^R$  constitute a homogeneous population when referring to their transcription factor  
464 program during development [24, 66], their physiological function [67] and their firing  
465 pattern at postnatal stages [27]. Surprisingly, our electrophysiological recordings and our  
466 cluster analysis clearly indicate that distinct functional classes of  $V1^R$  are transiently  
467 present during development at the onset of the SNA (E11.5-E12.5). Five different groups of  
468 embryonic  $V1^R$  were defined using cluster analysis, according to their firing properties.

469

### 470 **Development of the firing pattern of embryonic $V1^R$ during SNA**

471 It is generally assumed that, during early development, newborn neurons cannot sustain  
472 repetitive firing [35, 48]. Later on, neurons progressively acquire the ability to fire  
473 repetitively, APs become sharper, and neurons eventually reach their mature firing pattern,  
474 due to the progressive appearance of a panoply of voltage-gated channels with different  
475 kinetics [18, 35, 48]. Our results challenge the general view that single spiking is a more  
476 primitive form of excitability [35]. Indeed, we show that repetitive firing and plateau  
477 potentials dominated at early stages (E11.5-E12.5), while single spiking was prevailing only  
478 later (E13.5- E16.5).

479 The different V1<sup>R</sup> firing patterns observed at E11.5-E12.5 might reflect variability in the  
480 maturation level between V1<sup>R</sup> at a given developmental stage, as suggested for developing  
481 MNs [68, 69]. However, this is unlikely since V1<sup>R</sup> transiently lose their ability to sustain  
482 tonic firing or plateau potential after E13.5. The heterogeneous discharge patterns of V1<sup>R</sup>  
483 observed before E13.5 contrasts with the unique firing pattern of V1<sup>R</sup> at postnatal age [27].  
484 Accordingly, the transient functional heterogeneity of V1<sup>R</sup> rather reflects an early initial  
485 developmental stage (E11.5-E13.5) of intrinsic excitability.

486 The physiological meaning of the transient functional involution of V1<sup>R</sup> that follows,  
487 after E12.5, is puzzling. To our knowledge, such a phenomenon was never described in  
488 vertebrates during CNS development. So far, a functional involution was described only for  
489 inner hair cells between E16 and P12 [70, 71] and cultured oligodendrocytes [72], and it  
490 was irreversible. Because most V1<sup>R</sup> cannot sustain tonic firing after E12.5, it is likely that  
491 their participation to SNA is limited to the developmental period before other GABAergic  
492 interneuron subtypes mature and start to produce GABA and glycine [73]. Interestingly,  
493 embryonic V1<sup>R</sup> begin to recover their capability to sustain tonic firing when locomotor-like  
494 activity emerges [4, 11], a few days before they form their recurrent synaptic loop with  
495 MNs (around E18.5 in the mouse embryos, [74]). One possible function of the transient  
496 involution between E12.5 and E15.5 could be to regulate the growth of V1<sup>R</sup> axons toward  
497 their targets. It is indeed known that low calcium fluctuations within growth cones are  
498 required for axon growth while high calcium fluctuations stop axon growth and promote  
499 growth cone differentiation [75].

500

501 **Ion channels mechanisms underlying the functional heterogeneity of embryonic V1<sup>R</sup>**

502 Blockade of  $I_{Nap}$  leads to single spiking [25], which emphasizes the importance of this  
503 current for the occurrence of repetitive firing and plateau potentials in  $V1^R$  at early  
504 developmental stages. But these neurons can also switch from one firing pattern to  
505 another, when  $G_{Kdr}$  is decreased by 4-AP, which emphasizes the importance of  $I_{Kdr}$ . We  
506 found that the main determinant of embryonic  $V1^R$  firing pattern is the balance between  
507  $G_{Nap}$  and  $G_{Kdr}$ .

508 A Hodgkin-Huxley-type model incorporating a persistent sodium current  $I_{Nap}$  provided a  
509 parsimonious explanation of all five firing patterns recorded in the  $V1^R$  population at E12.5.  
510 It provided a mathematical interpretation for the clustering of embryonic  $V1^R$  shown by the  
511 hierarchical analysis and accounted for the effect of 4-AP and riluzole [25] on the discharge.  
512 Remarkably, it highlighted how a simple mechanism involving only the two opposing  
513 currents  $I_{Nap}$  and  $I_{Kdr}$ , but not  $I_A$ , could produce functional diversity in a population of  
514 developing neurons. The model explained why minimal  $G_{Nap}$  and  $G_{Kdr}$  are required for  
515 firing, and how a synergy between  $G_{Nap}$  and  $G_{Kdr}$  controls the firing pattern and accounts  
516 for the zonation of the  $G_{Nap} - G_{Kdr}$  plane that is observed experimentally.

517 Taking into account the slow inactivation of  $I_{Nap}$  to the model allowed us to explain the  
518 bursting patterns displayed by cells of the PP and ME clusters. We showed, in particular,  
519 that mixed events arose from elliptic bursting at the repetitive spiking-plateau transition  
520 and that smooth repetitive plateaus could be explained by a pseudo-plateau bursting  
521 mechanism [53, 59]. Such bursting scenario has been previously studied in models of  
522 endocrine cells [58, 76, 77] and adult neurons [78], but rarely observed in experiments [79].  
523 It contrasts with the more common square wave bursting at firing onset, i.e. alternating  
524 bursts of APs and quiescent episodes, on which most studies of bursting focused [61-63].  
525 Our model can also display such square wave bursting, but this occurs for physiologically

526 realistic parameter values, and did not dwell on that bursting mode that we never  
527 observed in embryonic  $V1^R$ . The model also provides a mathematical explanation for mixed  
528 events, where bursts of APs alternate with plateau episodes. It is due to an elliptic bursting  
529 scenario at the RS-PP transition, a firing range that the afore-mentioned studies did not  
530 examine. This further emphasizes the capacity of our simple model to account for a wide  
531 diversity of firing patterns.

532 Pseudo-plateau bursting has also been observed in the embryonic pre-Böttinger  
533 network [79]. However, it is produced there by the calcium-activated nonselective cationic  
534 current  $I_{CAN}$ , while  $I_{Nap}$  leads to square wave bursting. Pseudo-plateau bursting, displayed  
535 by half of the cells at E16.5 largely disappears at E18.5 because of the change in the  
536 balance between  $I_{CAN}$  and  $I_{Nap}$  during embryonic maturation [79]. Such a scenario cannot  
537 account for the variety of discharge patterns observed in embryonic  $V1^R$  at the E11.5-12.5  
538 stage of development. Our theoretical analysis and our experimental data clearly indicate  
539 that the interplay between two opposing currents is necessary to explain all the firing  
540 patterns of  $V1^R$ . Our model is of course not restricted to embryonic  $V1^R$ , but may also apply  
541 to any electrically compact cell, the firing activity of which is dominated by  $I_{Nap}$  and  
542 delayed rectifier potassium currents. This is the case of many classes of embryonic cells in  
543 mammals at an early stage of their development. It can also apply to the axon initial  
544 segment, where  $G_{Nap}$  and  $G_{Kdr}$  are known to play the major role in the occurrence of  
545 repetitive firing [80].

546 Altogether our experimental and theoretical results provide a global view of the  
547 developmental trajectories of embryonic  $V1^R$  (see **Figure 7F, G**). At E12.5, conductances of  
548 embryonic  $V1^R$  are widely spread in the  $G_{Nap} - G_{Kdr}$  plane, which explains the  
549 heterogeneity of their firing patterns. This likely results from the random and uncorrelated

550 expression of sodium and potassium channels from cell to cell at this early stage. Between  
551 E12.5 and E14.5-15.5 cell size increases, and  $G_{Kdr}$  with it, while the density of sodium  
552 channels decreases (see **Figures 1 and 4**). The functional involution displayed by  $V1^R$   
553 between E12.5 and E15.5 thus mainly results from a decrease of  $G_{Nap}$  coordinated with an  
554 increase of  $G_{Kdr}$ . How these synergistic processes are controlled during this developmental  
555 period remains an open issue.

556 It is important to note that the presence of  $I_{Nap}$  is required for the functional diversity  
557 of  $V1^R$ . Indeed, in the absence of  $I_{Nap}$ ,  $V1^R$  lose their ability to generate plateau potentials  
558 or to fire repetitively. More generally, when the diversity of voltage-gated channels is  
559 limited, as observed in embryonic neurons [18], changes in the balance between  $I_{Kdr}$  and  
560 non (or poorly) inactivating inward current can modify the firing pattern. This can be  
561 achieved not only by  $I_{Nap}$ , but also by other slowly or non-inactivating inward  
562 conductances, such as  $I_{CAN}$  [79]. Our work also clearly indicates that a change in the firing  
563 pattern can only occur if a change in inward conductances cannot be counterbalanced by a  
564 corresponding change in outward conductances. This implies that there is no homeostatic  
565 regulation of channel density to ensure the robustness of  $V1^R$  excitability during its early  
566 development, contrarily to the mature CNS [37]. In addition, the poor repertoire of  
567 voltage-gated channels at this developmental stage precludes channel degeneracy, which  
568 is also known to ensure the robustness of excitability in mature neurons [37].

569 In conclusion, our study shows that there is no universal pattern of development in  
570 embryonic neurons, and it demonstrates that a simple general mechanism involving only  
571 two slowly inactivating voltage-gated channels with opposite effects is sufficient to  
572 produce

573 a wide variety of firing patterns in immature neurons having a limited repertoire of  
574 voltage-gated channels.  
575

Key Resources Table				
Reagent type (species) or resource	Designation	Source or reference	Identifiers	Additional information
genetic reagent (M. musculus Swiss) male and female	GAD1 <sup>GFP</sup>	PMID: 14574680		a cDNA encoding enhanced GFP (eGFP) was targeted to the locus encoding the gene Gad1.
Antibody	Anti-FoxD3 (Guinea pig polyclonal)	PMID:19088088		IF(1:5000)
Antibody	Anti-cleaved Caspase-3 (Asp175) (Rabbit polyclonal)	Cell Signaling Technology	Cat# 9661, RRID: AB_2341188	IF(1:1000)
chemical compound, drug	Tetrodotoxin	Alomone labs	Cat# T550, CAS No.: 18660-81-6	1 $\mu$ M
chemical compound, drug	4-aminopyridine	Sigma-Aldrich	Cat# A78403, CAS No.: 504-24-5	0.3 - 600 $\mu$ M
software, algorithm	pCLAMP 10.5	Molecular devices	RRID:SCR_014284	
software, algorithm	Axograph 1.7.2	AxoGraph	RRID:SCR_014284	
software, algorithm	PRISM 7.0e	GraphPad Software	RRID:SCR_002798)	
software, algorithm	ImageJ 1.5	N.I.H. (USA)	RRID:SCR_003070	

software, algorithm	Adobe Photoshop CS6	Adobe, USA	RRID:SCR_014199	
software, algorithm	R software 3.3.2	Cran project ( <a href="https://cran.r-project.org/">https://cran.r-project.org/</a> )	RRID:SCR_001905	
software, algorithm	XPP-Aut 8.0	University of Pittsburgh; Pennsylvania; USA	RRID:SCR_001996	

578

579 **Isolated spinal cord preparation**

580 Experiments were performed in accordance with European Community guiding principles  
581 on the care and use of animals (86/609/CEE, CE Off J no. L358, 18 December 1986), French  
582 decree no. 97/748 of October 19, 1987 (J Off République Française, 20 October 1987, pp.  
583 12245-12248). All procedures were carried out in accordance with the local ethics  
584 committee of local Universities and recommendations from the CNRS. We used Gad1<sup>GFP</sup>  
585 knock-in mice to visualize putative GABAergic INs [81], as in our previous study [25]. To  
586 obtain E12.5-E16.5 Gad1<sup>GFP</sup> embryos, 8 to 12 weeks old wild-type Swiss female mice were  
587 crossed with Gad1<sup>GFP</sup> Swiss male mice.

588 Isolated mouse SCs from 420 embryos were used in this work and obtained as previously  
589 described [28, 82]. Briefly, pregnant mice were anesthetized by intramuscular injection of a  
590 mix of ketamine and xylazine and sacrificed using a lethal dose of CO<sub>2</sub> after embryos of  
591 either sex were removed. Whole SCs were isolated from eGFP-positive embryos and  
592 maintained in an artificial cerebrospinal fluid (ACSF) containing 135 mM NaCl, 25 mM  
593 NaHCO<sub>3</sub>, 1 mM NaH<sub>2</sub>PO<sub>4</sub>, 3 mM KCl, 11 mM glucose, 2 mM CaCl<sub>2</sub>, and 1 mM MgCl<sub>2</sub> (307  
594 mOsm/kg H<sub>2</sub>O), continuously bubbled with a 95% O<sub>2</sub>-5% CO<sub>2</sub> gas mixture.

595 In the lumbar SC of Gad1<sup>GFP</sup> mouse embryos, eGFP neurons were detected using 488 nm  
596 UV light. They were localized in the ventro-lateral marginal zone between the motor  
597 columns and the ventral funiculi [66]. Embryonic V1<sup>R</sup> identity was confirmed by the  
598 expression of the forkhead transcription factor Foxd3 [25].

599

#### 600 **Whole-cell recordings and analysis**

601 The isolated SC was placed in a recording chamber and was continuously perfused (2  
602 ml/min) at room temperature (22-26°C) with oxygenated ACSF. Whole-cell patch-clamp  
603 recordings of lumbar spinal embryonic V1<sup>R</sup> were carried out under direct visualization using  
604 an infrared-sensitive CCD video camera. Whole-cell patch-clamp electrodes with a  
605 resistance of 4-7 MΩ were pulled from thick-wall borosilicate glass using a P-97 horizontal  
606 puller (Sutter Instrument Co., USA). They were filled with a solution containing (in mM):  
607 96.4 K methanesulfonate, 33.6 KCl, 4 MgCl<sub>2</sub>, 4 Na<sub>2</sub>ATP, 0.3 Na<sub>3</sub>GTP, 10 EGTA, and 10 HEPES  
608 (pH 7.2; 290 mOsm/kg-H<sub>2</sub>O). This intracellular solution led to an equilibrium potential of  
609 chloride ions,  $E_{Cl}$ , of about -30 mV, close to the physiological values measured at E12.5 in  
610 spinal MNs [28]. The junction potential (6.6 mV) was systematically corrected offline.

611 Signals were recorded using Multiclamp 700B amplifiers (Molecular Devices, USA). Data  
612 were low-pass filtered (2 kHz), digitized (20 kHz) online using Digidata 1440A or 1550B  
613 interfaces and acquired using pCLAMP 10.5 software (Molecular Devices, USA). Analyses  
614 were performed off-line using pCLAMP 10.5 software packages (Molecular devices;  
615 RRID:SCR\_014284) and Axograph 1.7.2 (AxoGraph; RRID:SCR\_002798).

616 In voltage-clamp mode, voltage-dependent K<sup>+</sup> currents ( $I_{Kv}$ ) were elicited in the presence  
617 of 1 μM tetrodotoxin (TTX, Alomone lab, Cat# T550, CAS No.: 18660-81-6) by 500 ms  
618 depolarizing voltage steps (10 mV increments, 10 s interval) after a prepulse of 300 ms at

619  $V_H = -100$  mV. To isolate  $I_{Kdr}$ , voltage steps were applied after a 300 ms prepulse at  $V_H = -$   
620 30 mV that inactivated the low threshold transient potassium current  $I_A$ .  $I_A$  was then  
621 obtained by subtracting offline  $I_{Kdr}$  from the total potassium current  $I_{Kv}$ . Capacitance and  
622 leak current were subtracted using on-line P/4 protocol provided by pCLAMP 10.5.  
623 In current-clamp mode,  $V1^R$  discharge was elicited using 2 s depolarizing current steps  
624 (from 0 to  $\approx 50$  pA in 5-10 pA increments, depending on the input resistance of the cell)  
625 with an 8 s interval to ensure that the membrane potential returned to  $V_H$ . When a cell  
626 generated a sustained discharge, the intensity of the depolarizing pulse was reduced to the  
627 minimal value compatible with repetitive firing.

628  $I_{Nap}$  was measured in voltage-clamp mode using a 70 mV/s depolarizing voltage ramp [83].  
629 This speed was slow enough to preclude substantial contamination by the inactivating  
630 transient current and fast enough to avoid substantial inactivation of  $I_{Nap}$ . Subtraction of  
631 the current evoked by the voltage ramp in the presence of 1  $\mu$ M TTX from the control  
632 voltage ramp-evoked current revealed  $I_{Nap}$ .

633

#### 634 **Pharmacological reagents**

635 During patch-clamp recordings, bath application of TTX (1  $\mu$ M, Alomone lab, Cat# T550,  
636 CAS No.: 18660-81-6) or 4-aminopyridine (4-AP, Sigma Aldrich Cat# T550, CAS No.: 18660-  
637 81-6) was done using 0.5 mm diameter quartz tubing positioned, under direct visual  
638 control, 50  $\mu$ m away from the recording area. The quartz tubing was connected to 6  
639 solenoid valves linked with 6 reservoirs *via* a manifold. Solutions were gravity-fed into the  
640 quartz tubing. Their application was controlled using a VC-8 valve controller (Warner  
641 Instruments, USA).

642 4-AP was used to block  $I_{Kdr}$ . To determine the concentration–response curve,  $I - V$  curves  
643 of  $I_{Kdr}$  for different concentrations of 4-AP (0.3 to 300  $\mu$ M) were compared to the control  
644 curve obtained in the absence of 4-AP. The percentage of inhibition for a given  
645 concentration was calculated by dividing the peak intensity of  $I_{Kdr}$  by the peak value  
646 obtained in control condition. The obtained normalized concentration–response curves  
647 were fitted using the Hill equation:

$$648 \frac{100 - I_{min}}{1 + ([4-AP]/IC_{50})^{n_H}} + I_{min} ,$$

649 where [4-AP] is the 4-AP concentration,  $I_{min}$  is the residual current (in percentage of the  
650 peak  $I_{Kdr}$ ),  $100 - I_{min}$  is the maximal inhibition achieved for saturating concentration of  
651 4-AP,  $IC_{50}$  is the 4-AP concentration producing half of the maximal inhibition, and  $n_H$  is  
652 the Hill coefficient. Curve fitting was performed using KaleidaGraph 4.5 (Synergy Software,  
653 USA).

654

### 655 **Immunohistochemistry and confocal microscopy**

656 E14.5 embryos were collected from pregnant females. Once dissected out of their yolk sac,  
657 SCs were dissected and immediately immersion-fixed in phosphate buffer (PB 0.1 M)  
658 containing 4% paraformaldehyde (PFA; freshly prepared in PB, pH 7.4) for 1 h at 4°C. Whole  
659 SCs were then rinsed out in 0.12 M PB at 4°C, thawed at room temperature, washed in PBS,  
660 incubated in  $NH_4Cl$  (50 mM), diluted in PBS for 20 min and then permeabilized for 30 min in  
661 a blocking solution (10% goat serum in PBS) with 0.2% Triton X-100. They were incubated  
662 for 48 h at 4°C in the presence of the following primary antibodies: guinea pig anti-FoxD3  
663 (1:5000, gift from Carmen Birchmeier and Thomas Müller of the Max Delbrück Center for  
664 Molecular Medicine in Berlin) and rabbit anti-cleaved Caspase-3 (1:1000, Cell Signaling  
665 Technology Cat# 9661, RRID:AB\_2341188). SCs were then washed in PBS and incubated for

666 2 h at RT with secondary fluorescent antibodies (goat anti-rabbit-conjugated 649; donkey  
667 anti-guinea pig-conjugated Alexa Fluor 405 [1:1000, ThermoFisher]) diluted in 0.2% Triton  
668 X-100 blocking solution. After washing in PBS, SCs were dried and mounted in Mowiol  
669 medium (Millipore, Molsheim, France). Preparations were then imaged using a Leica SP5  
670 confocal microscope. Immunostaining was observed using a 40X oil-immersion objective  
671 with a numerical aperture of 1.25, as well as with a 63X oil-immersion objective with a  
672 numerical aperture of 1.32. Serial optical sections were obtained with a Z-step of 1  $\mu$ m  
673 (40X) and 0.2-0.3  $\mu$ m (63X). Images (1024x1024; 12-bit color scale) were stored using Leica  
674 software LAS-AF and analyzed using ImageJ 1.5 (N.I.H., USA, RRID:SCR\_003070) and Adobe  
675 Photoshop CS6 (Adobe, USA, RRID:SCR\_014199) software.

676

### 677 **Cluster analysis**

678 To classify the firing patterns of embryonic V1<sup>R</sup>, we performed a hierarchical cluster  
679 analysis on a population of 163 cells. Each cell was characterized by three quantitative  
680 measures of its firing pattern (see legend of Figure 5). After normalizing these quantities to  
681 zero mean and unit variance, we performed a hierarchical cluster analysis using the hclust  
682 function in R 3.3.2 software (Cran project ; <https://cran.r-project.org/>; RRID:SCR\_001905)  
683 that implements the complete linkage method. The intercluster distance was defined as  
684 the maximum Euclidean distance between the points of two clusters, and, at each step of  
685 the process, the two closest clusters were merged into a single one, thus constructing  
686 progressively a dendrogram. Clusters were then displayed in data space using the  
687 dendromat function in the R package 'squash' dedicated to color-based visualization of  
688 multivariate data. The best clustering was determined using the silhouette measure of  
689 clustering consistency [84]. The silhouette of a data point, based on the comparison of its

690 distance to other points in the same cluster and to points in the closest cluster, ranges  
691 from -1 to 1. A value near 1 indicates that the point is well assigned to its cluster, a value  
692 near 0 indicates that it is close to the decision boundary between two neighboring clusters,  
693 and negative values may indicate incorrect assignment to the cluster. This allowed us to  
694 identify an optimal number k of clusters by maximizing the overall average silhouette over  
695 a range of possible values for k [84], using the silhouette function in the R package ‘cluster’.

696

### 697 **Biophysical modeling**

698 To understand the relationship between the voltage-dependent membrane conductances  
699 and the firing patterns of embryonic V1<sup>R</sup>, we relied on a single compartment conductance-  
700 based model that included the leak current, the transient and persistent components of  
701 the sodium current,  $I_{Nat}$  and  $I_{Nap}$ , a delayed rectifier potassium current  $I_{Kdr}$  and the  
702 inactivating potassium current  $I_A$  revealed by experiments. Voltage evolution then  
703 followed the equation

$$704 \quad C_{in} \frac{dV}{dt} = G_{in}(V_r - V) + G_{Nat}m^3h(E_{Na} - V) + G_{Nap}m_p^3s(V_{Na} - V) + G_{Kdr}n^3(E_K - V) +$$

$$705 \quad G_A m_A h_A (E_K - V) + I \quad (1),$$

706 ,

707 where  $C_{in}$  was the input capacitance;  $G_{in}$  the input conductance;  $G_{Nat}$ ,  $G_{Nap}$ ,  $G_{Kdr}$  and  
708  $G_A$  the maximal conductances of the aforementioned currents;  $m$ ,  $m_p$ ,  $n$  and  $m_A$  their  
709 activation variables;  $h$  the inactivation variable of  $I_{Nat}$ ,  $s$  the slow inactivation variable of  
710  $I_{Nap}$ , and  $m_A$  the inactivation variable of  $I_A$ .  $V_r$  is the baseline potential imposed by *ad hoc*  
711 current injection in current-clamp experiments;  $E_{Na}$  and  $E_K$  are the Nernst potentials of  
712 sodium and potassium ions, and  $I$  the injected current. All gating variables satisfied  
713 equations of the form:

714  $\tau_x \frac{dx}{dt} = x_\infty(V) - x,$

715 where the (in)activation curves were modeled by a sigmoid function of the form:

716  $x_\infty = \frac{1}{1 + \exp(-(V - V_x)/k_x)}$

717 with  $k_x$  being positive for activation and negative for inactivation. The time constant  $\tau_x$   
718 was voltage-independent except for the inactivation variables  $h$  and  $s$ . The activation  
719 variable  $m_A$  of  $I_A$  was assumed to follow instantaneously voltage changes.

720 The effect of channel noise was investigated with a stochastic realization of the model,  
721 where channels kinetics were described by Markov-type models, assuming a unitary  
722 channel conductance of 10 pS for all channels.

723

#### 724 **Choice of model parameters**

725 Most model parameters were chosen on the basis of experimental measurements  
726 performed in the present study or already reported [25]. Parameters that could not be  
727 constrained from our experimental data were chosen from an experimentally realistic  
728 range of values.  $V_r$  was set at -60 mV as in experiments (see **table 1**).  $C_{in}$  (average 13.15  
729 pF, 50% between 11.9 and 15.1 pF, only 18 cells out of 246 in the first quartile below 7.2 pF  
730 or in the fourth quartile above 19 pF) and  $G_{in}$  (50% of cells between 0.71 and 1.18 nS, only  
731 7 out of 242 with input conductance above 2 nS) were not spread much in the cells  
732 recorded at E12.5, which showed that most embryonic V1<sup>R</sup> were of comparable size.  
733 Interestingly,  $C_{in}$  and  $G_{in}$  were not correlated, which indicated that the input conductance  
734 was determined by the density of leak channels rather than by the sheer size of the cell.  
735 Moreover, no correlation was observed between the passive properties and the firing  
736 pattern [25]. Therefore, we always set  $G_{in}$  and  $C_{in}$  to 1 nS and 13 pF in the model (except

737 in **Figure 6—figure supplement 2**), close to the experimental medians (0.96 nS and 13.15  
 738 pF, respectively). The membrane time constant  $C_{in}/G_{in}$  was then equal to 13 ms, which  
 739 was also close to the experimental median (13.9 ms, N=241).  
 740  $E_{Na}$  was set to 60 mV (see [25]). The activation curve of  $I_{Nap}$  was obtained by fitting  
 741 experimental data, leading to an average mid-activation of -36 mV and an average  
 742 steepness of 9.5 mV. The experimentally measured values of  $G_{Nap}$  were in the range 0-2.2  
 743 nS. We assumed that the activation curve of  $I_{Nat}$  was shifted rightward by 10 mV in  
 744 comparison to  $I_{Nap}$ . No experimental data was available for the inactivation of  $I_{Nat}$ . We  
 745 chose a mid-inactivation voltage  $V_h = -45$  mV and a steepness  $k_h = -5$  mV. We also assumed  
 746 that the activation time constant of both  $I_{Nat}$  and  $I_{Nap}$  was 1.5 ms, and that the  
 747 inactivation time constant was voltage-dependent:  
 748  $\tau_h(V) = 16.5 - 13.5 \tanh((V + 20)/15)$ , decreasing by one order of magnitude (from 30  
 749 ms down to 3 ms) with the voltage increase. This enabled us to account for the shape of  
 750 the action potentials recorded in experiments, showing a slow rise time and rather long  
 751 duration. The conductance  $G_{Nat}$  was not measured experimentally. When choosing a  
 752 reasonable value of 20 nS for  $G_{Nat}$ , the model behaved very much as recorded embryonic  
 753  $V1^R$ : with similar current threshold (typically 10-20 pA) and stable plateau potential  
 754 obtained for the largest values of  $G_{Nap}$ .  
 755 When taking into account slow inactivation of  $I_{Nap}$  (see **Figure 8**), we chose  $V_s = -30$  mV  
 756 for the mid-inactivation voltage and set the steepness  $k_s$  at -5 mV (as for the inactivation  
 757 of  $I_{Nat}$ ). For simplicity, we assumed that the inactivation time constant was voltage-  
 758 independent and set it at a value of 2 s.  
 759  $E_K$  was set to the experimentally measured value of -96 mV [25]. The activation  
 760 parameters of  $I_{Kdr}$  were obtained by fitting the experimental data:  $V_n = -20$  mV,  $k_n = 15$

761 mV,  $\tau_n = 10$  ms and an activation exponent of 3. The activation and inactivation properties  
762 of  $I_A$  were also chosen based on experimental measurements. Accordingly,  $V_{m_A} = -30$  mV,  
763  $k_{m_A} = -12$  mV,  $V_{h_A} = -70$  mV,  $k_{h_A} = -7$  mV, and  $\tau_{h_A} = 23$  ms. When  $I_A$  was taken into  
764 account, we assumed that  $G_A = G_{Kdr}$ , consistently with experimental data (see **Figure 6—**  
765 **figure supplement 1**).

766

### 767 **Numerical simulations and dynamical systems analysis**

768 We integrated numerically the deterministic model using the freeware XPP-Aut 8.0  
769 (University of Pittsburgh; Pennsylvania; USA; RRID:SCR\_001996) [85] and a standard  
770 fourth-order Runge-Kutta algorithm. XPP-Aut was also used to compute one-parameter  
771 and two-parameters bifurcation diagrams. The stochastic version of the model was also  
772 implemented in XPP-Aut and computed with a Gillespie's algorithm [86].

773 To investigate the dynamics of the model with slow inactivation of  $I_{Nap}$ , we relied on  
774 numerical simulations together with fast/slow dynamics analysis [87]. In this approach, one  
775 distinguishes slow dynamical variables (here only  $s$ ) and fast dynamical variables. Slow  
776 variables vary little at the time scale of fast variables and may therefore be considered as  
777 constant parameters of the fast dynamics in first approximation. In contrast, slow variables  
778 are essentially sensitive to the time average of the fast variables, much more than to their  
779 instantaneous values. This separation of time scales allows one to conduct a phase plane  
780 analysis of the full dynamics.

781

### 782 **Statistics**

783 Samples sizes ( $n$ ) were determined based on previous experience. The number of embryos  
784 ( $N$ ) is indicated in the main text and figure captions. No power analysis was employed, but

785 sample sizes are comparable to those typically used in the field. All values were expressed  
786 as mean with standard error of mean (SEM). Statistical significance was assessed by non-  
787 parametric Kruskal-Wallis test with Dunn's post hoc test for multiple comparisons, Mann-  
788 Whitney test for unpaired data or Wilcoxon matched pairs test for paired data using  
789 GraphPad Prism 7.0e Software (USA). Significant changes in the proportions of firing  
790 patterns with age were assessed by chi-square test for large sample and by Fisher's exact  
791 test for small sample using GraphPad Prism 7.0e Software (GraphPad Software, USA;  
792 RRID:SCR\_002798). Significance was determined as  $p < 0.05$  (\*),  $p < 0.01$  (\*\*) or  $p < 0.001$   
793 (\*\*\*). The exact p value was mentioned in the result section or in the figure captions.

794 **Acknowledgments**

795 We thank Susanne Bolte, Jean-François Gilles and France Lam for assistance with confocal  
796 imaging (IBPS imaging facility) and IBPS rodent facility team for animal care and  
797 production. We thank University Paris Descartes for hosting Yulia Timofeeva as an invited  
798 professor. This work was supported by INSERM, CNRS, Sorbonne Université (Paris),  
799 Université de Bordeaux, Université Paris Descartes and Fondation pour la Recherche  
800 Médicale.

801

802 **Additional information**

803 **Competing interests**

804 The authors declare no competing interests

805

807 **References**

- 808 1. O'Donovan MJ. The origin of spontaneous activity in developing networks of the  
809 vertebrate nervous system. *Curr Opin Neurobiol.* 1999;9(1):94-104. PubMed PMID:  
810 10072366.
- 811 2. Saint-Amant L. Development of motor rhythms in zebrafish embryos. *Progress in*  
812 *brain research.* 2010;187:47-61. doi: 10.1016/B978-0-444-53613-6.00004-6. PubMed PMID:  
813 21111200.
- 814 3. Blankenship AG, Feller MB. Mechanisms underlying spontaneous patterned activity  
815 in developing neural circuits. *Nature reviews Neuroscience.* 2010;11(1):18-29. doi:  
816 10.1038/nrn2759. PubMed PMID: 19953103; PubMed Central PMCID: PMC2902252.
- 817 4. Myers CP, Lewcock JW, Hanson MG, Gosgnach S, Aimone JB, Gage FH, et al.  
818 Cholinergic input is required during embryonic development to mediate proper assembly of  
819 spinal locomotor circuits. *Neuron.* 2005;46(1):37-49. Epub 2005/04/12. doi: S0896-  
820 6273(05)00165-0 [pii]  
821 10.1016/j.neuron.2005.02.022. PubMed PMID: 15820692.
- 822 5. Milner LD, Landmesser LT. Cholinergic and GABAergic inputs drive patterned  
823 spontaneous motoneuron activity before target contact. *J Neurosci.* 1999;19(8):3007-22.  
824 PubMed PMID: 10191318.
- 825 6. Hanson MG, Landmesser LT. Characterization of the circuits that generate  
826 spontaneous episodes of activity in the early embryonic mouse spinal cord. *J Neurosci.*  
827 2003;23(2):587-600. PubMed PMID: 12533619.
- 828 7. Momose-Sato Y, Sato K. Large-scale synchronized activity in the embryonic  
829 brainstem and spinal cord. *Frontiers in cellular neuroscience.* 2013;7:36. doi:  
830 10.3389/fncel.2013.00036. PubMed PMID: 23596392; PubMed Central PMCID:  
831 PMC3625830.
- 832 8. Khazipov R, Luhmann HJ. Early patterns of electrical activity in the developing  
833 cerebral cortex of humans and rodents. *Trends in neurosciences.* 2006;29(7):414-8. doi:  
834 10.1016/j.tins.2006.05.007. PubMed PMID: 16713634.
- 835 9. Allain AE, Le Corrionc H, Delpy A, Cazenave W, Meyrand P, Legendre P, et al.  
836 Maturation of the GABAergic transmission in normal and pathologic motoneurons. *Neural*  
837 *plasticity.* 2011;2011:905624. doi: 10.1155/2011/905624. PubMed PMID: 21785735;  
838 PubMed Central PMCID: PMC3140191.

- 839 10. Branchereau P, Chapron J, Meyrand P. Descending 5-hydroxytryptamine raphe  
840 inputs repress the expression of serotonergic neurons and slow the maturation of inhibitory  
841 systems in mouse embryonic spinal cord. *J Neurosci.* 2002;22(7):2598-606. doi: 20026199.  
842 PubMed PMID: 11923425.
- 843 11. Yvert B, Branchereau P, Meyrand P. Multiple spontaneous rhythmic activity patterns  
844 generated by the embryonic mouse spinal cord occur within a specific developmental time  
845 window. *Journal of neurophysiology.* 2004;91(5):2101-9. doi: 10.1152/jn.01095.2003.  
846 PubMed PMID: 14724265.
- 847 12. Czarnecki A, Le Corrionc H, Rigato C, Le Bras B, Couraud F, Scain AL, et al.  
848 Acetylcholine controls GABA-, glutamate-, and glycine-dependent giant depolarizing  
849 potentials that govern spontaneous motoneuron activity at the onset of synaptogenesis in the  
850 mouse embryonic spinal cord. *J Neurosci.* 2014;34(18):6389-404. doi:  
851 10.1523/JNEUROSCI.2664-13.2014. PubMed PMID: 24790209.
- 852 13. Pun S, Sigrist M, Santos AF, Ruegg MA, Sanes JR, Jessell TM, et al. An intrinsic  
853 distinction in neuromuscular junction assembly and maintenance in different skeletal  
854 muscles. *Neuron.* 2002;34(3):357-70. doi: 10.1016/s0896-6273(02)00670-0. PubMed PMID:  
855 11988168.
- 856 14. Angelim M, Maia L, Mouffle C, Ginhoux F, Low D, Amancio-Dos-Santos A, et al.  
857 Embryonic macrophages and microglia ablation alter the development of dorsal root  
858 ganglion sensory neurons in mouse embryos. *Glia.* 2018;66(11):2470-86. doi:  
859 10.1002/glia.23499. PubMed PMID: 30252950.
- 860 15. Marmigere F, Ernfors P. Specification and connectivity of neuronal subtypes in the  
861 sensory lineage. *Nature reviews Neuroscience.* 2007;8(2):114-27. doi: 10.1038/nrn2057.  
862 PubMed PMID: 17237804.
- 863 16. Ozaki S, Snider WD. Initial trajectories of sensory axons toward laminar targets in  
864 the developing mouse spinal cord. *The Journal of comparative neurology.* 1997;380(2):215-  
865 29. PubMed PMID: 9100133.
- 866 17. Ballion B, Branchereau P, Chapron J, Viala D. Ontogeny of descending serotonergic  
867 innervation and evidence for intraspinal 5-HT neurons in the mouse spinal cord. *Brain*  
868 *research Developmental brain research.* 2002;137(1):81-8. doi: 10.1016/s0165-  
869 3806(02)00414-5. PubMed PMID: 12128257.
- 870 18. Moody WJ, Bosma MM. Ion channel development, spontaneous activity, and  
871 activity-dependent development in nerve and muscle cells. *Physiological reviews.*  
872 2005;85(3):883-941. doi: 10.1152/physrev.00017.2004. PubMed PMID: 15987798.

- 873 19. Spitzer NC. Electrical activity in early neuronal development. *Nature*.  
874 2006;444(7120):707-12. doi: 10.1038/nature05300. PubMed PMID: 17151658.
- 875 20. Katz LC, Shatz CJ. Synaptic activity and the construction of cortical circuits. *Science*.  
876 1996;274(5290):1133-8. PubMed PMID: 8895456.
- 877 21. Hanson MG, Milner LD, Landmesser LT. Spontaneous rhythmic activity in early  
878 chick spinal cord influences distinct motor axon pathfinding decisions. *Brain Res Rev*.  
879 2008;57(1):77-85. Epub 2007/10/09. doi: S0165-0173(07)00127-0 [pii]  
880 10.1016/j.brainresrev.2007.06.021. PubMed PMID: 17920131.
- 881 22. Hanson MG, Landmesser LT. Normal patterns of spontaneous activity are required  
882 for correct motor axon guidance and the expression of specific guidance molecules. *Neuron*.  
883 2004;43(5):687-701. doi: 10.1016/j.neuron.2004.08.018. PubMed PMID: 15339650.
- 884 23. Hanson MG, Landmesser LT. Increasing the frequency of spontaneous rhythmic  
885 activity disrupts pool-specific axon fasciculation and pathfinding of embryonic spinal  
886 motoneurons. *J Neurosci*. 2006;26(49):12769-80. doi: 10.1523/JNEUROSCI.4170-06.2006.  
887 PubMed PMID: 17151280.
- 888 24. Benito-Gonzalez A, Alvarez FJ. Renshaw cells and Ia inhibitory interneurons are  
889 generated at different times from p1 progenitors and differentiate shortly after exiting the  
890 cell cycle. *J Neurosci*. 2012;32(4):1156-70. doi: 10.1523/JNEUROSCI.3630-12.2012.  
891 PubMed PMID: 22279202; PubMed Central PMCID: PMC3276112.
- 892 25. Boeri J, Le Corrone H, Lejeune FX, Le Bras B, Mouffle C, Angelim M, et al.  
893 Persistent Sodium Current Drives Excitability of Immature Renshaw Cells in Early  
894 Embryonic Spinal Networks. *J Neurosci*. 2018;38(35):7667-82. doi:  
895 10.1523/JNEUROSCI.3203-17.2018. PubMed PMID: 30012693.
- 896 26. Perry S, Gezelius H, Larhammar M, Hilscher MM, Lamotte d'Incamps B, Leao KE,  
897 et al. Firing properties of Renshaw cells defined by *Chrna2* are modulated by  
898 hyperpolarizing and small conductance ion currents *I<sub>h</sub>* and *ISK*. *The European journal of*  
899 *neuroscience*. 2015;41(7):889-900. doi: 10.1111/ejn.12852. PubMed PMID: 25712471.
- 900 27. Bikoff JB, Gabitto MI, Rivard AF, Drobac E, Machado TA, Miri A, et al. Spinal  
901 Inhibitory Interneuron Diversity Delineates Variant Motor Microcircuits. *Cell*.  
902 2016;165(1):207-19. doi: 10.1016/j.cell.2016.01.027. PubMed PMID: 26949184; PubMed  
903 Central PMCID: PMC4808435.
- 904 28. Delpy A, Allain AE, Meyrand P, Branchereau P. NKCC1 cotransporter inactivation  
905 underlies embryonic development of chloride-mediated inhibition in mouse spinal

906 motoneuron. *J Physiol.* 2008;586(4):1059-75. doi: 10.1113/jphysiol.2007.146993. PubMed  
907 PMID: 18096599; PubMed Central PMCID: PMC2375629.

908 29. Crill WE. Persistent sodium current in mammalian central neurons. *Annual review of*  
909 *physiology.* 1996;58:349-62. doi: 10.1146/annurev.ph.58.030196.002025. PubMed PMID:  
910 8815799.

911 30. Sillar KT, Simmers AJ, Wedderburn JF. The post-embryonic development of cell  
912 properties and synaptic drive underlying locomotor rhythm generation in *Xenopus* larvae.  
913 *Proceedings Biological sciences.* 1992;249(1324):65-70. doi: 10.1098/rspb.1992.0084.  
914 PubMed PMID: 1359549.

915 31. Gao BX, Ziskind-Conhaim L. Development of ionic currents underlying changes in  
916 action potential waveforms in rat spinal motoneurons. *Journal of neurophysiology.*  
917 1998;80(6):3047-61. PubMed PMID: 9862905.

918 32. Gao H, Lu Y. Early development of intrinsic and synaptic properties of chicken  
919 nucleus laminaris neurons. *Neuroscience.* 2008;153(1):131-43. doi:  
920 10.1016/j.neuroscience.2008.01.059. PubMed PMID: 18355968.

921 33. McKay BE, Turner RW. Physiological and morphological development of the rat  
922 cerebellar Purkinje cell. *J Physiol.* 2005;567(Pt 3):829-50. doi:  
923 10.1113/jphysiol.2005.089383. PubMed PMID: 16002452; PubMed Central PMCID:  
924 PMC1474219.

925 34. Liu X, Pfaff DW, Calderon DP, Tabansky I, Wang X, Wang Y, et al. Development  
926 of Electrophysiological Properties of Nucleus Gigantocellularis Neurons Correlated with  
927 Increased CNS Arousal. *Developmental neuroscience.* 2016;38(4):295-310. doi:  
928 10.1159/000449035. PubMed PMID: 27788521; PubMed Central PMCID: PMC5127753.

929 35. Pineda R, Ribera A. Evolution of the Action Potential. In: Kaas JH, editor. *Evolution*  
930 *of Nervous Systems.* 1: Elsevier Ltd; 2010. p. 211-38.

931 36. Coetzee WA, Amarillo Y, Chiu J, Chow A, Lau D, McCormack T, et al. Molecular  
932 diversity of K<sup>+</sup> channels. *Annals of the New York Academy of Sciences.* 1999;868:233-85.  
933 doi: 10.1111/j.1749-6632.1999.tb11293.x. PubMed PMID: 10414301.

934 37. O'Leary T, Williams AH, Caplan JS, Marder E. Correlations in ion channel  
935 expression emerge from homeostatic tuning rules. *Proceedings of the National Academy of*  
936 *Sciences of the United States of America.* 2013;110(28):E2645-54. Epub 2013/06/27. doi:  
937 10.1073/pnas.1309966110. PubMed PMID: 23798391; PubMed Central PMCID:  
938 PMCPMC3710808.

939 38. Taylor AL, Goillaud JM, Marder E. How multiple conductances determine  
940 electrophysiological properties in a multicompartment model. *J Neurosci.*  
941 2009;29(17):5573-86. Epub 2009/05/01. doi: 10.1523/jneurosci.4438-08.2009. PubMed  
942 PMID: 19403824; PubMed Central PMCID: PMCPMC2821064.

943 39. Alonso LM, Marder E. Visualization of currents in neural models with similar  
944 behavior and different conductance densities. *eLife.* 2019;8. Epub 2019/02/01. doi:  
945 10.7554/eLife.42722. PubMed PMID: 30702427; PubMed Central PMCID:  
946 PMCPMC6395073.

947 40. Sigworth FJ, Sine SM. Data transformations for improved display and fitting of  
948 single-channel dwell time histograms. *Biophysical journal.* 1987;52(6):1047-54. doi:  
949 10.1016/S0006-3495(87)83298-8. PubMed PMID: 2447968; PubMed Central PMCID:  
950 PMC1330104.

951 41. Ramoa AS, McCormick DA. Developmental changes in electrophysiological  
952 properties of LGNd neurons during reorganization of retinogeniculate connections. *J*  
953 *Neurosci.* 1994;14(4):2089-97. PubMed PMID: 8158259; PubMed Central PMCID:  
954 PMC6577110.

955 42. Belleau ML, Warren RA. Postnatal development of electrophysiological properties  
956 of nucleus accumbens neurons. *Journal of neurophysiology.* 2000;84(5):2204-16. doi:  
957 10.1152/jn.2000.84.5.2204. PubMed PMID: 11067966.

958 43. Picken Bahrey HL, Moody WJ. Early development of voltage-gated ion currents and  
959 firing properties in neurons of the mouse cerebral cortex. *Journal of neurophysiology.*  
960 2003;89(4):1761-73. doi: 10.1152/jn.00972.2002. PubMed PMID: 12611962.

961 44. Tong H, McDearmid JR. Pacemaker and plateau potentials shape output of a  
962 developing locomotor network. *Current biology : CB.* 2012;22(24):2285-93. doi:  
963 10.1016/j.cub.2012.10.025. PubMed PMID: 23142042; PubMed Central PMCID:  
964 PMC3525839.

965 45. Alvarez FJ, Benito-Gonzalez A, Siembab VC. Principles of interneuron development  
966 learned from Renshaw cells and the motoneuron recurrent inhibitory circuit. *Annals of the*  
967 *New York Academy of Sciences.* 2013;1279:22-31. doi: 10.1111/nyas.12084. PubMed  
968 PMID: 23530999; PubMed Central PMCID: PMC3870136.

969 46. Allain AE, Segu L, Meyrand P, Branchereau P. Serotonin controls the maturation of  
970 the GABA phenotype in the ventral spinal cord via 5-HT1b receptors. *Annals of the New*  
971 *York Academy of Sciences.* 2010;1198:208-19. doi: 10.1111/j.1749-6632.2010.05433.x.  
972 PubMed PMID: 20536936.

- 973 47. Branchereau P, Morin D, Bonnot A, Ballion B, Chapron J, Viala D. Development of  
974 lumbar rhythmic networks: from embryonic to neonate locomotor-like patterns in the mouse.  
975 *Brain research bulletin*. 2000;53(5):711-8. doi: 10.1016/s0361-9230(00)00403-2. PubMed  
976 PMID: 11165805.
- 977 48. Spitzer NC, Vincent A, Lautermilch NJ. Differentiation of electrical excitability in  
978 motoneurons. *Brain research bulletin*. 2000;53(5):547-52. PubMed PMID: 11165790.
- 979 49. Prasad T, Wang X, Gray PA, Weiner JA. A differential developmental pattern of  
980 spinal interneuron apoptosis during synaptogenesis: insights from genetic analyses of the  
981 protocadherin-gamma gene cluster. *Development*. 2008;135(24):4153-64. doi:  
982 10.1242/dev.026807. PubMed PMID: 19029045; PubMed Central PMCID: PMC2755264.
- 983 50. Taddese A, Bean BP. Subthreshold sodium current from rapidly inactivating sodium  
984 channels drives spontaneous firing of tuberomammillary neurons. *Neuron*. 2002;33(4):587-  
985 600. doi: 10.1016/s0896-6273(02)00574-3. PubMed PMID: 11856532.
- 986 51. Kuo JJ, Lee RH, Zhang L, Heckman CJ. Essential role of the persistent sodium  
987 current in spike initiation during slowly rising inputs in mouse spinal neurones. *J Physiol*.  
988 2006;574(Pt 3):819-34. doi: 10.1113/jphysiol.2006.107094. PubMed PMID: 16728453;  
989 PubMed Central PMCID: PMC1817738.
- 990 52. Ori H, Marder E, Marom S. Cellular function given parametric variation in the  
991 Hodgkin and Huxley model of excitability. *Proceedings of the National Academy of*  
992 *Sciences of the United States of America*. 2018;115(35):E8211-E8. Epub 2018/08/17. doi:  
993 10.1073/pnas.1808552115. PubMed PMID: 30111538; PubMed Central PMCID:  
994 PMC6126753.
- 995 53. Teka W, Tsaneva-Atanasova K, Bertram R, Tabak J. From plateau to pseudo-plateau  
996 bursting: making the transition. *Bulletin of mathematical biology*. 2011;73(6):1292-311. doi:  
997 10.1007/s11538-010-9559-7. PubMed PMID: 20658200; PubMed Central PMCID:  
998 PMC3152987.
- 999 54. Bertram R, Butte MJ, Kiemel T, Sherman A. Topological and phenomenological  
1000 classification of bursting oscillations. *Bulletin of mathematical biology*. 1995;57(3):413-39.  
1001 doi: 10.1007/BF02460633. PubMed PMID: 7728115.
- 1002 55. Izhikevich EM. Neural excitability, spiking and bursting. *Int J Bifurcation Chaos*.  
1003 2000;10(06):1171-266.
- 1004 56. Borisyuk A, Rinzel J. Understanding neuronal dynamics by geometrical dissection of  
1005 minimal models. In: Chow C, Gutkin B, Hansel D, Meunier C, Dalibard J, editors. *Models*

1006 and Methods in Neurophysics. Proc Les Houches Summer School 2003, (Session LXXX):  
1007 Elsevier; 2005. p. 19-72.

1008 57. Rinzel J. Bursting oscillations in an excitable membrane model. In: Sleeman B,  
1009 Jarvis R, editors. Ordinary and Partial Differential Equations Lecture Notes in Mathematics.  
1010 1151. Berlin, Heidelberg: Springer; 1985. p. 304–16.

1011 58. Stern JV, Osinga HM, LeBeau A, Sherman A. Resetting behavior in a model of  
1012 bursting in secretory pituitary cells: distinguishing plateaus from pseudo-plateaus. Bulletin  
1013 of mathematical biology. 2008;70(1):68-88. doi: 10.1007/s11538-007-9241-x. PubMed  
1014 PMID: 17703340.

1015 59. Osinga HM, Tsaneva-Atanasova KT. Dynamics of plateau bursting depending on the  
1016 location of its equilibrium. Journal of neuroendocrinology. 2010;22(12):1301-14. doi:  
1017 10.1111/j.1365-2826.2010.02083.x. PubMed PMID: 20955345.

1018 60. Osinga HM, Sherman A, Tsaneva-Atanasova K. Cross-Currents between Biology  
1019 and Mathematics: The Codimension of Pseudo-Plateau Bursting. Discrete and continuous  
1020 dynamical systems Series A. 2012;32(8):2853-77. doi: 10.3934/dcds.2012.32.2853. PubMed  
1021 PMID: 22984340; PubMed Central PMCID: PMC3439852.

1022 61. Golomb D, Yue C, Yaari Y. Contribution of persistent Na<sup>+</sup> current and M-type K<sup>+</sup>  
1023 current to somatic bursting in CA1 pyramidal cells: combined experimental and modeling  
1024 study. Journal of neurophysiology. 2006;96(4):1912-26. Epub 2006/06/30. doi:  
1025 10.1152/jn.00205.2006. PubMed PMID: 16807352.

1026 62. Del Negro CA, Koshiya N, Butera RJ, Jr., Smith JC. Persistent sodium current,  
1027 membrane properties and bursting behavior of pre-bötzing complex inspiratory neurons in  
1028 vitro. Journal of neurophysiology. 2002;88(5):2242-50. Epub 2002/11/09. doi:  
1029 10.1152/jn.00081.2002. PubMed PMID: 12424266.

1030 63. Rybak IA, Shevtsova NA, Ptak K, McCrimmon DR. Intrinsic bursting activity in the  
1031 pre-Bötzing complex: role of persistent sodium and potassium currents. Biological  
1032 cybernetics. 2004;90(1):59-74. Epub 2004/02/06. doi: 10.1007/s00422-003-0447-1. PubMed  
1033 PMID: 14762725.

1034 64. Izhikevich EM. Subcritical Elliptic Bursting of Bautin Type. SIAM Journal on  
1035 Applied Mathematics. 2000;60(2):503-35. doi:  
1036 <https://doi.org/10.1137/S003613999833263X>.

1037 65. Su J, Rubin J, Terman D. Effects of noise on elliptic bursters. Nonlinearity.  
1038 2004;17(1):133-57. doi: <https://doi.org/10.1088/0951-7715/17/1/009>.

- 1039 66. Stam FJ, Hendricks TJ, Zhang J, Geiman EJ, Francius C, Labosky PA, et al.  
1040 Renshaw cell interneuron specialization is controlled by a temporally restricted transcription  
1041 factor program. *Development*. 2012;139(1):179-90. doi: 10.1242/dev.071134. PubMed  
1042 PMID: 22115757; PubMed Central PMCID: PMC3231776.
- 1043 67. Eccles JC, Fatt P, Landgren S. The inhibitory pathway to motoneurons. *Progress in*  
1044 *neurobiology*. 1956;(2):72-82. PubMed PMID: 13441782.
- 1045 68. Vinay L, Brocard F, Clarac F. Differential maturation of motoneurons innervating  
1046 ankle flexor and extensor muscles in the neonatal rat. *The European journal of neuroscience*.  
1047 2000;12(12):4562-6. doi: 10.1046/j.0953-816x.2000.01321.x. PubMed PMID: 11122369.
- 1048 69. Durand J, Filipchuk A, Pambo-Pambo A, Amendola J, Borisovna Kulagina I,  
1049 Gueritaud JP. Developing electrical properties of postnatal mouse lumbar motoneurons.  
1050 *Frontiers in cellular neuroscience*. 2015;9:349. doi: 10.3389/fncel.2015.00349. PubMed  
1051 PMID: 26388736; PubMed Central PMCID: PMC4557103.
- 1052 70. Marcotti W, Johnson SL, Holley MC, Kros CJ. Developmental changes in the  
1053 expression of potassium currents of embryonic, neonatal and mature mouse inner hair cells.  
1054 *J Physiol*. 2003;548(Pt 2):383-400. doi: 10.1113/jphysiol.2002.034801. PubMed PMID:  
1055 12588897; PubMed Central PMCID: PMC2342842.
- 1056 71. Marcotti W, Johnson SL, Rusch A, Kros CJ. Sodium and calcium currents shape  
1057 action potentials in immature mouse inner hair cells. *J Physiol*. 2003;552(Pt 3):743-61. doi:  
1058 10.1113/jphysiol.2003.043612. PubMed PMID: 12937295; PubMed Central PMCID:  
1059 PMC2343463.
- 1060 72. Sontheimer H, Trotter J, Schachner M, Kettenmann H. Channel expression correlates  
1061 with differentiation stage during the development of oligodendrocytes from their precursor  
1062 cells in culture. *Neuron*. 1989;2(2):1135-45. doi: 10.1016/0896-6273(89)90180-3. PubMed  
1063 PMID: 2560386.
- 1064 73. Allain AE, Bairi A, Meyrand P, Branchereau P. Ontogenic changes of the  
1065 GABAergic system in the embryonic mouse spinal cord. *Brain research*. 2004;1000(1-  
1066 2):134-47. doi: 10.1016/j.brainres.2003.11.071. PubMed PMID: 15053961.
- 1067 74. Sapir T, Geiman EJ, Wang Z, Velasquez T, Mitsui S, Yoshihara Y, et al. Pax6 and  
1068 engrailed 1 regulate two distinct aspects of rensaw cell development. *J Neurosci*.  
1069 2004;24(5):1255-64. doi: 10.1523/JNEUROSCI.3187-03.2004. PubMed PMID: 14762144;  
1070 PubMed Central PMCID: PMC2997484.

1071 75. Henley J, Poo MM. Guiding neuronal growth cones using Ca<sup>2+</sup> signals. Trends in  
1072 cell biology. 2004;14(6):320-30. doi: 10.1016/j.tcb.2004.04.006. PubMed PMID: 15183189;  
1073 PubMed Central PMCID: PMC3115711.

1074 76. Tsaneva-Atanasova K, Osinga HM, Riess T, Sherman A. Full system bifurcation  
1075 analysis of endocrine bursting models. Journal of theoretical biology. 2010;264(4):1133-46.  
1076 doi: 10.1016/j.jtbi.2010.03.030. PubMed PMID: 20307553; PubMed Central PMCID:  
1077 PMC3128456.

1078 77. Tagliavini A, Tabak J, Bertram R, Pedersen MG. Is bursting more effective than  
1079 spiking in evoking pituitary hormone secretion? A spatiotemporal simulation study of  
1080 calcium and granule dynamics. American journal of physiology Endocrinology and  
1081 metabolism. 2016;310(7):E515-25. doi: 10.1152/ajpendo.00500.2015. PubMed PMID:  
1082 26786781.

1083 78. Oster A, Faure P, Gutkin BS. Mechanisms for multiple activity modes of VTA  
1084 dopamine neurons. Frontiers in computational neuroscience. 2015;9:95. doi:  
1085 10.3389/fncom.2015.00095. PubMed PMID: 26283955; PubMed Central PMCID:  
1086 PMC4516885.

1087 79. Chevalier M, Toporikova N, Simmers J, Thoby-Brisson M. Development of  
1088 pacemaker properties and rhythmogenic mechanisms in the mouse embryonic respiratory  
1089 network. eLife. 2016;5. doi: 10.7554/eLife.16125. PubMed PMID: 27434668; PubMed  
1090 Central PMCID: PMC4990420.

1091 80. Kole MH, Stuart GJ. Signal processing in the axon initial segment. Neuron.  
1092 2012;73(2):235-47. doi: 10.1016/j.neuron.2012.01.007. PubMed PMID: 22284179.

1093 81. Tamamaki N, Yanagawa Y, Tomioka R, Miyazaki J, Obata K, Kaneko T. Green  
1094 fluorescent protein expression and colocalization with calretinin, parvalbumin, and  
1095 somatostatin in the GAD67-GFP knock-in mouse. The Journal of comparative neurology.  
1096 2003;467(1):60-79. doi: 10.1002/cne.10905. PubMed PMID: 14574680.

1097 82. Scain AL, Le Corrionc H, Allain AE, Muller E, Rigo JM, Meyrand P, et al. Glycine  
1098 release from radial cells modulates the spontaneous activity and its propagation during early  
1099 spinal cord development. J Neurosci. 2010;30(1):390-403. Epub 2010/01/08. doi: 30/1/390  
1100 [pii]  
1101 10.1523/JNEUROSCI.2115-09.2010. PubMed PMID: 20053920.

1102 83. Huang H, Trussell LO. Control of presynaptic function by a persistent Na(+) current.  
1103 Neuron. 2008;60(6):975-9. doi: 10.1016/j.neuron.2008.10.052. PubMed PMID: 19109905;  
1104 PubMed Central PMCID: PMC2657474.

- 1105 84. Rousseeuw PJ. Silhouettes - a Graphical Aid to the Interpretation and Validation of  
1106 Cluster-Analysis. J Comput Appl Math. 1987;20:53-65. doi: Doi 10.1016/0377-  
1107 0427(87)90125-7. PubMed PMID: WOS:A1987L111800005.
- 1108 85. Ermentrout B. Simulating, Analyzing, and Animating Dynamical Systems: A Guide  
1109 to XPPAUT for Researchers and Students. Philadelphia: Society for Industrial and Applied  
1110 Mathematics; 2002.
- 1111 86. Gillespie DT. A general method for numerically simulating the stochastic time  
1112 evolution of coupled chemical reactions. Journal of Computational Physics. 1976;22(4):403-  
1113 34. doi: [https://doi.org/10.1016/0021-9991\(76\)90041-3](https://doi.org/10.1016/0021-9991(76)90041-3).
- 1114 87. Witelski T, Bowen M. Fast/slow Dynamical Systems. In: Methods of Mathematical  
1115 Modelling: Springer, Cham; 2015.
- 1116
- 1117
- 1118

## 1119 **Figure captions**

### 1120 **Figure 1. $G_{Kdr}$ and $G_{Nap}$ in embryonic $V1^R$ at E12.5 and E14.5**

1121 (A) Representative traces of voltage responses showing single-spiking activity in E12.5 SS  
1122  $V1^R$  (A1), repetitive action potential firing in RS  $V1^R$  (A2), Mixed of plateau potential activity  
1123 and repetitive action potential firing in ME  $V1^R$  (A3) and plateau potential activity in PP  $V1^R$   
1124 (A4). (B) Representative examples of the total outward  $K^+$  currents ( $I_{Kv}$  total) obtained  
1125 from  $V_H = -100$  mV (left traces), of  $I_{Kdr}$  ( $V_H = -30$  mV, middle traces) and of isolated  $I_A$  (left  
1126 traces) recorded at E12.5 in SS  $V1^R$  (B1), RS  $V1^R$  (B2), ME  $V1^R$  (B3) and PP  $V1^R$  (B4). Voltage-  
1127 dependent potassium currents were evoked in response to 10 mV membrane potential  
1128 steps (200 ms) from -100 or from -30 mV to +40 mV (10 s interval between pulses).  $V1^R$   
1129 were voltage clamped at  $V_H = -60$  mV. A prepulse of -40 mV (300 ms) was applied to  
1130 activate both  $I_A$  and  $I_{Kdr}$ .  $I_{Kdr}$  was isolated by applying a prepulse of 30 mV (300 ms) to  
1131 inactivate  $I_A$  (B1 insert).  $I_A$  was isolated by subtracting step-by-step the currents obtained  
1132 using a pre-pulse of 30 mV ( $V_H = -30$  mV) from the currents obtained using a pre-pulse of -  
1133 40 mV ( $V_H = -100$  mV). (C) Current-voltage relationship ( $I - V$  curves) of  $I_{Kdr}$  (filled circles)  
1134 and of  $I_A$  (open circles) recorded in SS  $V1^R$  (C1), RS  $V1^R$  (C2), ME  $V1^R$  (C3) and PP  $V1^R$  (C4).  
1135  $I - V$  curves were obtained from currents shown in B1, B2, B3 and B4. Note that  $I -$   
1136  $V$  curves are similar between SS  $V1^R$ , RS  $V1^R$ , ME  $V1^R$  and PP  $V1^R$ . (D) Bar graph showing  
1137 maximal  $G_{Kdr}$  value (Max  $G_{Kdr}$ ) in SS  $V1^R$  at E12.5 ( $n = 9$ ;  $N = 9$ ; gray bar) and at E14.5 ( $n =$   
1138  $10$ ;  $N = 10$  gray bar), and in RS  $V1^R$  ( $n = 7$ ;  $N = 7$ ; red bar), ME  $V1^R$  ( $n = 3$ ;  $N = 3$  purple bar)  
1139 and PP  $V1^R$  at E12.5 ( $n = 7$ ;  $N = 7$  blue bar).  $G_{Kdr}$  was calculated from  $I_{Kdr}$  at  $V_H = +20$  mV,  
1140 assuming a  $K^+$  equilibrium potential of -96 mV. There is no significant difference  
1141 in  $G_{Kdr}$  between SS  $V1^R$  and RS  $V1^R$ , while  $G_{Kdr}$  is significantly smaller in PP  $V1^R$  as  
1142 compared to SS  $V1^R$  and RS  $V1^R$ .  $G_{Kdr}$  was significantly higher in SS  $V1^R$  at E14.5 than in SS

1143  $V1^R$ , RS  $V1^R$  and PP  $V1^R$  at E12.5. (Kruskall-Wallis test  $P < 0.0001$ ; SS  $V1^R$  versus RS  $V1^R$  at  
 1144 E12.5,  $P = 0.5864$ ; SS  $V1^R$  versus PP  $V1^R$  at E12.5,  $P = 0.0243$ ; RS  $V1^R$  versus PP  $V1^R$  at E12.5,  
 1145  $P = 0.0086$ ; E14.5 SS  $V1^R$  versus E12.5 SS  $V1^R$ ,  $P = 0.0048$ ; E14.5 SS  $V1^R$  versus E12.5 RS  $V1^R$ ,  
 1146  $P = 0.0384$ , E14.5 SS  $V1^R$  versus E12.5 PP  $V1^R$ ,  $P < 0.0001$ ). The increase in  $G_{Kdr}$  between  
 1147 E12.5 and E14.5 is likely to be due to the increase in neuronal size (input capacitance;  
 1148 Figure 2A). Indeed, there was no significant difference (Mann Whitney test,  $P = 0.133$ )  
 1149 in  $G_{Kdr}$  density between SS  $V1^R$  at E12.5 ( $n = 9$ ;  $N = 9$  gray bar) and at E14.5 ( $n = 10$ ;  $N = 10$   
 1150 gray bar). (E) Bar graph showing the maximal  $G_{Nap}$  value (Max  $G_{Nap}$ ) in SS  $V1^R$  at E12.5 ( $n =$   
 1151  $9$ ;  $N = 9$  gray bar) and E14.5 ( $n = 10$ ;  $N = 10$  gray bar), and in RS  $V1^R$  ( $n = 8$ ;  $N = 8$  red bar),  
 1152 ME  $V1^R$  ( $n = 3$ ;  $N = 3$  purple bar) and PP  $V1^R$  ( $n = 6$ ;  $N = 6$  blue bar) at E12.5. Max  $G_{Nap}$  was  
 1153 calculated from maximal  $I_{Nap}$  value measured on current evoked by assuming a  $Na^+$   
 1154 equilibrium potential of +60 mV. There was no difference in  $G_{Nap}$  between RS  $V1^R$  and PP  
 1155  $V1^R$ . On the contrary,  $G_{Nap}$  measured in SS  $V1^R$  at E12.5 or at E14.5 was significantly  
 1156 smaller as compared to  $G_{Nap}$  measured at E12.5 in RS  $V1^R$  or in PP  $V1^R$ .  $G_{Nap}$  measured at  
 1157 E12.5 and E14.5 in SS  $V1^R$  were not significantly different (Kruskall-Wallis test  $P < 0.0001$ ;  
 1158 E12.5 SS  $V1^R$  versus E12.5 RS  $V1^R$ ,  $P = 0.0034$ ; E12.5 SS  $V1^R$  versus E12.5 PP  $V1^R$ ,  $P = 0.0006$ ;  
 1159 E12.5 RS  $V1^R$  versus E12.5 PP  $V1^R$ ,  $P = 0.5494$ ; E14.5 SS  $V1^R$  versus E12.5 SS  $V1^R$ ,  $P = 0.5896$ ;  
 1160 E14.5 SS  $V1^R$  versus E12.5 RS  $V1^R$ ,  $P = 0.0005$ ; E14.5 SS  $V1^R$  versus E12.5 PP  $V1^R$ ,  $P < 0.0001$ ).  
 1161 (F) Histograms showing the  $G_{Nap} / G_{Kdr}$  ratio in SS  $V1^R$  at E12.5 ( $n = 9$ ; gray bar) and E14.5  
 1162 ( $n = 10$ ; green bar) and in RS  $V1^R$  ( $n = 8$ ; red bar), ME  $V1^R$  ( $n = 3$ ; purple bar) and PP  $V1^R$  ( $n =$   
 1163  $6$ ; blue bar) at E12.5. Note that the  $G_{Nap} / G_{Kdr}$  ratio differs significantly between SS  $V1^R$ ,  
 1164 RS  $V1^R$  and PP  $V1^R$  at E12.5, while it is not different between SS  $V1^R$  recorded at E12.5 and  
 1165 at E14.5 (Kruskall-Wallis test  $P < 0.0001$ ; SS  $V1^R$  versus RS  $V1^R$  at E12.5,  $P = 0.0367$ ; SS  $V1^R$   
 1166 versus PP  $V1^R$  at E12.5,  $P < 0.0001$ ; RS  $V1^R$  versus PP  $V1^R$  at E12.5,  $P = 0.0159$ ; E14.5 SS  $V1^R$

1167 versus E12.5 SS V1<sup>R</sup>,  $P = 0.2319$ ; E14.5 SS V1<sup>R</sup> versus E12.5 RS V1<sup>R</sup>,  $P = 0.0017$ ; E14.5 SS V1<sup>R</sup>  
1168 versus E12.5 PP V1<sup>R</sup>  $P < 0.0001$ ). Data shown in A and B were used to  
1169 calculate  $G_{Nap} / G_{Kdr}$  ratio shown in C. (\* $P < 0.05$ , \*\*  $P < 0.01$ , \*\*\*  $P < 0.001$ ).

1170

1171 **Figure 2. Increasing 4-AP concentration changed the firing pattern of single spiking**  
1172 **embryonic V1<sup>R</sup> recorded at E12.5**

1173 The firing pattern of embryonic V1<sup>R</sup> was evoked by 2 s suprathreshold depolarizing current  
1174 steps. (A) Representative traces showing examples of the effect of increasing concentration  
1175 of 4-AP (from 3 to 300  $\mu\text{M}$ ) on the firing pattern of a SS V1<sup>R</sup> recorded at E12.5. Note that in  
1176 A1, increasing 4-AP concentration converted single spiking (gray trace) to repetitive spiking  
1177 (red trace), repetitive spiking to a mixed event pattern (purple trace) and mixed events to  
1178 plateau potential (blue trace). (A2) Example of SS V1<sup>R</sup> in which increasing 4-AP  
1179 concentration converted single spiking to repetitive spiking only. (A3) Bar plots showing the  
1180 change in the firing pattern of SS V1<sup>R</sup> according to 4-AP concentrations (control  $n = 10$ ;  $N =$   
1181  $10$ , 3  $\mu\text{M}$  4-AP  $n = 8$ ;  $N = 8$ , 10  $\mu\text{M}$  4-AP  $n = 10$ ;  $N = 10$ , 30  $\mu\text{M}$  4-AP  $n = 10$ ;  $N = 10$ , 100  $\mu\text{M}$   
1182 4-AP  $n = 10$ ;  $N = 10$ , 300  $\mu\text{M}$  4-AP  $n = 8$ ;  $N = 8$ ). (B) Representative traces showing the effect  
1183 of 0.5  $\mu\text{M}$  TTX on a plateau potential evoked in a SS V1<sup>R</sup> in the presence of 300  $\mu\text{M}$  4-AP. (C)  
1184 Representative traces showing the effect of 0.5  $\mu\text{M}$  TTX on repetitive AP firing evoked in a  
1185 SS V1<sup>R</sup> in the presence of 300  $\mu\text{M}$  4-AP. In both cases, the application of TTX fully blocked  
1186 the responses evoked in the presence of 4-AP, indicating that they were underlain by the  
1187 activation of voltage-gated Na<sup>+</sup> channels.

1188

1189 **Figure 3. Cluster analysis of V1<sup>R</sup> firing pattern at E12.5**

1190 (A, inserts) Cluster analysis of embryonic  $V1^R$  firing pattern was performed using three  
1191 parameters that describe the firing pattern during a 2 s suprathreshold depolarizing pulses:  
1192 the mean of the half-amplitude event duration (mean  $\frac{1}{2}Ad$ ), the coefficient of variation of  
1193  $\frac{1}{2} Ad$  ( $CV \frac{1}{2}Ad$ ) allowing to quantify the AP variation within a train ( $CV$  was set to 0 when  
1194 the number of spikes evoked by a depolarizing pulse was  $\leq 3$ ) and the duration ratio  $ddr =$   
1195  $\Sigma \frac{1}{2} Ad/Pw$ , obtained by dividing the sum of  $\frac{1}{2} Ad$  by the pulse duration  $Pw$ , that indicates  
1196 the total time spent in the depolarized state. For example,  $ddr = 1$  when a plateau potential  
1197 lasts as long as the depolarizing pulse. Conversely, its value is low when the depolarizing  
1198 pulse evokes a single AP only. (A) Dendrogram for complete linkage hierarchical clustering  
1199 of 164 embryonic  $V1^R$  ( $N = 140$ ) according to the values of  $\log$  mean  $\frac{1}{2}Ad$ , of  $CV \frac{1}{2}Ad$  and of  
1200  $\log ddr$ . The colored matrix below the dendrogram shows the variations of these three  
1201 parameters for all the cells in the clusters (colored trees) extracted from the dendrogram.  
1202 (B) The number of clusters was determined by analyzing the distribution of silhouette  
1203 width values (see Material and Methods). The boxplots show the distribution of silhouette  
1204 width values when the number of clusters  $k$  varies from 2 to 12. The mean silhouette width  
1205 values (red diamond shaped points) attained their maximum when the estimated cluster  
1206 number was 5. (C) 3D plot showing cluster distribution of embryonic  $V1^R$  according to  $\log$   
1207 mean  $\frac{1}{2}Ad$ ,  $CV \frac{1}{2}Ad$  and  $\log ddr$ . Each cluster corresponds to a particular firing pattern as  
1208 illustrated in D.  $V1^R$  that cannot sustain repetitive firing of APs (1 to 3 AP/pulse only, gray,  
1209 Single spiking, SS),  $V1^R$  that can fire tonically (red, Repetitive spiking, RS),  $V1^R$  with a firing  
1210 pattern characterized by a mix of APs and relatively short plateau potentials (dark purple,  
1211 Mixed event short PP, ME short PP),  $V1^R$  with a firing pattern characterized by a mix of APs  
1212 and relatively long plateau potentials (light purple, Mixed event long PP, ME long PP) and  
1213  $V1^R$  with evoked plateau potentials only (blue, Plateau potential, PP). The arrow in C

1214 indicates 3 misclassified  $V1^R$  that could not sustain repetitive firing although they were  
1215 assigned to the cluster of repetitively firing  $V1^R$  (see text).

1216

1217 **Figure 4. Developmental changes of embryonic  $V1^R$  firing patterns from E11.5 to E16.5**

1218 (A1) Graph showing how the input capacitance  $C_{in}$  of  $V1^R$  changes with embryonic age.  $C_{in}$

1219 significantly increased between E12.5 or E13.5 and E14.5 (Kruskall-Wallis test  $P < 0.0001$ ;

1220 E12.5 versus E11.5  $P = 0.258$ , E12.5 versus E13.5  $P = 0.904$ , E12.5 versus E14.5  $P < 0.0001$ ,

1221 E12.5 versus E15.5  $P < 0.0001$ , E12.5 versus E16.5  $P < 0.0001$ , E13.5 versus E14.5  $P < 0.0001$ ,

1222 E13.5 versus E15.5  $P < 0.0001$ , E13.5 versus E16.5  $P < 0.0001$ ; E11.5  $n = 31$ ;  $N = 27$ , E12.5  $n$

1223  $= 267$ ;  $N = 152$ , E13.5  $n = 43$ ;  $N = 40$ , E14.5  $n = 61$ ;  $N = 49$ , E15.5  $n = 16$ ;  $N = 4$ , E16.5  $n = 30$ ;

1224  $N = 9$ ). (A2) Graph showing how the input resistance  $R_{in}$  of  $V1^R$  changes with embryonic

1225 age.  $R_{in}$  significantly decreased between E12.5 or E14.5 and E15.5 (Kruskall-Wallis test  $P <$

1226  $0.0001$ ; E12.5 versus E11.5  $P > 0.999$ , E12.5 versus E13.5  $P = 0.724$ , E12.5 versus E14.5  $P >$

1227  $0.999$ , E12.5 versus E15.5  $P = 0.0004$ , E12.5 versus E16.5  $P = 0.0005$ , E14.5 versus E15.5  $P =$

1228  $0.0019$ , E14.5 versus E16.5  $P < 0.0058$ ; E11.5  $n = 31$ , E12.5  $n = 261$ ;  $N = 146$ , E13.5  $n = 43$ ;  $N$

1229  $= 40$ , E14.5  $n = 60$ ;  $N = 48$ , E15.5  $n = 16$ ;  $N = 4$ , E16.5  $n = 30$ ;  $N = 9$ ). (A3) Graph showing

1230 how the threshold of regenerative events (APs and plateau potentials) of  $V1^R$  changes with

1231 embryonic age. The average threshold became significantly more hyperpolarized after

1232 E12.5 (Kruskall-Wallis test  $P < 0.0001$ ; E12.5 versus E11.5  $P = 0.676$ , E12.5 versus E13.5  $P =$

1233  $0.0039$ , E12.5 versus E14.5  $P < 0.0001$ , E12.5 versus E15.5  $P < 0.0001$ , E12.5 versus E16.5  $P$

1234  $< 0.0001$ , E13.5 versus E14.5  $P > 0.999$ , E13.5 versus E15.5  $P = 0.1398$ , E13.5 versus E16.5  $P$

1235  $= 0.0013$ ; E14.5 versus E15.5  $P > 0.999$ , E14.5 versus E16.5  $P = 0.0634$ , E15.5 versus E16.5  $P >$

1236  $0.999$ ; E11.5  $n = 20$ ;  $N = 16$ , E12.5  $n = 162$ ;  $N = 139$ , E13.5  $n = 31$ ;  $N = 28$ , E14.5  $n = 30$ ;  $N =$

1237  $26$ , E15.5  $n = 16$ ;  $N = 4$ , E16.5  $n = 30$ ;  $N = 9$ ). Yellow and purple bars below the graphs

1238 indicate the two important phases of the functional development of spinal cord networks.  
1239 The first one is characterized by synchronized neuronal activity (SNA) and the second one is  
1240 characterized by the emergence of a locomotor-like activity (see text). Note that changes in  
1241  $C_{in}$  and  $R_{in}$  occurred at the end of the first developmental phase. (\* $P < 0.05$ , \*\*  $P < 0.01$ ,  
1242 \*\*\*  $P < 0.001$ ; control, E12.5). The intrinsic activation properties were analyzed using 2 s  
1243 suprathreshold depolarizing current steps. (B) Representative traces of voltage responses  
1244 showing Single Spiking (SS)  $V1^R$  (gray), Repetitive Spiking (RS)  $V1^R$  (red), ME  $V1^R$  (purple)  
1245 and Plateau Potential (PP)  $V1^R$  (blue) at E11.5 (B1), E13.5 (B2), E14.5 (B3) E15.5 (B4) and  
1246 E16.5 (B5). (C) Bar graph showing how the proportions of the different firing patterns  
1247 change from E11.5 to E16.5 (E11.5 n = 22; N = 18, E12.5 n = 163; N = 140, E13.5 n = 32; N =  
1248 29, E14.5 n = 57; N = 45, E15.5 n = 15; N = 4, E16.5 n = 28; N = 9). Yellow and purple bars  
1249 below the graphs indicate the first and the second phase of functional embryonic spinal  
1250 cord networks. The proportions of the different firing patterns significantly changed  
1251 between E11.5 to E12.5 (Fisher's exact test,  $P = 0.0052$ ) with a significant increase in the  
1252 proportion of RS  $V1^R$  (Fisher's exact test,  $P = 0.0336$ ) and a significant decrease in the  
1253 proportion of ME  $V1^R$  (Fisher's exact test,  $P = 0.01071$ ) at E12.5. Only two firing patterns (SS  
1254 and RS) were observed after E13.5 and most embryonic  $V1^R$  lost their ability to sustain  
1255 tonic firing after E13.5. However, at E16.5 the proportion of RS  $V1^R$  significantly increased  
1256 at the expense of SS  $V1^R$  when compared to E14.5 (Fisher's exact test,  $P = 0.0112$ ),  
1257 indicating that embryonic  $V1^R$  began to recover the ability to sustain tonic firing after E15.5.

1258

### 1259 **Figure 5. Activated caspase-3 is not observed in embryonic $V1^R$ at E14.5**

1260 Representative confocal image of the ventral part of an isolated lumbar spinal cord of  
1261 E14.5 GAD67-eGFP mouse embryo showing immunostainings using antibodies against

1262 eGFP (A), FoxD3 (B) and activated Caspase 3 (aCaspase 3) (C). (D) Superimposition of the  
1263 three stainings shows that embryonic  $V1^R$  (eGFP+ and FoxD3+) were not aCaspase 3  
1264 immunoreactive. (A1, B1, C1 and D1). Enlarged images from A, B and C showing that  
1265 aCaspase 3 staining is localized in areas where eGFP and Foxd3 staining were absent. (A2,  
1266 B2, C2 and D2) Enlarged images from A, B and C showing that aCaspase 3 staining is absent  
1267 in the area where  $V1^R$  (eGFP+ and FoxD3+) are located. aCaspase 3 staining that did not co-  
1268 localize with GAD67eGFP likely indicates MN developmental cell death.

1269

1270 **Figure 6. 600  $\mu$ M 4-AP changed the firing pattern of single spiking embryonic  $V1^R$**   
1271 **recorded at E14.5**

1272 The firing pattern of embryonic  $V1^R$  was evoked by 2 s suprathreshold depolarizing current  
1273 steps. (A) Representative traces showing the effect of 4-AP application (600  $\mu$ M) on the  
1274 firing pattern of single spiking (SS)  $V1^R$  recorded at E14.5. Note that the applications of 600  
1275  $\mu$ M 4-AP evoked either a plateau potential (A1) or repetitive spiking (A2), both fully  
1276 blocked by TTX. (B) Bar plots showing the proportions of the different firing patterns  
1277 observed in the presence of 600  $\mu$ M 4-AP versus control recorded in SS  $V1^R$  at E14.5 (n = 14;  
1278 N = 14). Single Spiking (SS)  $V1^R$  (gray), Repetitive Spiking (RS)  $V1^R$  (red), Mixed Events (ME)  
1279  $V1^R$  (purple), Plateau Potential (PP)  $V1^R$  (blue).

1280

1281 **Figure 7. Embryonic  $V1^R$  firing patterns predicted by computational modeling**

1282 (A) Firing patterns of 27 recorded cells, in which both  $G_{Nap}$  and  $G_{Kdr}$  were measured. Gray:  
1283 SS, red: RS, blue: PP. The three purple points located at the boundary between the RS and  
1284 PP regions correspond to mixed events (ME) where plateau potentials alternate with  
1285 spiking episodes. Note that no cell exhibited low values of both  $G_{Nap}$  and  $G_{Kdr}$  (lower left),

1286 or large values of both conductances (upper right). (B) Bifurcation diagram of the  
 1287 deterministic model when  $G_{Kdr}$  is kept fixed to 2.5 nS or 10 nS while  $G_{Nap}$  is varied  
 1288 between 0 and 2.5 nS.  $G_{in} = 1$  nS and  $I = 20$  pA. For  $G_{Kdr} = 10$  nS (i.e., in the top  
 1289 experimental range), the red curves indicate the maximal and minimal voltages achieved  
 1290 on the stable limit cycle associated with repetitive firing (solid lines) and on the unstable  
 1291 limit cycle (dashed lines). The fixed point of the model is indicated by a gray solid line when  
 1292 it corresponds to the stable quiescent state, a gray dashed line when it is unstable and a  
 1293 solid blue line when it corresponds to a stable plateau potential. The two HB corresponding  
 1294 to the change of stability of the quiescence state (HB<sub>1</sub>,  $G_{Nap} = 0.81$  nS) and of the voltage  
 1295 plateau (HB<sub>2</sub>,  $G_{Nap} = 2.13$  nS) are indicated, as well as the two SN bifurcations of limit cycles  
 1296 associated with the onset (SN<sub>1</sub>,  $G_{Nap} = 0.65$  nS) and offset (SN<sub>2</sub>,  $G_{Nap} = 2.42$  nS) of  
 1297 repetitive spiking as  $G_{Nap}$  is increased. For  $G_{Kdr} = 2.5$  nS, the model does not display  
 1298 repetitive firing; it possesses a unique fixed point, which is always stable (blue-gray curve).  
 1299 The transition from quiescence to plateau is gradual with no intervening bifurcation.  
 1300 Representative voltage traces of the three different activity patterns are shown: single  
 1301 spiking in response to a 2 s current pulse (gray,  $G_{Nap} = 0.2$  nS,  $G_{Kdr} = 10$  nS), repetitive  
 1302 spiking (red,  $G_{Nap} = 1.2$  nS,  $G_{Kdr} = 10$  nS) and plateau potential (blue,  $G_{Nap} = 1.2$  nS,  $G_{Kdr} =$   
 1303 2.5 nS). Note that the plateau never outlasts the current pulse. (C) Bifurcation diagram  
 1304 when  $G_{Nap}$  is kept fixed at 1.2 nS and  $G_{Kdr}$  is varied between 0 and 25 nS ( $I = 20$  pA). Same  
 1305 conventions as in B. Plateau potential is stable until the subcritical Hopf bifurcation HB<sub>2</sub>  
 1306 ( $G_{Kdr} = 6.34$  nS) is reached, repetitive firing can be observed between SN<sub>2</sub> ( $G_{Kdr} = 5.93$  nS)  
 1307 and SN<sub>1</sub> ( $G_{Kdr} = 22.65$  nS). The quiescent state is stable from point HB<sub>1</sub> ( $G_{Kdr} = 17.59$  nS)  
 1308 onward. (D) Two-parameters bifurcation diagram of the model in the  $G_{Nap} - G_{Kdr}$  plane ( $I$   
 1309 = 20 pA). The black merged curves indicate the bifurcations HB<sub>1</sub> and HB<sub>2</sub>. The red curves

1310 indicate the SN bifurcations of limit cycles  $SN_1$  and  $SN_2$ . The shaded area indicates the  
1311 region where repetitive firing can occur. The oblique lines through the points labeled 1, 2  
1312 and 3, the same as in B, correspond to three different values of the ratio  $G_{Nap}/G_{Kdr}$  : 0.02  
1313 (gray), 0.12 (red) and 0.48 (blue). Voltage traces on the right display the response to a 2 s  
1314 current pulse when channel noise is taken into account for the three regimes: quiescence  
1315 (top, gray trace and dot in the diagram), repetitive firing (middle, red) and plateau  
1316 potential (bottom, blue). They correspond to the three deterministic voltage traces shown  
1317 in B. Note that the one-parameter bifurcation diagrams shown in B correspond to  
1318 horizontal lines through points 1 and 2 ( $G_{Kdr} = 10$  nS) and through point 3 ( $G_{Kdr} = 2.5$  nS),  
1319 respectively. The bifurcation diagram in C corresponds to a vertical line through point 2 and  
1320 3 ( $G_{Nap} = 1.2$  nS). (E) Cumulative distribution function of the ratio  $G_{Nap}/G_{Kdr}$  for the four  
1321 clusters in A, showing the sequencing SS (gray)  $\rightarrow$  RS (red)  $\rightarrow$  ME (purple, 3 cells only)  $\rightarrow$   
1322 PP (blue) predicted by the two-parameters bifurcation diagram in D. The wide PP range, as  
1323 compared to SS and RS, merely comes from the fact that  $G_{Kdr}$  is small for cells in this  
1324 cluster. The three colored points indicate the slopes of the oblique lines displayed in D  
1325 (0.02, 0.12 and 0.48, respectively). (F) The data points in A are superimposed on the two-  
1326 parameters bifurcation diagram shown in D, demonstrating a good agreement between  
1327 our basic model and experimental data (the same color code as in A for the different  
1328 clusters). The bifurcation diagram is simplified compared to A, only the region where  
1329 repetitive spiking is possible (i.e. between the lines  $SN_1$  and  $SN_2$  in A) being displayed  
1330 (shaded area). Notice that 3 ME cells (purple dots) are located close to the transition  
1331 between the RS and PP regions. The four arrows indicate the presumable evolution of  $G_{Nap}$   
1332 and  $G_{Kdr}$  for SS, RS, ME and PP cells between E12.5 and E14.5-15.5.  $G_{Nap}$  eventually  
1333 decreases while  $G_{Kdr}$  keeps on increasing. (G) Distribution of a sample of cells in the  $G_{Kdr}$  -

1334  $G_{Kdr}$  plane at E14.5. All the cells are located well within the SS region far from bifurcation  
1335 lines because of the decreased  $G_{Nap}$  compared to E12.5, the increased  $G_{Kdr}$ , and the shift  
1336 of the RS region (shaded) due to capacitance increase (18 versus 13 pF).

1337

1338 **Figure 8. Effects of the slow inactivation of  $I_{Nap}$  on firing patterns predicted by**  
1339 **computational modeling**

1340 (A) Examples of repetitive plateaus (left) and mixed events (right) recorded in V1<sup>R</sup> at E12.5  
1341 during a 2 s current pulse. (B1) Current-voltage curve of the basic model (without slow  
1342 inactivation of  $I_{Nap}$ , and without  $I_A$  or channel noise) for  $G_{Kdr} = 5$  nS and for  $G_{Nap} = 1.65$   
1343 nS (lower curve) and 2 nS (upper curve). Solid lines denote stable fixed points and dashed  
1344 lines unstable ones. For  $G_{Nap} = 1.65$  nS, bistability between quiescence and plateau occurs  
1345 between 1.39 and 10.48 pA. When  $G_{Nap}$  is increased to 2 nS, the bistability region ranges  
1346 from -10.84 to 9.70 pA, thus extending into the negative current range. This implies that  
1347 once a plateau has been elicited, the model will stay in that stable state and not return to  
1348 the resting state, even though current injection is switched off (see insert). B1 Insert.  
1349 Voltage response to a 2 s current pulse of 15 pA for  $G_{Nap} = 2$  nS. The resting state (gray dot  
1350 on the lower curve in B1) is destabilized at pulse onset and a plateau is elicited (blue dot on  
1351 the upper curve in B1). At pulse offset, the plateau is maintained, even though the injected  
1352 current is brought back to zero, and channel noise is not sufficient to go back to the resting  
1353 state. (B2) Domain of bistability between quiescence and plateau (shaded) in the  $I$ -  
1354  $G_{Nap}$  plane for  $G_{Kdr} = 5$  nS. It is delimited by the line SN<sub>2</sub> where a SN bifurcation of fixed  
1355 points occurs and by the subcritical Hopf bifurcation line HB where the plateau becomes  
1356 unstable. Bistability requires that  $G_{Nap}$  exceeds 1.35 nS, and the domain of bistability  
1357 enlarges as  $G_{Nap}$  is increased further. The two horizontal lines correspond to the two cases

1358 shown in B1:  $G_{Nap} = 1.65$  nS and 2 nS. (C) Behavior of the model when slow inactivation is  
1359 incorporated. The bifurcation diagram of the basic model (without slow inactivation) for  $I =$   
1360 10 pA and  $G_{Kdr} = 5$  nS (same conventions as in Fig 7B) and the stable limit cycle (black solid  
1361 curve) obtained when slow inactivation is added are superimposed. The limit cycle is  
1362 comprised of four successive phases (see labels): 1) long plateau during which  $I_{Nap}$  slowly  
1363 inactivates, 2) fast transition to the quiescent state, 3) repolarization episode during which  
1364  $I_{Nap}$  slowly deinactivates, 4) fast transition back to the plateau. Each plateau starts with a  
1365 full-blown action potential followed by rapidly decaying spikelets. Note that the bifurcation  
1366 HB is subcritical here (unstable limit cycle shown by dashed red curve), at variance with  
1367 square wave bursting (supercritical bifurcation and stable limit cycle); this is a characteristic  
1368 feature of pseudo-plateau bursting. Note also that the plateau extends beyond the  
1369 bifurcation HB because it is only weakly unstable then. Responses to a 15 s current pulse  
1370 are shown on the right side. Top left: voltage response ( $G_{Nap} = 2.5$  nS), Top right: behavior  
1371 of the “effective” conductance of  $I_{Nap}$  channel, i.e., the maximal conductance  $G_{Nap}$   
1372 multiplied by the slow inactivation variable  $s$ . Bottom left: voltage trace when channel  
1373 noise is added to fast and slow gating variables, Bottom right: Voltage trace when  $G_{Nap}$  is  
1374 increased by 50% to 3.75 nS. (D) Mixed events. The bifurcation diagram of the basic model  
1375 for  $G_{Kdr} = 5$  nS and  $I = 12$  pA and the stable limit cycle obtained in the presence of slow  
1376 inactivation ( $G_{Nap} = 2.5$  nS) are superimposed. Here again, the limit cycle is comprised of  
1377 four successive phases (see labels): 1) slow inactivation of  $I_{Nap}$  that leads to the crossing of  
1378 the bifurcation point  $HB_2$  and then to the destabilization of the plateau potential, 2) fast  
1379 transition to the spiking regime, 3) repetitive spiking during which  $I_{Nap}$  slowly de-  
1380 inactivates, which leads to the crossing of the bifurcation point  $SN_2$  and terminates the  
1381 spiking episode, 4) fast transition back to the stable plateau potential. Response to a 15 s

1382 current pulse of 12 pA is shown on the right in the absence of any channel noise. Top:  
1383 Voltage trace (same labels as in the bifurcation diagram on the left), Bottom: Variations of  
1384 the “effective” conductance  $G_{NapS}$  (same labels as in the voltage trace). Note that de-  
1385 inactivation sufficient to trigger a new plateau occurs over a series of successive spikes,  
1386 hence the small oscillations are visible on the trace. Note also that in C and D the first  
1387 plateau lasts longer than the following ones, as in electrophysiological recordings of  
1388 embryonic V1<sup>R</sup> cells displaying repetitive plateaus. This form of adaptation is caused by the  
1389 slow inactivation of the persistent sodium current.

1390

1391

## 1392 **Supplementary legends**

### 1393 **Figure 2—figure supplement 1. Effect of 4-AP on $I_{Kdr}$ and $I_A$ in embryonic V1<sup>R</sup>**

1394 (A1) Example of voltage-dependent potassium currents evoked in response to 10 mV  
1395 membrane potential steps (200 ms) from -100 mV or from -30 mV to +40 mV (10 s interval  
1396 between pulses). V1<sup>R</sup> were voltage clamped at  $V_H = -60$  mV. A prepulse of -40 mV (300 ms)  
1397 was applied to activate both  $I_A$  and  $I_{Kdr}$ .  $I_{Kdr}$  was evoked in response to 10 mV membrane  
1398 potential steps (200 ms) from -100 mV to +40 mV. V1<sup>R</sup> were voltage clamped at  $V_H = -60$   
1399 mV. A prepulse of 30 mV ( $V_H = -30$  mV) was applied to isolate  $I_{Kdr}$ . (A1) Representative  
1400 example of the effect of 300  $\mu$ M 4-AP application on  $I_{Kdr}$  recorded from embryonic V1<sup>R</sup> at  
1401 E12.5. (B1) Curves showing current-voltage relationships of  $I_{Kdr}$  in control and in the  
1402 presence of 300  $\mu$ M 4-AP. Measurements were performed on traces shown in A1. (C1)  
1403 Dose-response relationship of 4-AP-evoked  $I_{Kdr}$  inhibition (mean + SE). Data were  
1404 normalized to  $I_{Kdr}$  amplitude measured in the absence of 4-AP ( $V_H = 40$ mV) and fitted as  
1405 explained in Materials and Methods. Note that 4-AP IC<sub>50</sub> is in  $\mu$ M range (2.9  $\mu$ M). 0.3  $\mu$ M 4-  
1406 AP n = 3; N = 3, 1  $\mu$ M 4-AP n = 3; N = 3, 3  $\mu$ M 4-AP n = 9; N = 9, 10  $\mu$ M 4-AP n = 13; N = 13,  
1407 30  $\mu$ M 4-AP n = 7; N = 7, 100  $\mu$ M 4-AP n = 7; N = 7, 300  $\mu$ M 4-AP n = 7; N = 7. (A2)  $I_A$  was  
1408 obtained as the difference between currents evoked from  $V_H = -100$  mV and currents  
1409 evoked from  $V_H = -30$  mV (10 mV voltage step). (A2) Representative example of the effect  
1410 of 300  $\mu$ M 4-AP on  $I_A$  in V1<sup>R</sup> recorded at E12.5. (B2)  $I_A$  Current-voltage ( $I - V$ ) relationship  
1411 in control conditions and in the presence of 300  $\mu$ M 4-AP. The  $I - V$  curves were obtained  
1412 from the traces shown in A1. (C2) Bar graph showing the percentage of  $I_A$  block elicited by  
1413 4-AP. Note that 4-AP did not significantly block  $I_A$  (Wilcoxon test  $P = 0.065$ , n = 10).

1414

1415 **Figure 2—figure supplement 2. Relates to Fig 2. Effect of 4-AP application in repetitively**  
1416 **spiking V1<sup>R</sup> at E12.5**

1417 (A) Representative traces showing the effect of 4-AP application (300  $\mu$ M) on Repetitive  
1418 Spiking (RS) V1<sup>R</sup> at E12.5. Note that plateau potential activity evoked in the presence of 4-  
1419 AP (middle trace) was blocked by 0.5  $\mu$ M TTX (right trace). (B) Bar plots showing the  
1420 changes in the firing pattern of RS V1<sup>R</sup> evoked by 300  $\mu$ M 4-AP application (n = 14). 4-AP  
1421 application evoked a plateau potential in 71.4 % of the recorded neurons (10/14) and  
1422 mixed events in 14.3% of the recorded neurons (2/14). The excitability pattern was not  
1423 modified in 2 neurons. Repetitive Spiking (RS) V1<sup>R</sup> (red), Mixed events (ME) V1<sup>R</sup> (purple),  
1424 Plateau Potential (PP) V1<sup>R</sup> (blue).

1425

1426 **Figure 3—figure supplement 1. Distributions of log  $\frac{1}{2}$ Ad, CV  $\frac{1}{2}$ Ad and log ddr values**  
1427 **related to the cluster analysis of embryonic V1<sup>R</sup> firing patterns**

1428 (A1) Histogram of log mean  $\frac{1}{2}$ Ad (mean half amplitude event duration) for the whole V1<sup>R</sup>  
1429 population at E12.5 (n= 164; bin width 0.1). The histogram was well fitted by the sum of  
1430 three Gaussian curves with means and SDs of 1.135, 2.046 & 2.84, and 0.316, 0.181 & 0.21,  
1431 respectively. (A2) Histogram of the values of log mean  $\frac{1}{2}$ Ad sorted after cluster analysis  
1432 showing single spiking (SS) V1<sup>R</sup> (gray), repetitive spiking (RS) V1<sup>R</sup> (red), mixed events (ME)  
1433 V1<sup>R</sup> with short plateau potentials (ME short PP V1<sup>R</sup>, light purple), ME V1<sup>R</sup> with long plateau  
1434 potentials (ME long PP V1<sup>R</sup>, dark purple) and plateau potential (PP) V1<sup>R</sup> (blue). log mean  
1435  $\frac{1}{2}$ Ad was significantly different between SS V1<sup>R</sup>, PP V1<sup>R</sup>, the whole ME V1<sup>R</sup> population (ME<sub>s</sub>  
1436 and ME<sub>l</sub> V1<sup>R</sup>) and PP V1<sup>R</sup> (Kruskall-Wallis test  $P < 0.0001$ ; SS V1<sup>R</sup> versus RS V1<sup>R</sup>,  $P < 0.0001$ ;  
1437 SS V1<sup>R</sup> versus ME V1<sup>R</sup>,  $P < 0.0001$ ; SS V1<sup>R</sup> versus PP V1<sup>R</sup>,  $P < 0.0001$ ; RS V1<sup>R</sup> versus ME V1<sup>R</sup>,  $P$   
1438 = 0.0004; RS V1<sup>R</sup> versus PP V1<sup>R</sup>,  $P < 0.0001$ ; ME V1<sup>R</sup> versus PP V1<sup>R</sup>,  $P = 0.018$ ; SS V1<sup>R</sup> n = 46,

1439 RS V1<sup>R</sup> n = 69, ME<sub>s</sub> V1<sup>R</sup> n = 9, ME<sub>l</sub> V1<sup>R</sup> n = 4, PP V1<sup>R</sup> n = 35). (B1) Histogram of CV ½Ad for  
 1440 the whole V1<sup>R</sup> population at E12.5 (n= 164; bin width 5%). Note that a large population of  
 1441 V1<sup>R</sup> had zero CV ½Ad (n = 83). The histogram for CV ½Ad ≠ 0 was fitted by the sum of three  
 1442 Gaussian curves with means and SDs of 23.4, 68.4 & 117 (%) and 8.9, 6.8 & 4.1, respectively.  
 1443 (B2) Histograms of the values of CV ½Ad sorted after cluster analysis showing SS V1<sup>R</sup> (black),  
 1444 RS V1<sup>R</sup> (red), ME<sub>s</sub> V1<sup>R</sup> (light purple), ME<sub>l</sub> V1<sup>R</sup> (dark purple) and PP V1<sup>R</sup>. CV ½Ad was not  
 1445 significantly different between SS V1<sup>R</sup> and PP V1<sup>R</sup> (CV ½Ad of SS V1<sup>R</sup> and PP V1<sup>R</sup> = 0.682 %  
 1446 and 0% respectively: only one of the 46 SS V1<sup>R</sup> displayed 3 PA and had a CV ½Ad of 31.37).  
 1447 CV ½Ad was significantly different between RS V1<sup>R</sup> and the whole ME V1<sup>R</sup> population and  
 1448 also between SS V1<sup>R</sup> or PP V1<sup>R</sup> and RS V1<sup>R</sup> or ME V1<sup>R</sup> (Kruskall-Wallis test  $P < 0.0001$ ; SS V1<sup>R</sup>  
 1449 versus RS V1<sup>R</sup>  $P < 0.0001$ , SS V1<sup>R</sup> versus ME V1<sup>R</sup>  $P < 0.0001$ , SS V1<sup>R</sup> versus PP V1<sup>R</sup>  $P = 0.846$ ,  
 1450 RS V1<sup>R</sup> versus ME V1<sup>R</sup>  $P = 0.0003$ , RS V1<sup>R</sup> versus PP V1<sup>R</sup>  $P < 0.0001$ , ME V1<sup>R</sup> versus PP V1<sup>R</sup>  $P$   
 1451  $< 0.0001$ ). (C1) Histogram of log ddr (sum of ½Ad divided by pulse duration) for the whole  
 1452 V1<sup>R</sup> population at E12.5 (n= 164; bin width 0.2). The histogram was fitted by the sum of  
 1453 two Gaussian curves with means and SDs of -2.51 & -0.851, and 0.2 & 0.46, respectively.  
 1454 (C2) Histograms of the values of log ddr sorted after cluster analysis showing SS V1<sup>R</sup> (black),  
 1455 RS V1<sup>R</sup> (red), ME<sub>s</sub> V1<sup>R</sup> (light purple), ME<sub>l</sub> V1<sup>R</sup> (dark purple) and PP V1<sup>R</sup>. log (ddr) was not  
 1456 significantly different between ME V1<sup>R</sup> and PP V1<sup>R</sup>, while it was significantly different  
 1457 between SS V1<sup>R</sup> and RS V1<sup>R</sup>, SS V1<sup>R</sup> and the whole ME V1<sup>R</sup> population, SS V1<sup>R</sup> and PP V1<sup>R</sup>,  
 1458 RS V1<sup>R</sup> and the whole ME V1<sup>R</sup> population, RS V1<sup>R</sup> and PP V1<sup>R</sup> (Kruskall-Wallis test  $P < 0.0001$ ;  
 1459 SS V1<sup>R</sup> versus RS V1<sup>R</sup>,  $P < 0.0001$ ; SS V1<sup>R</sup> versus ME V1<sup>R</sup>,  $P < 0.0001$ ; SS V1<sup>R</sup> versus PP V1<sup>R</sup>,  $P$   
 1460  $< 0.0001$ ; RS V1<sup>R</sup> versus ME V1<sup>R</sup>,  $P < 0.0001$ ; RS V1<sup>R</sup> versus PP V1<sup>R</sup>,  $P < 0.0001$ ; ME V1<sup>R</sup>  
 1461 versus PP V1<sup>R</sup>,  $P = 0.977$ ). ME<sub>s</sub> V1<sup>R</sup> and ME<sub>l</sub> V1<sup>R</sup> differed only by their CV ½Ad (Mann-  
 1462 Whitney test, log mean ½Ad for ME<sub>s</sub> V1<sup>R</sup> versus log mean ½Ad for ME<sub>l</sub> V1<sup>R</sup>,  $P = 0.26$ ; CV

1463  $\frac{1}{2}$ Ad for ME<sub>s</sub> V1<sup>R</sup> versus CV  $\frac{1}{2}$ Ad ME<sub>i</sub> V1<sup>R</sup>,  $P = 0.0028$  and log ddr for ME<sub>s</sub> V1<sup>R</sup> versus log ddr  
1464 for ME<sub>i</sub> V1<sup>R</sup>,  $P = 0.1483$ ). It is noteworthy that the distribution of the values of each metric  
1465 was multimodal thus indicating that each of them could partially discriminate different  
1466 groups of embryonic V1<sup>R</sup> according to their firing pattern.

1467

1468 **Figure 6—figure supplement 1.  $I_{Nap}$  is present in embryonic V1<sup>R</sup> recorded at E14.5**

1469 (A) Representative trace of  $I_{Nap}$  evoked by a slow depolarizing voltage ramp (70 mV/s,  
1470 upper insert) in SS embryonic V1<sup>R</sup> (lower insert).  $I_{Nap}$  was isolated by subtracting currents  
1471 evoked by depolarizing ramps in the presence of 1  $\mu$ M TTX to the control current evoked in  
1472 the absence of TTX (upper insert). (B) Voltage dependence of  $G_{Nap}$  conductance calculated  
1473 from the trace shown in A. The activation curve was obtained by transforming the current  
1474 evoked by a depolarizing voltage ramp from -100 mV to 20 mV (70 mV/s) using the  
1475 following equation:  $G_{Nap} = -I_{Nap}/((-V_h)+E_{Na})$  where  $V_h$  is the holding potential at time  $t$   
1476 during a depolarizing voltage ramp and  $E_{Na}$  is the equilibrium potential for sodium ( $E_{Na} = 60$   
1477 mV). The  $G_{Nap}/V_h$  curve was fitted with the following Boltzmann function:  $G =$   
1478  $G_{MAX}/(1+\exp(-(V-V_{HALF})/k))$  (Boeri et al. 2018), where  $V_{half}$  is the  $V_h$  value for  $G_{Nap}$  half  
1479 activation,  $k$  the slope factor of the curve and  $G_{max}$  the maximum conductance. We found  
1480 no significant difference between the values of  $V_{half}$  (Mann-Whitney test:  $P = 0.8518$ ) and  
1481 of  $k$  (Mann-Whitney test:  $P = 0.7546$ ) obtained at E12.5 (Boeri et al. 2018) and those  
1482 obtained at E14.5. At E14.5  $V_{half} = -27 \pm 5.1$  mV and  $k = 7.73 \pm 0.78$  (n = 6).

1483

1484 **Figure 6—figure supplement 2.  $I_{Kdr}$  was inhibited by 4-AP in V1<sup>R</sup> recorded at E14.5**

1485 (A1) Representative examples of the total outward K<sup>+</sup> currents obtained from  $V_H = -100$  mV  
1486 (left traces), of  $I_{Kdr}$  ( $V_H = -30$  mV, middle traces) and of isolated  $I_A$  (left traces) recorded in

1487 single spiking (SS)  $V1^R$  at E14.5. (A2) Current-voltage relationship of  $I_{Kdr}$  (filled circle) and  
1488 of  $I_A$  (open circle) in SS  $V1^R$  at E14.5.  $I - V$  curves were obtained from currents shown in  
1489 A1. (B1) Representative example of the effect of 4-AP at 600  $\mu\text{M}$  in  $V1^R$  at E14.5. (B2)  
1490 Current-voltage curves in control condition and in the presence of 600  $\mu\text{M}$  4-AP. (B3) Bar  
1491 plots showing the percentage of  $I_{Kdr}$  inhibition evoked by 300  $\mu\text{M}$  4-AP application ( $n = 8$ )  
1492 and by 600  $\mu\text{M}$  4-AP application ( $n = 7$ ). The percentages of  $I_{Kdr}$  inhibition evoked by 300  
1493  $\mu\text{M}$  4-AP and by 600  $\mu\text{M}$  4-AP applications were not significantly different ( $P = 0.574$ ). (C1)  
1494 Representative example of the effect of 600  $\mu\text{M}$  4-AP on  $I_A$  in  $V1^R$  recorded at E14.5. (C2)  
1495  $I - V$  curves in control conditions and in the presence of 600  $\mu\text{M}$  4-AP. These curves were  
1496 obtained from the traces shown in B1. (C3) Bar graph showing the percentage of  $I_A$  block  
1497 elicited by 4-AP. 4-AP did not significantly block  $I_A$  (Wilcoxon test  $P = 0.11$ ,  $n = 6$ ).

1498

1499 **Figure 7—figure supplement 1. Effects of  $I_A$  on embryonic  $V1^R$  firing patterns predicted**  
1500 **by computational modeling**

1501 (A) The maximal conductances of  $I_{Kdr}$  and  $I_A$  at E12.5 are linearly correlated. Best fit:  $G_A =$   
1502  $1.09 G_{Kdr}$  ( $R^2 = 0.81$ ,  $N=44$ ). (B) Effect of  $I_A$  on the dynamics of the basic model. The one-  
1503 parameter bifurcation diagrams in control condition (black,  $I = 20$  pA,  $G_{Kdr} = 10$  nS, no  
1504  $I_A$ , same as in Fig 7B) and with  $I_A$  added (orange,  $G_A = 10$  nS) are superimposed. The  
1505  $I_A$  current shifts the firing threshold  $SN_1$  to the right by 0.18 nS (see also C) as indicated by  
1506 the orange arrow, with little effect on the amplitude of action potentials (see also insert in  
1507 C). In contrast,  $I_A$  shifts  $SN_2$  by only 0.03 nS because it is inactivated by depolarization. (C)  
1508  $I_A$  also slows down the discharge frequency, as shown by comparing the  $G_{Nap} - V$  curves  
1509 without  $I_A$  (black) and with  $I_A$  (orange). For  $G_{Nap} = 1$  nS, for instance, the firing frequency is  
1510 reduced by 31%, from 15 to 10.4 Hz. Here again, the effect of  $I_A$  progressively decreases as

1511  $G_{Nap}$  increases because of the membrane depolarization elicited by  $I_{Nap}$ . For  $G_{Nap} = 2.4$  nS,  
1512 for instance, the firing frequency is reduced by 11% only, from 19.1 to 17 Hz. This  
1513 frequency reduction elicited by  $I_A$  does not merely result from the increased firing  
1514 threshold. Note also that the latency of the first spike is increased (see voltage trace in  
1515 insert), which is a classical effect of  $I_A$ . (D)  $I_A$  reduces the frequency of pseudo-plateau  
1516 bursting by lengthening quiescent episodes (doubling their duration in the example shown)  
1517 without affecting the duration of plateaus much (here a mere 5% increase), as shown by  
1518 the comparison of the voltage traces obtained without  $I_A$  (control,  $G_{Kdr} = 2.5$  nS, black)  
1519 and with  $I_A$  ( $G_{Kdr} = G_A = 2.5$  nS, orange). This is because  $I_A$  is activated near rest but  
1520 inactivated during voltage plateaus. Note that increasing  $G_{Kdr}$ , in the absence of  $I_A$  has not  
1521 the same effect; it shortens both plateaus and quiescent episodes (see Fig 8C, where  
1522  $G_{Kdr} = 5$  nS). Again, this is because  $I_{Kdr}$  does not inactivate (or does it only very slowly), in  
1523 contrast to  $I_A$ .

1524

### 1525 **Figure 7—figure supplement 2. Explaining the effect of 4-AP on the firing pattern**

1526 The RS region of the basic model, where repetitive firing may occur, is displayed in the  
1527  $G_{Nap} - G_{Kdr}$  plane in control condition for E12.5 V1<sup>R</sup> ( $C_{in} = 13$  pF,  $G_{in} = 1$  nS,  $I = 20$  pA,  
1528 shaded area), and when  $G_{in}$  and  $I$  were both reduced by 25% (middle curve) or by 50% (left  
1529 curve). The reduced  $I$  accounts for the decrease in rheobase, and thus in the current  
1530 injected in the experiments, following the decrease in  $G_{in}$ . If 4-AP reduced only  $G_{Kdr}$  (as  
1531 indicated by the downward arrow) the firing pattern of SS V1<sup>R</sup> would not change, the RS  
1532 region being too far to the right to be visited. In contrast, when the effects of 4-AP on the  
1533 input conductance and rheobase are taken into account, the bifurcation diagram moves  
1534 leftwards and downwards, as indicated by the oblique black arrow, and the RS and PP

1535 regions are then successively entered as  $G_{Kdr}$  is reduced. The same explanation holds at

1536 E14.5.

1537

1538 **Figure 3-souce data-1**

1539 Numerical data used to perform cluster analysis shown in Figure 3

1540

1541 **TABLE 1 Model parameters**

Parameter	Basic model	Model with slow inactivation of $I_{Nap}$
<b>Passive parameters</b>		
Input conductance $G_{in}$	1 nS	same
Input capacitance $C_{in}$	13 pF (E12.5, Figs. 7B, C, D and F and 8B to D) or 18 pF (E14.5, Fig. 7G)	13 pF
Resting potential $V_r$	-60 mV	same
Injected current $I$	20 pA (Fig. 7B to G)	10 pA (Fig. 8C) or 12 pA (Fig. 8D) variable in Fig. 8B
<b>Transient sodium current <math>I_{Nat}</math></b>		
Maximal conductance $G_{Nat}$	20 nS	same
Reversal potential $E_{Na}$	60 mV	
Activation exponent	3	
Mid-activation $V_m$	-26 mV	
Steepness of activation $k_m$	9.5 mV	
Activation time constant	1.5 ms	
Mid-inactivation $V_h$	-45 mV	
Steepness of inactivation $K_h$	-5 mV	
Inactivation time constant $\tau_m$	Voltage-dependent (see Material and Methods)	
<b>Persistent sodium current <math>I_{Nap}</math></b>		
Maximal conductance	variable (see text and figure captions)	same
Mid-activation voltage	-36 mV	same
Mid-inactivation $V_s$		-30 mV
Steepness of inactivation $k_s$		-5 mV
Inactivation time constant	Slow inactivation not included	2 s
<b>Delayed rectifier potassium current <math>I_{Kdr}</math></b>		
Maximal conductance $G_{Kdr}$	variable (see text and figure captions)	same
Reversal potential $E_K$	-96 mV	
Activation exponent	3	
Mid-activation $V_n$	-20 mV	
Steepness of activation $k_n$	15 mV	
Activation time constant $\tau_m$	10 ms	
<b>Potassium A current <math>I_A</math> (when included in the basic model)</b>		
Maximal conductance $G_A$	Equal to $G_{Kdr}$	never included
Mid-activation $V_{mA}$	-30 mV	
Steepness of activation $k_{mA}$	12 mV	
Activation time constant	Instantaneous activation	
Mid-inactivation $V_{hA}$	-70 mV	

Steepness of inactivation $k_{hA}$	-7 mV
Inactivation time constant $\tau_{hA}$	23 ms

1542

1543

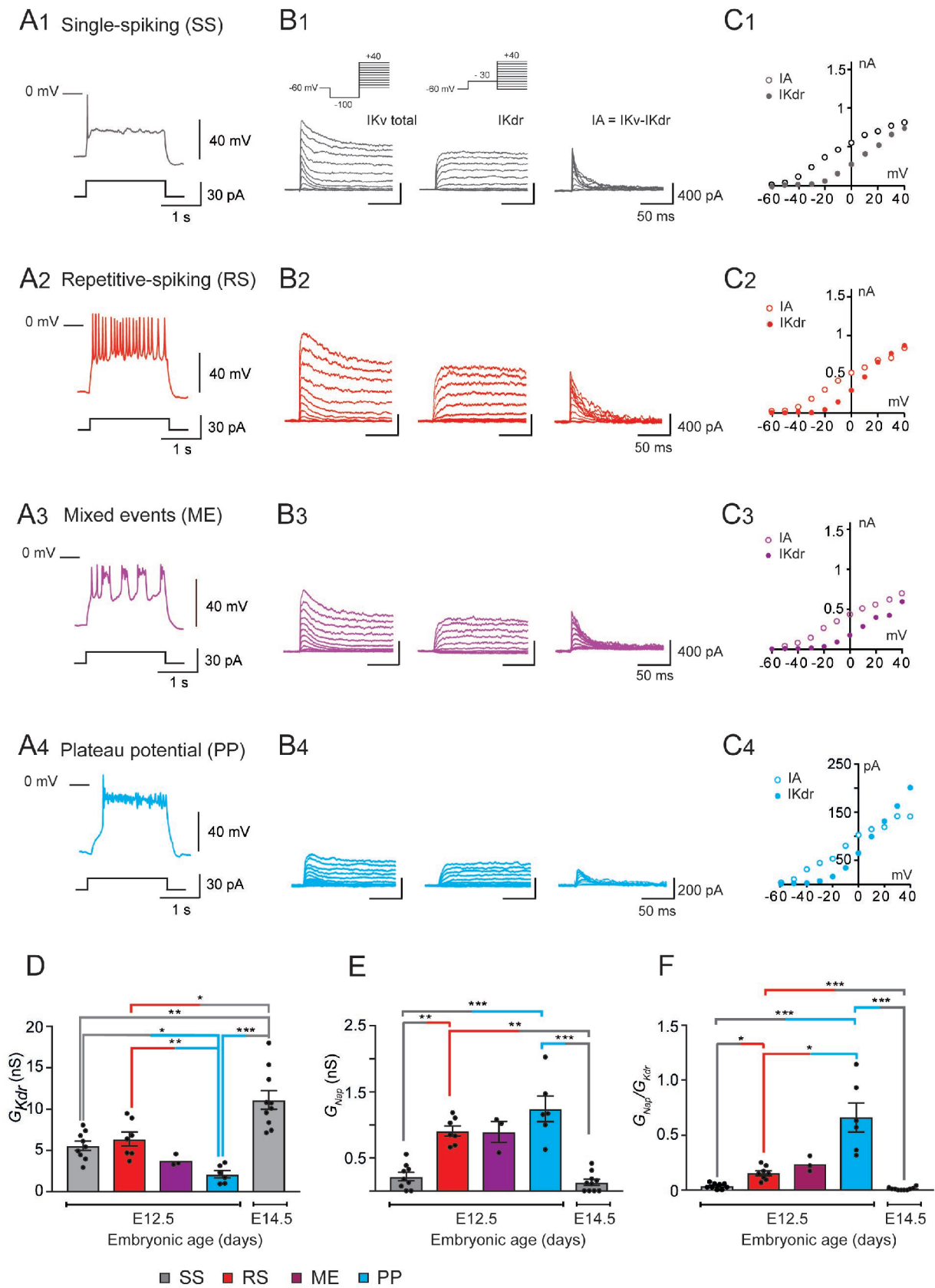


Fig 1

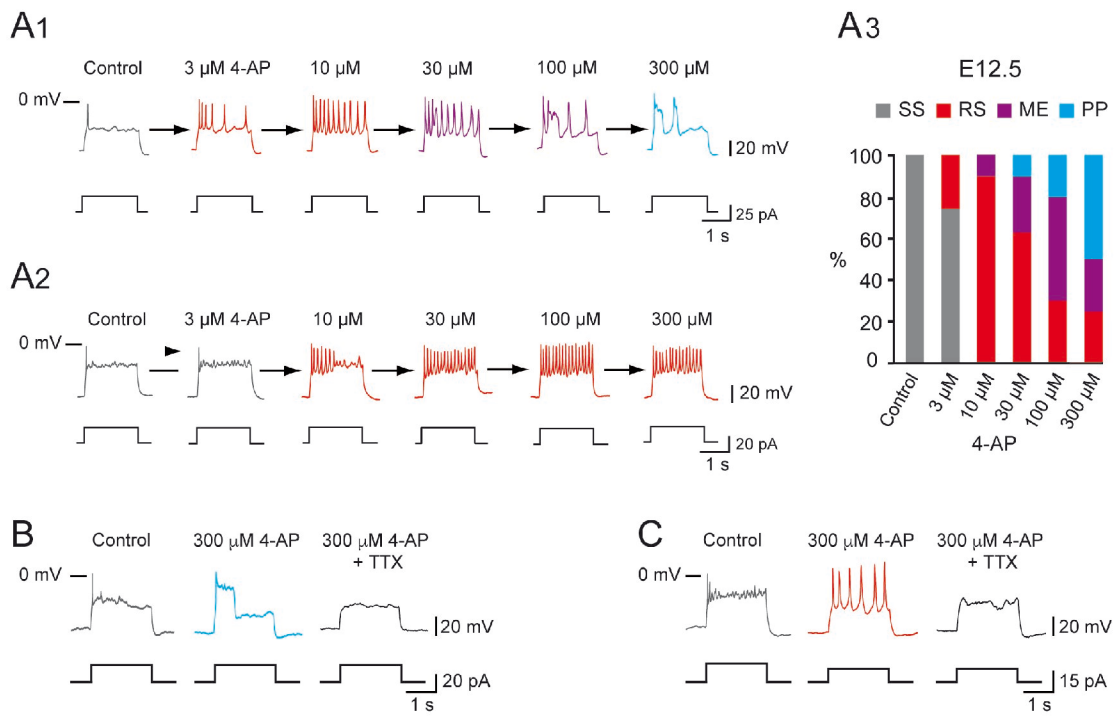
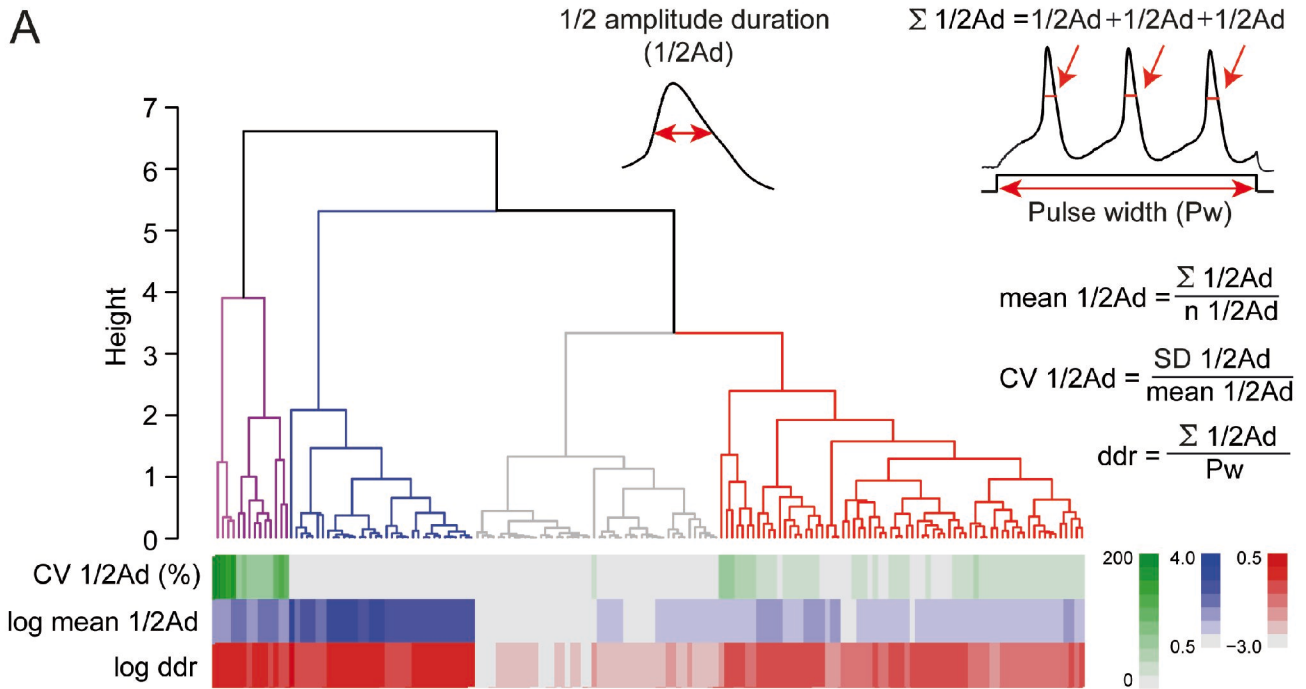
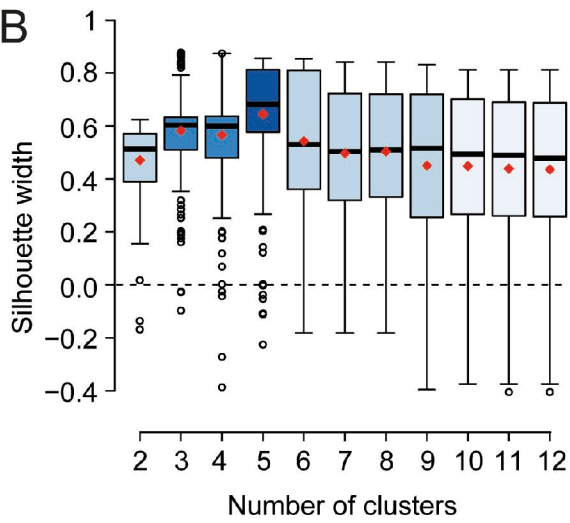
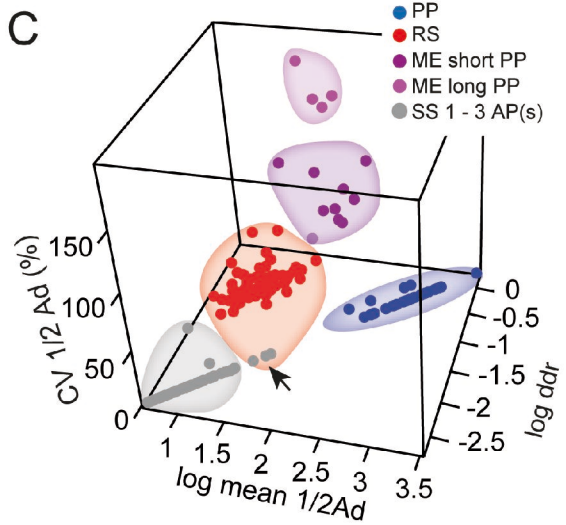
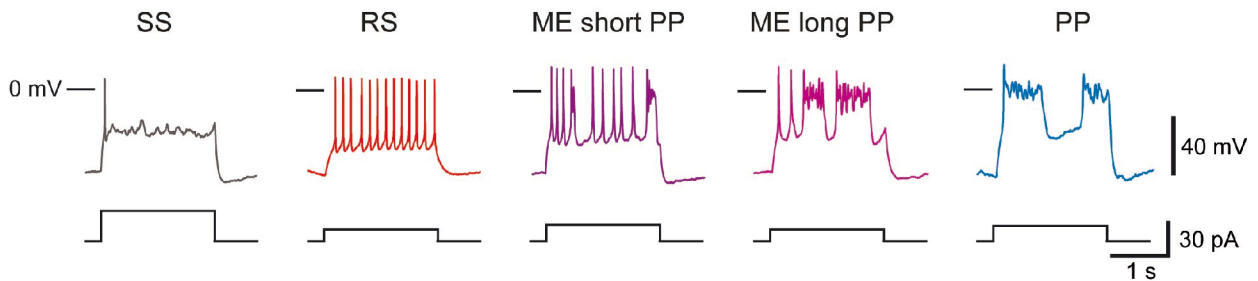
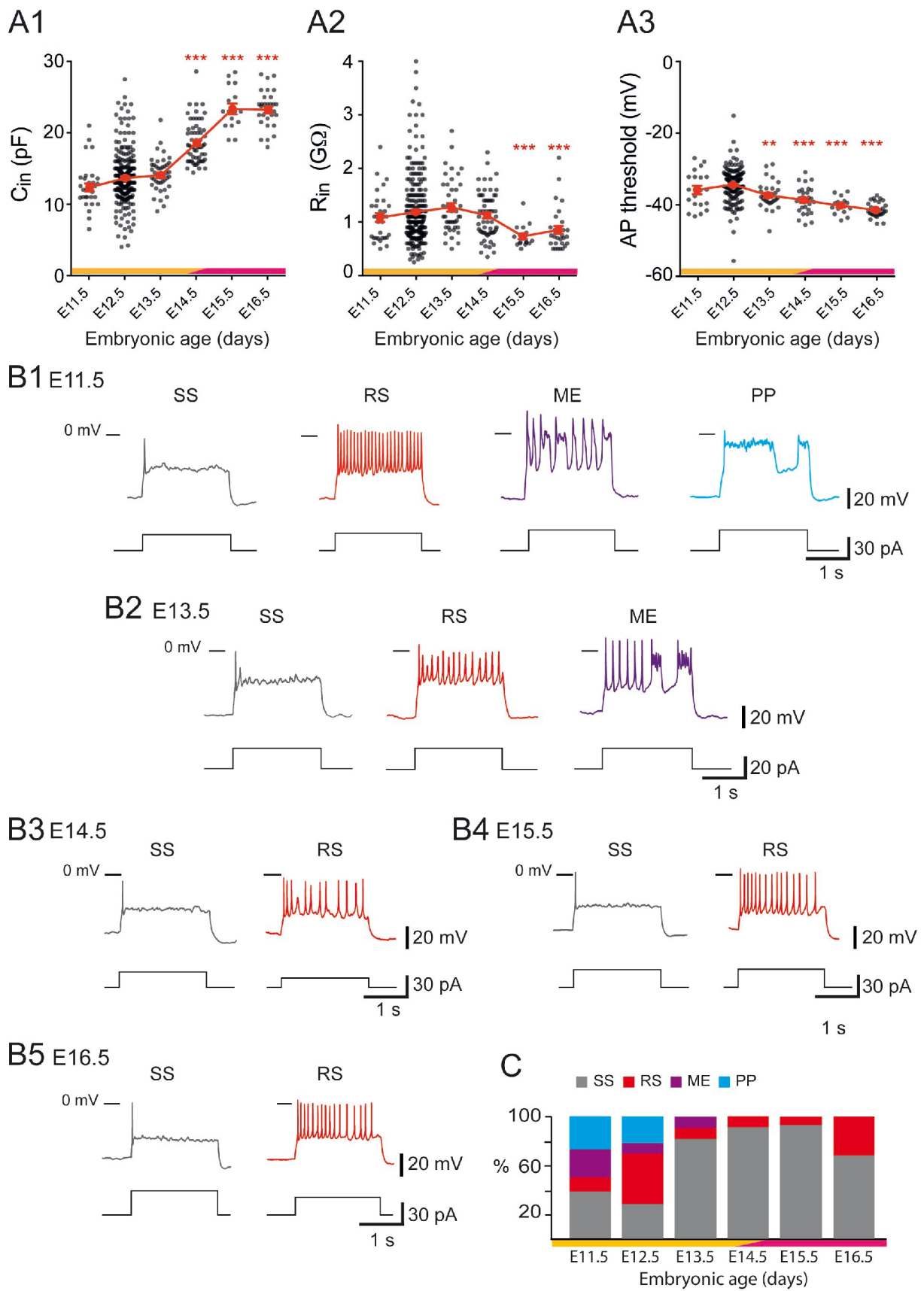


Fig 2

**A****B****C****D****Fig 3**



**Fig 4**

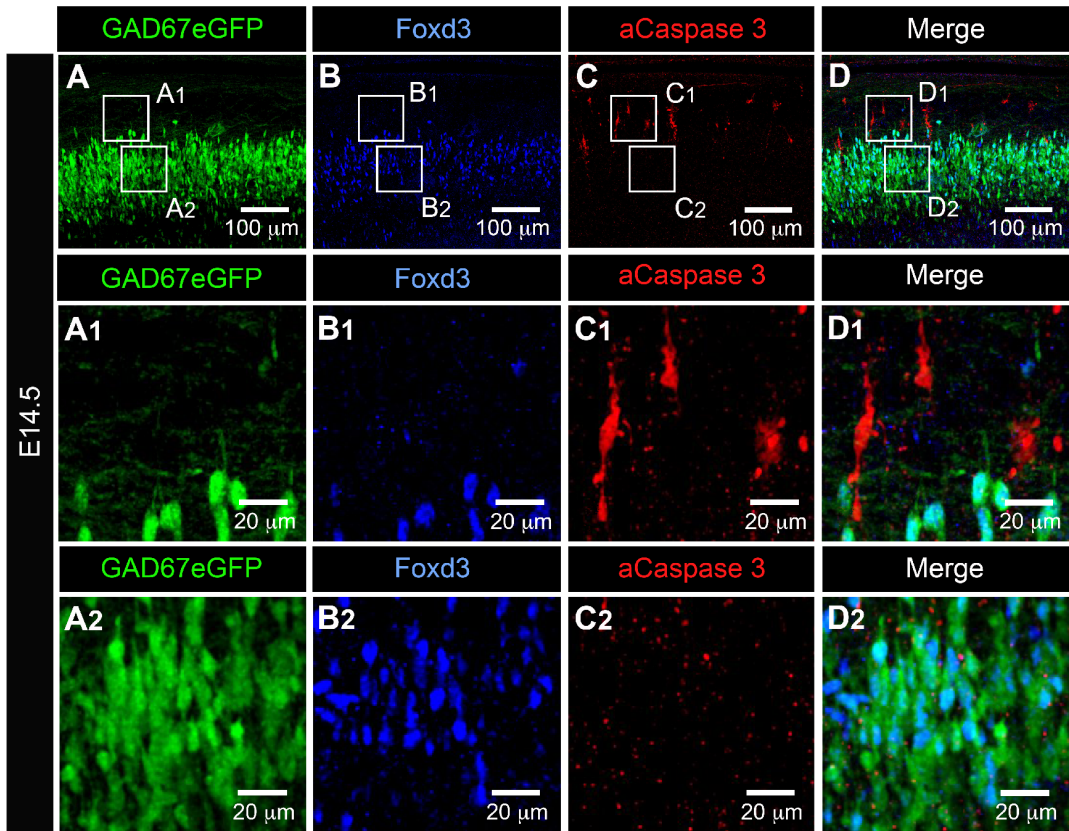


Fig 5

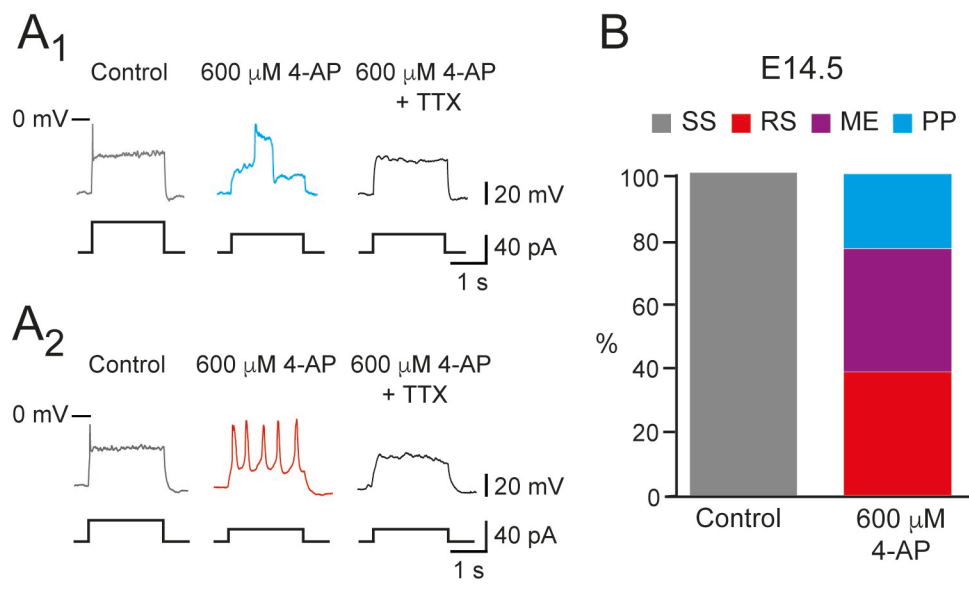


Fig 6

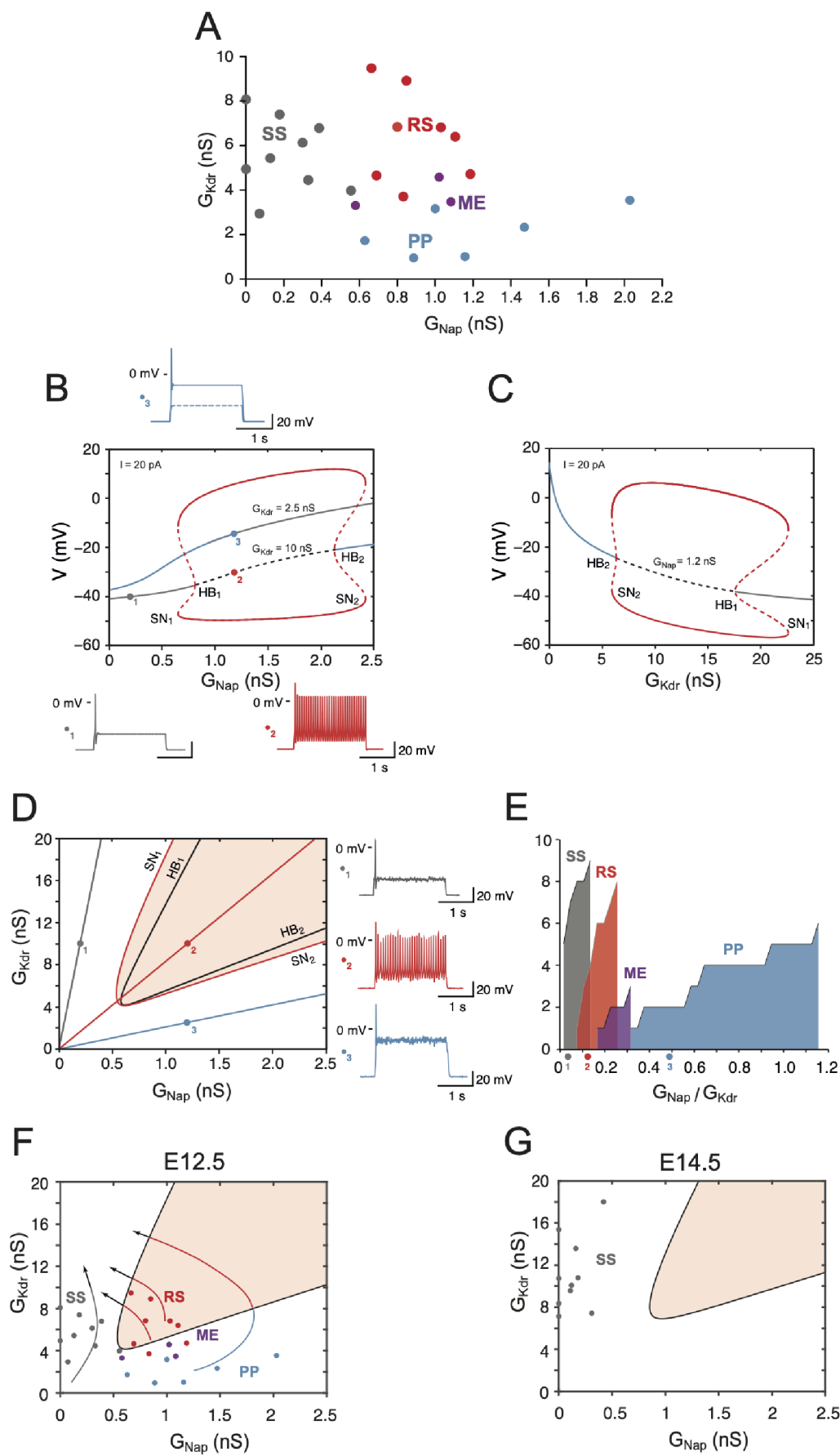


Fig 7

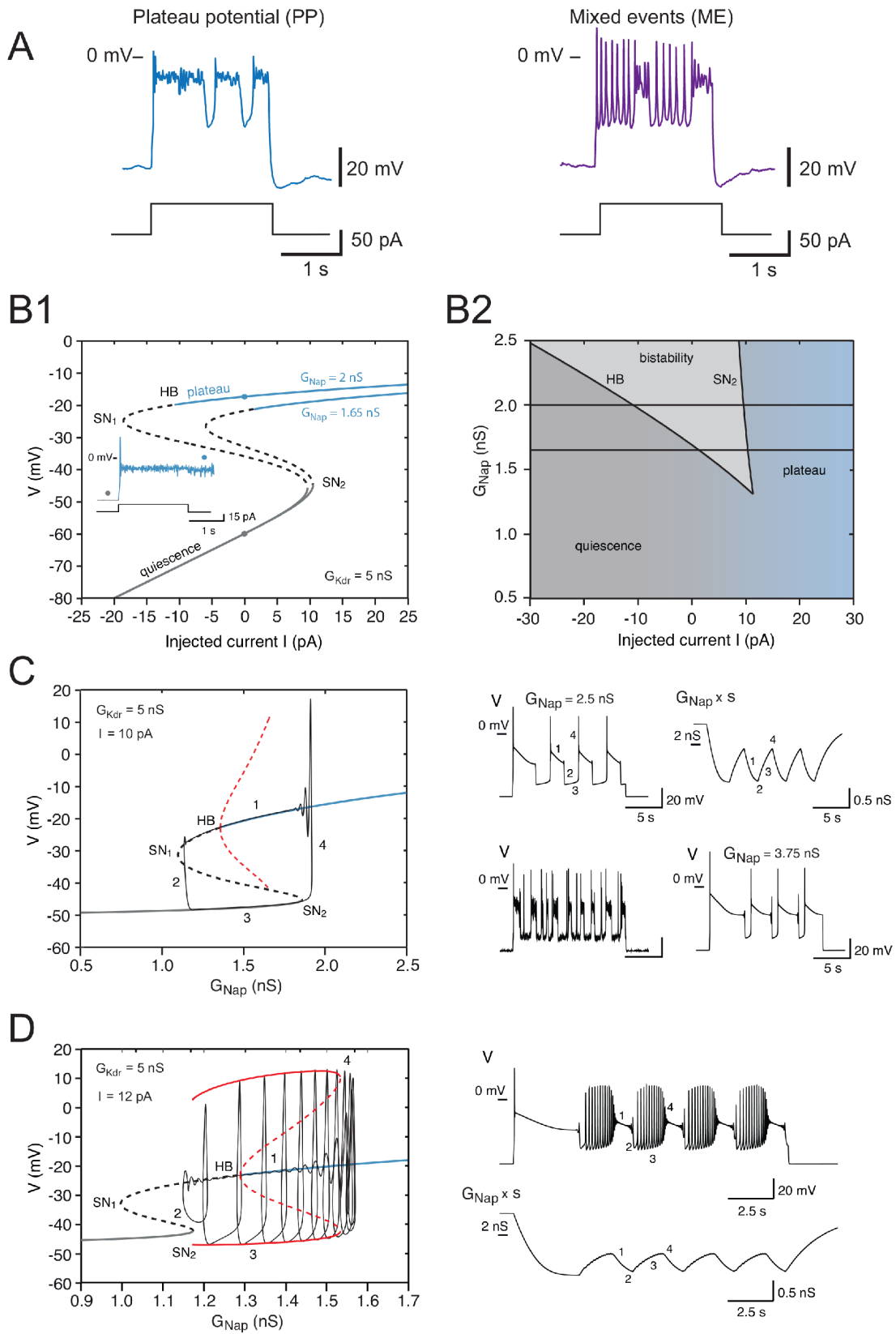
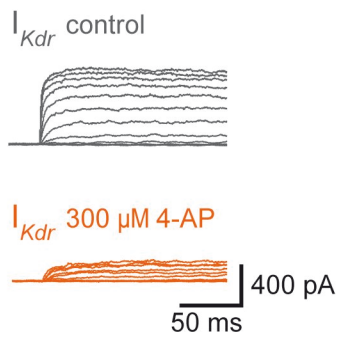
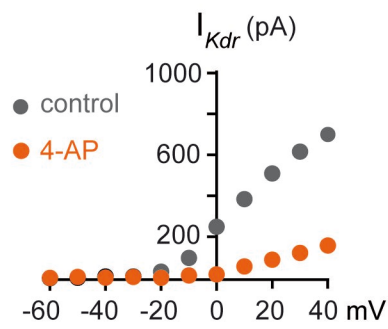


Fig 8

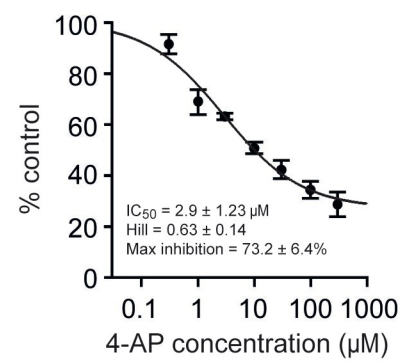
A1 E12.5



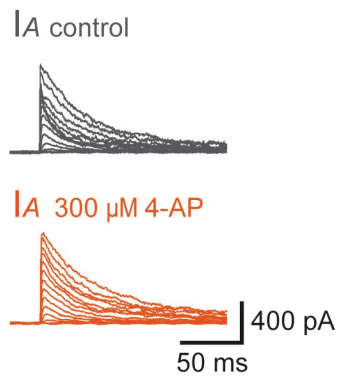
B1



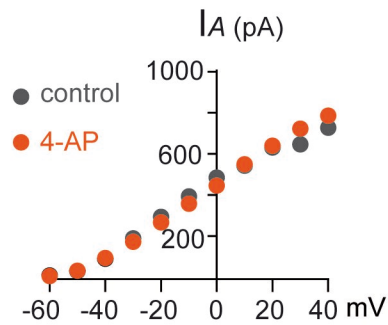
C1



A2 E12.5



B2



C2

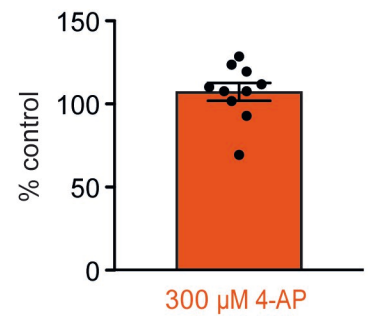


Fig 2 figure supplement 1

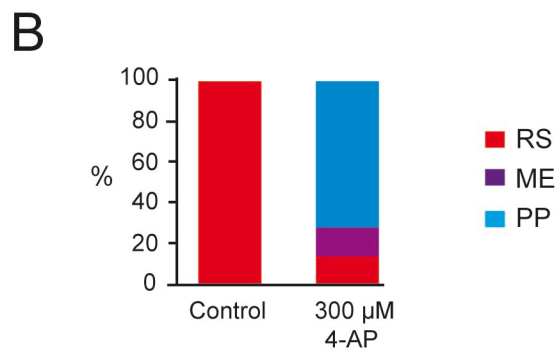
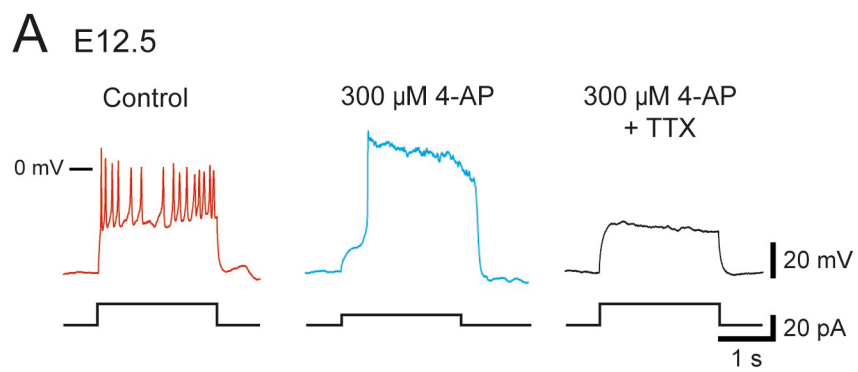


Fig 2 figure supplement 2

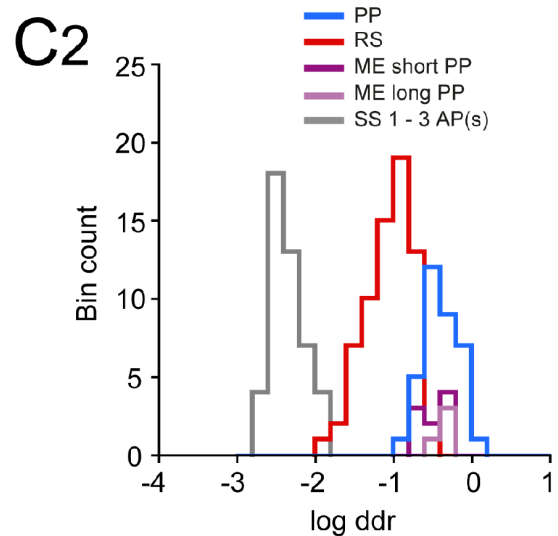
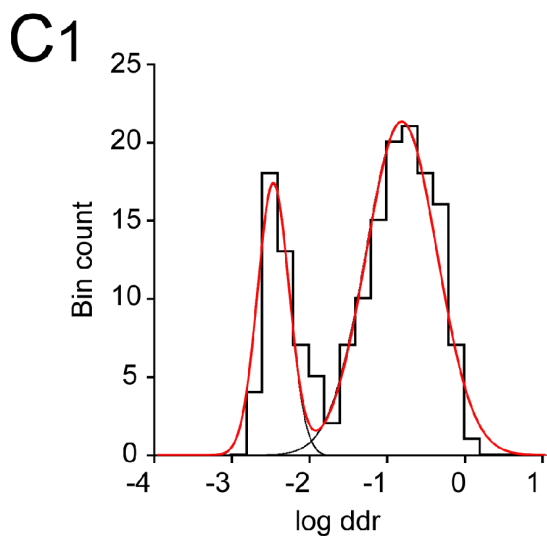
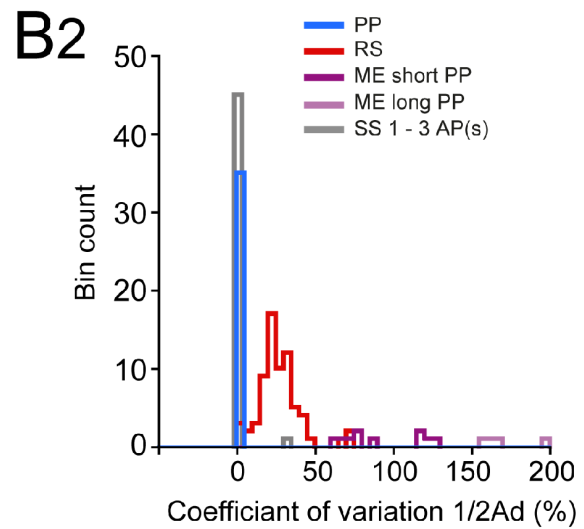
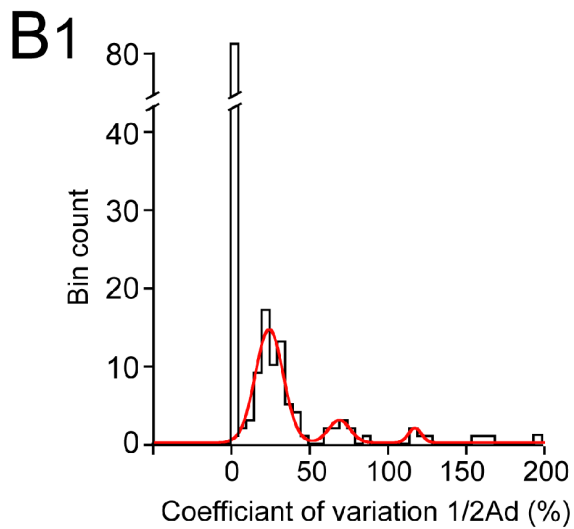
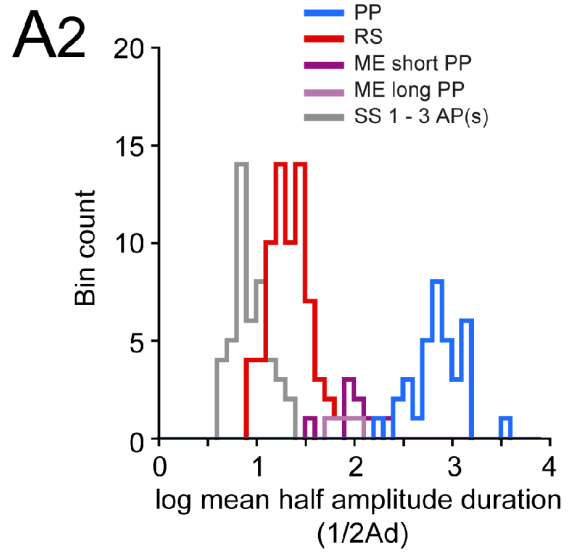
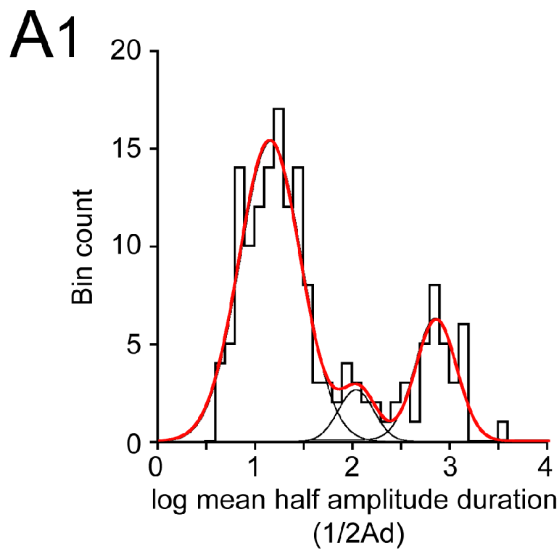


Fig 3 figure supplement 1

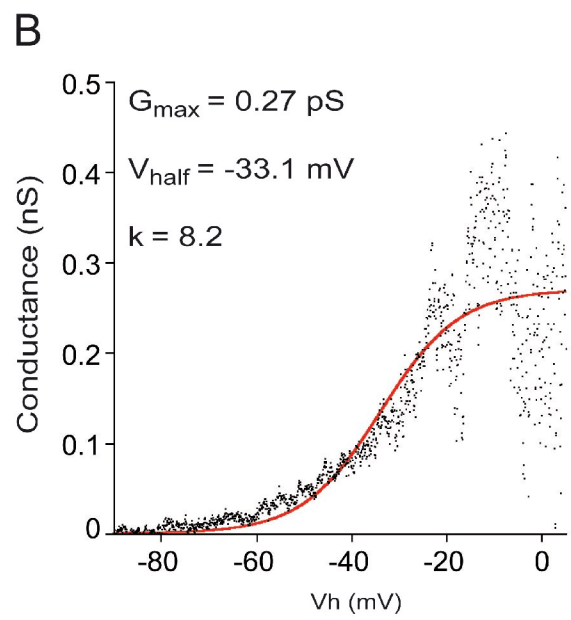
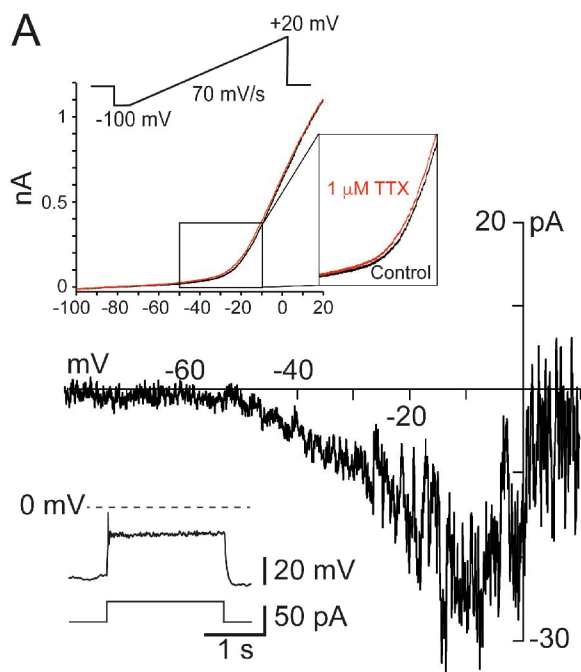
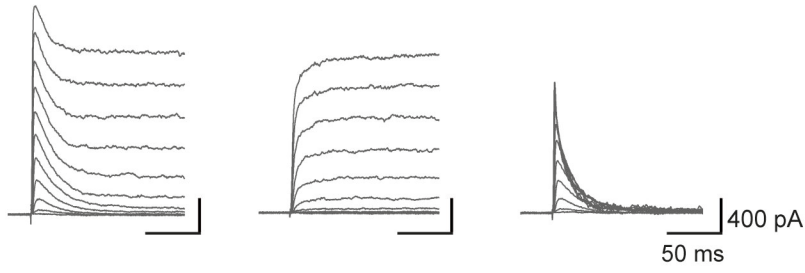
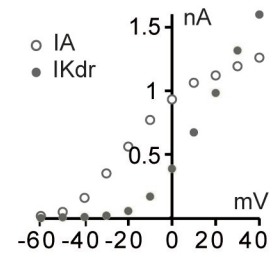


Fig 6 figure supplement 1

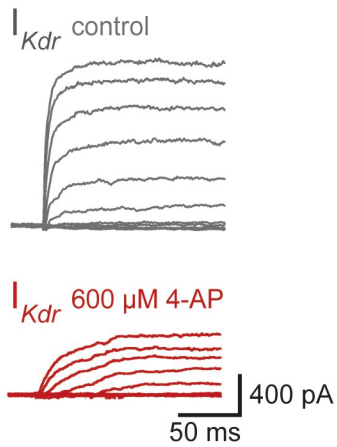
A1 SS (E14.5)



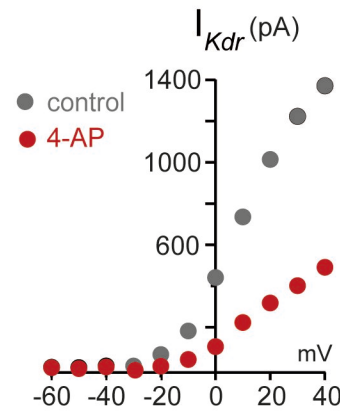
A2



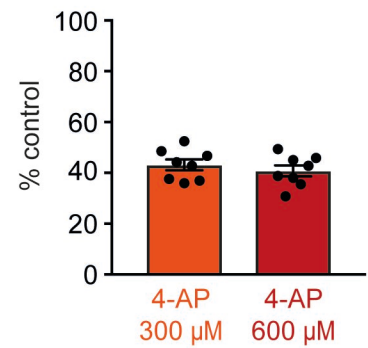
B1



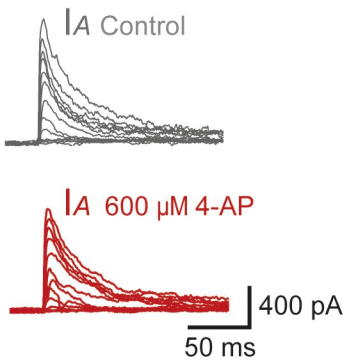
B2



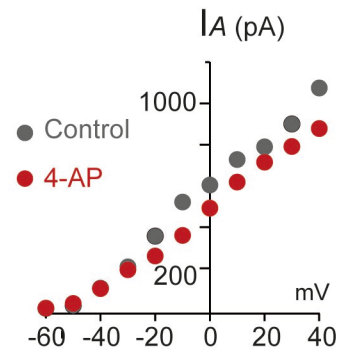
B3



C1



C2



C3

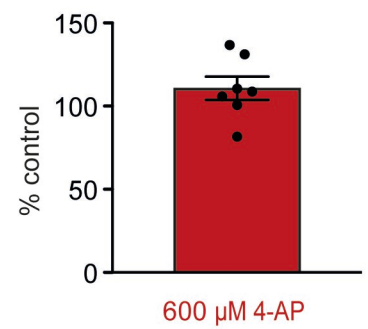


Fig 6 figure supplement 2

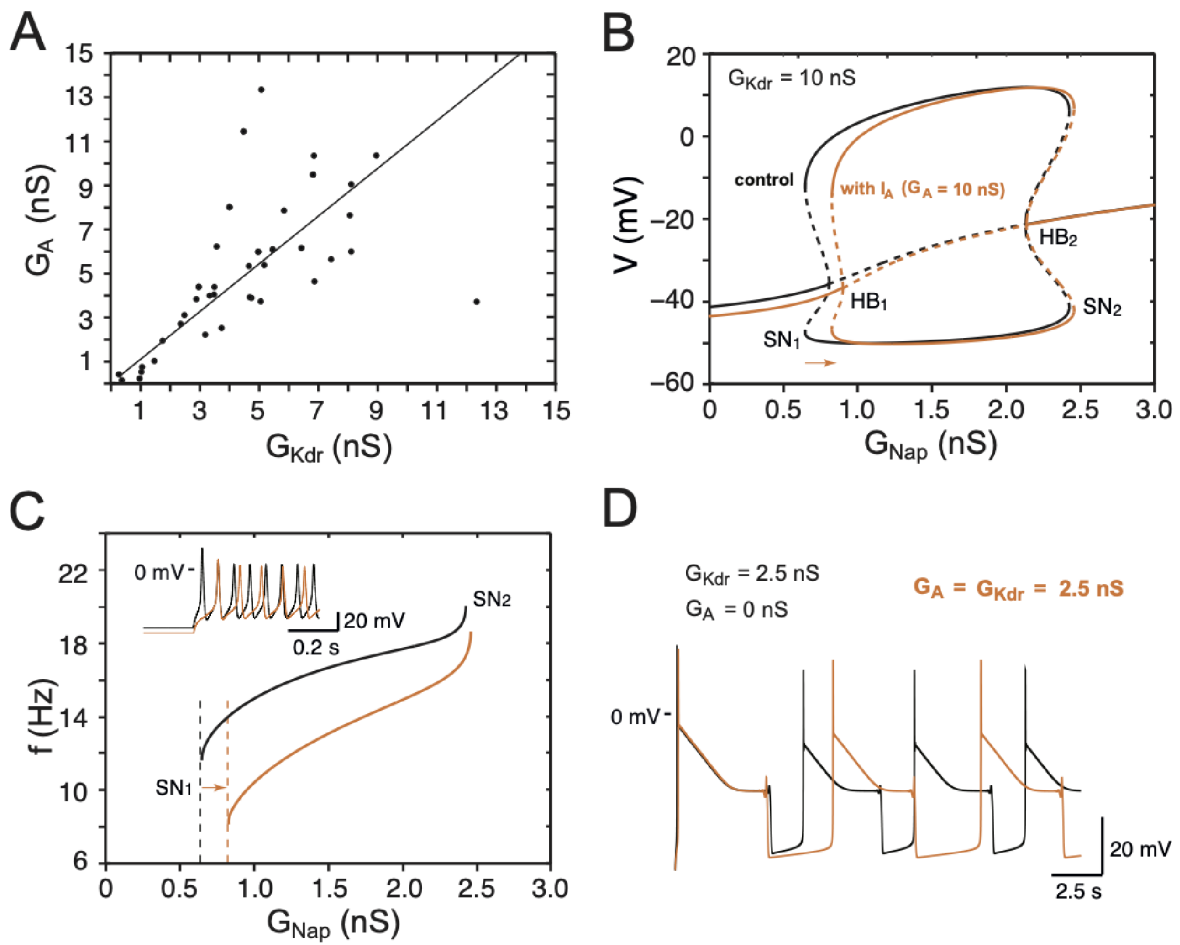


Fig 7 figure supplement 1

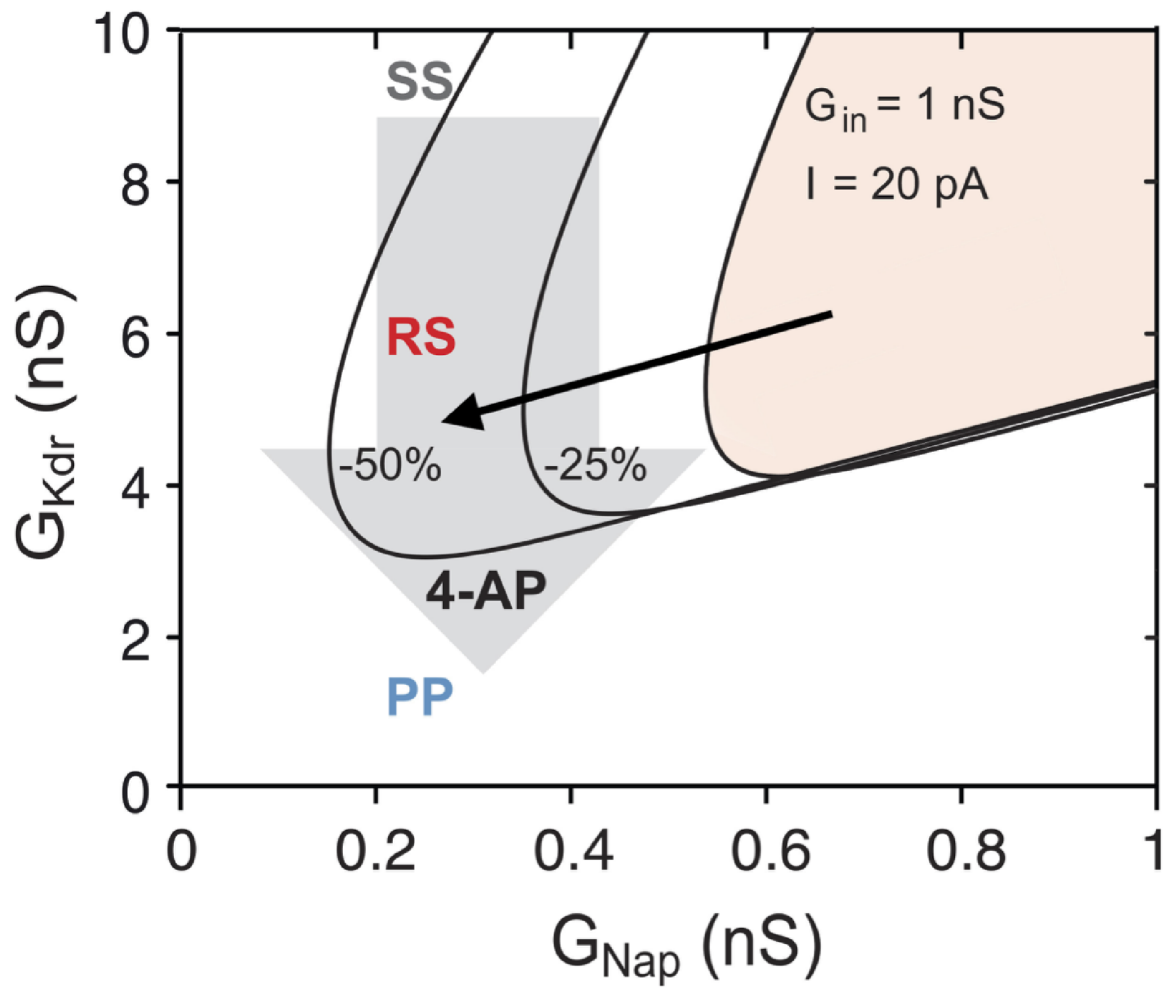


Fig 7 figure supplement 2